MICRO-EARTHQUAKE STUDIES USING CROSS
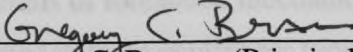CORRELATION-DERIVED HYPOCENTERS

A DISSERTATION
SUBMITTED TO THE DEPARTMENT OF GEOPHYSICS
AND THE COMMITTEE ON GRADUATE STUDIES
OF STANFORD UNIVERSITY
IN PARTIAL FULFILLMENT OF THE REQUIREMENTS
FOR THE DEGREE OF
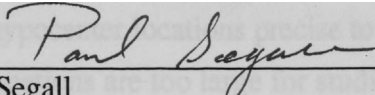DOCTOR OF PHILOSOPHY

Doug A. Dodge

November 1996

I certify that I have read this dissertation and that in my opinion it is fully adequate, in scope and quality, as a dissertation for the degree of Doctor of Philosophy.

Gregory C. Beroza (Principal Advisor)

I certify that I have read this dissertation and that in my opinion it is fully adequate, in scope and quality, as a dissertation for the degree of Doctor of Philosophy.

Paul Segall
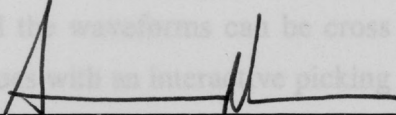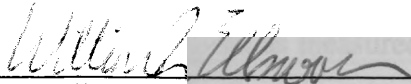
I certify that I have read this dissertation and that in my opinion it is fully adequate, in scope and quality, as a dissertation for the degree of Doctor of Philosophy.
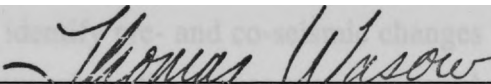
Amos Nur

I certify that I have read this dissertation and that in my opinion it is fully adequate, in scope and quality, as a dissertation for the degree of Doctor of Philosophy.

William Ellsworth

Approved for the University Committee on Graduate Studies:

Abstract

In this thesis I use seismograms recorded by regional short-period seismic networks in California and in Nevada to study details of foreshock mechanics and of coda wave scattering. The clusters of seismicity examined in these studies are typically less than 2 km in their greatest extent. A primary goal in analyzing the foreshock sequences is to see whether static stress changes from the foreshocks helped trigger the mainshocks, and to see if fault zone geometry might have been important in controlling mainshock initiation. These goals require relative hypocenter uncertainties that are a small fraction of the sequence dimensions. The coda waves I analyze have wavelengths as small as 1 km. To avoid errors in slowness estimation requires relative hypocenter locations precise to at least 250 m. Typical uncertainties in relative hypocenter locations are too large for studies such as these. However, the length scale of these problems is especially conducive to obtaining high-precision locations. Since the clusters of seismicity are small, the effectiveness of relative location techniques is maximized, and the seismograms are similar enough that waveform cross correlation is possible. It is not possible to completely automate the cross correlation repicking process, because not all the waveforms can be cross correlated. However, I have integrated automated techniques with an interactive picking program to process the entire sequences in a relatively efficient manner.

I find that the foreshocks do not usually appear to trigger the mainshock by static stress transfer. The foreshocks usually concentrate near structural discontinuities in the fault and are sufficiently distant from the mainshock fault plane that their static stress changes tend to destress the mainshock hypocenter. Fault zone heterogeneity may also be important in controlling the number of foreshocks, i.e., the stronger the heterogeneity, the greater the number of foreshocks. The size of the nucleation region, as measured by the extent of the foreshock sequence, also seems to scale with mainshock moment in the same manner as determined independently by measurements of the seismic nucleation phase.

Although coda waves are often considered to be generated by backscattering of primary waves from randomly distributed heterogeneities in the crust, theoretical and experimental work indicates that at least part of the coda may be due to near-receiver scattering. Since coda waves have been used to identify pre- and co-seismic changes in attenuation and velocity, it is important to know where the waves were scattered to properly interpret such results. I analyzed coda waves recorded at up to 78 central

California Calnet stations using 2 source arrays and found that at most stations, arrivals through the first 26 s of the coda were strongly clustered in azimuth and takeoff angle at or near the direct arrivals. This suggests that at nearly all of the stations analyzed, the coda consists primarily of waves scattered near the stations.

I use these results in combination with static stress modeling to study coseismic velocity decreases from the 1989 Loma Prieta earthquake observed by *Ellsworth et al.* [*1992*]. From the array analysis I conclude that the coda was produced by near-station scattering, and I hypothesize that the shear wave modulus changed near the station. One possible mechanism is a decrease in the mean stress due to the mainshock. I model the velocity change expected from this mechanism using the slip model of *Beroza* [*1991*] and a relation between pressure and shear wave velocity from *Jones* [*1983*] and find that this mechanism would produce a velocity increase in the region where velocity was observed to decrease. I conclude that the velocity decrease was more likely caused by crack opening due to strong shaking from the mainshock.

Preface

The four chapters of this dissertation are independent papers united by the common theme of using high-precision, cross correlation-derived hypocenters to study details of the earthquake process and of coda wave scattering in the Earth's crust. The first chapter is effectively an introduction in which I discuss factors that influence the precision of relative earthquake hypocenter locations, relative hypocenter relocation by cross correlation, and application of cross correlation to sequences larger than 1 km. In chapters 2 and 3 I use cross correlation-derived hypocenter locations to study six foreshock sequences and to make inferences about the earthquake initiation process based on the mechanics of those sequences. In the last chapter I form two source arrays of precisely relocated aftershocks and use them to study the directions of coda wave scattering in the source region.

Chapter 1, augmented with details about the programs I have developed for waveform cross correlation and repicking, will be submitted to *Computers in Geosciences*.

Chapter 2 was published in the June, 1995 issue of *Journal of Geophysical Research*. It is a detailed study of the foreshock sequence to the 1992 Landers, California earthquake. The paper considers the influence of fault zone geometry and static stress changes from the foreshocks in causing the mainshock. G. C. Beroza and W. L. Ellsworth were co-authors of this paper.

Chapter 3 will be published in the October, 1996 issue of *Journal of Geophysical Research*. It is an attempt to see whether the results of the Landers foreshock study generalize to other California foreshock sequences. An additional five foreshock sequences are analyzed and the static stress change calculations are augmented to produce stress change distributions that incorporate the uncertainties in the hypocentral parameter estimates. G. C. Beroza and W. L. Ellsworth are co-authors of this paper.

Chapter 4 will also be submitted to *Journal of Geophysical Research*. In this chapter I apply the source array technique of *Spudich and Bostwick* [1987] at up to 78 stations of the USGS CALNET array to study the behavior of coda waves at lapse times of up to 6S. G. C. Beroza is a co-author of this paper.

Acknowledgments

Table of Contents

List of Tables

List of Illustrations

Chapter 1 — Extending cross correlation-derived locations to larger groups of earthquakes

Abstract

Earthquakes with similar source parameters have similar seismograms, and that similarity may be exploited to obtain precise relative hypocenter locations. By cross correlating seismograms, the internal self-consistency of travel time picks can be improved, outliers can be eliminated, and additional observations can be added. Also, earthquakes that are spatially close enough to have similar seismograms share nearly common ray paths to the stations at which they are observed, so that nearly all unmodeled velocity structure can be accounted for using simple station corrections as part of a relative event location. Automated relocation procedures based on waveform cross correlation have been applied with considerable success in regions where tightly clustered events are common *e.g.* creeping faults and volcanic regions. However, there are significant research problems involving clustered seismicity that are not amenable to fully automated analysis. Research involving details of foreshock and aftershock behavior, fine-scale fault zone structure, and details of coda wave scattering require precise location of earthquakes only some of which may produce similar waveforms. In other cases, seismicity may be distributed as distinct clusters of earthquakes with inter-cluster distances too large to allow cross correlation. Nevertheless, cross correlation can be integrated into the relocation process for these earthquakes. I have developed a program that automatically identifies groups of similar seismograms and repicks them using an algorithm of *VanDecar and Crosson* [*1990*] while at the same time allowing interactive picking of seismograms that are too dissimilar to cross correlate. Inconsistencies between the group picks and manual picks are resolved so that the final locations are not biased. The program has been successfully used to study foreshock sequences and to construct two earthquake arrays used for a study of coda wave composition.

1.1 Introduction

The earthquake location problem is one of the oldest and most well-studied problems in seismology. Nevertheless, it is an incompletely solved problem in the sense that every hypocenter location is uncertain, possibly by a substantial amount. This uncertainty is due to imprecision in models of the earth's velocity structure and to the difficulty in obtaining data adequate to properly constrain the hypocenter solutions. As a consequence, the size of the uncertainty is also related to the scale length of the location problem (Figure 1). On the global scale, uncertainties may be 10's of kilometers [*Tucker et al., 1968*]. At the other extreme, small-aperture arrays for monitoring mining-induced seismicity have been used to obtain source locations with absolute errors of less than 10m [*Swanson et al., 1992*] and with uncertainties of less than 20m for events within the arrays [*Dodge and Sprenke, 1992*]. Between these extremes are the regional seismic networks.
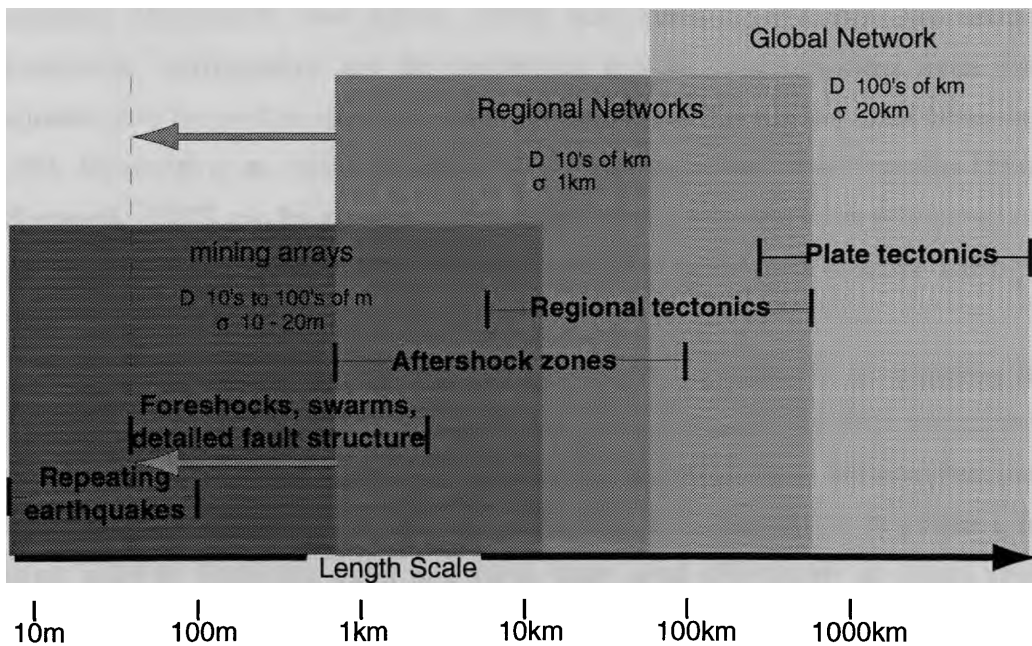
Figure 1.1. Schematic drawing showing the length scales of seismic networks and the corresponding geological problems for which they are optimized. The geological problems for which each network is optimized are determined by the network extent and the location precision obtainable with that geometry.

These networks are commonly used to obtain hypocenter locations with uncertainties of one km or less, and a principal goal of this thesis is to extend (where possible) the precision of network locations to well under 100 m. This can allow the use of regional

network data in the detailed study of fault zone structure and the mechanics of earthquake sequences.

Regional short-period seismic networks in California have been operational for over 20 years. In that time they have recorded tens-of-thousands of earthquakes and have played an important role in the study of regional tectonics and seismic hazard. The instruments are mostly vertical component velocity seismometers operated at high gain and the average station spacing along active faults is typically about 20 km. In many regions, the catalog of recorded events may be substantially complete to magnitude 1.0 [*Oppenheimer et al., 1992*]. Although the limited bandwidth and dynamic range of the telemetry and recording systems limits the usefulness of the seismograms for many types of analysis, the high density of recorded events is ideal for studying fine-scale features of faults as revealed by micro earthquakes. Examples include foreshock sequences, aftershock sequences, and the structure of fault jogs. Detailed examination of repeating earthquakes [*Ellsworth and Dietz, 1990*] may yield insight into the nature of "characteristic" earthquakes and the nucleation process. Seismograms from similar earthquakes may be used to search for time-dependent changes in the crust [*Poupinet et al., 1984; Ellsworth et al., 1992; Beroza et al., 1992*], and arrays of earthquakes [*Spudich and Bostwick, 1987*] can be constructed to study details of coda wave scattering in the source region. All of these studies depend critically on precise relative earthquake locations.

Fortunately, the length scale of these problems is conducive to obtaining high-precision locations. The clusters of seismicity are small, so relative location techniques are effective. Also, the seismograms are very similar and waveform cross correlation is possible. Automated procedures that use waveform cross correlation to produce high-precision relative locations exist and have been used effectively in some regions [*Deichmann and Garcia-Fernandez, 1992; Gillard et al., 1995*]. However, they are less useful when the seismicity under investigation consists of isolated clusters that must be relocated with respect to each other. In this chapter I discuss cross correlation-based techniques for relocating similar earthquakes, sources of error in relative earthquake locations, and the role that cross correlation can play in minimizing those errors. Then I discuss extension of cross correlation to larger sequences and my technique for processing sequences of discontinuous clusters. I illustrate the capabilities of that technique with results from the relocation of a group of earthquakes on the San Andreas fault.

1.2 Measuring relative arrival time by cross correlation

For years seismologists have been using waveform cross correlation as a means of obtaining high-precision relative earthquake hypocenter locations [*Nakamura, 1978; Pechmann and Kanamori, 1982; Poupinet et al., 1984; Frémont and Malone, 1987; Deichmann and Garcia-Fernandez, 1992; Dodge et al., 1995; Gillard et al., 1995*]. The existence of earthquakes with similar seismograms was noted by *Geller and Mueller* [*1980*]. They studied seismograms from four small earthquakes on the San Andreas fault, and noted that when low-pass filtered with a cutoff frequency of 2 Hz, the seismograms were nearly identical well into the coda. At these low frequencies the seismograms could
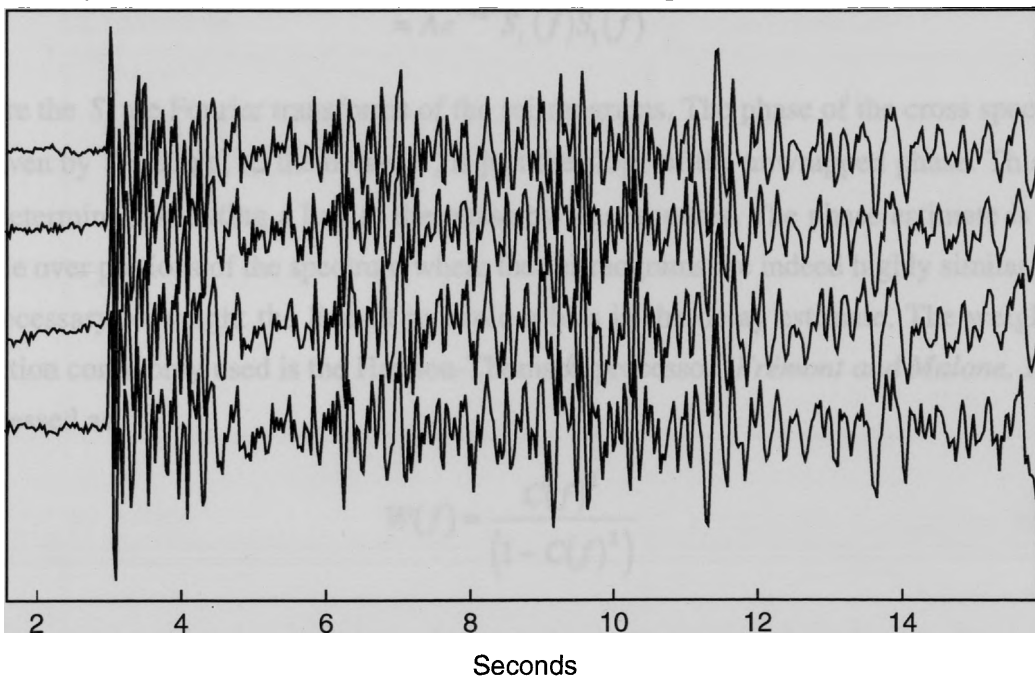
Figure 1.2. A multiplet consisting of four seismograms recorded by the USGS Calnet short period network. Only about 13 seconds of data are shown to make it easier to compare features, but these seismograms retain their similarity essentially all through the *S* wave coda.

be treated as Green's functions since the corner frequencies were above 10 Hz. The similarity of the Green's functions implied that the focal mechanisms were nearly identical and that the sources were located within 1/4 wavelength of each other (for the highest frequency at which the seismograms were similar). Subsequent studies (referenced above)

have shown that the similarity in waveforms can in some cases extend to frequencies of 15 Hz or more. An example of four such similar seismograms is shown in Figure 1.2.

Because of their similarity, these seismograms can be cross correlated to obtain precise differential arrival times. This may be done either in the time or frequency domains. In the frequency domain approach [*Poupinet et al., 1984*] the two seismograms $s_1(t)$ and $s_2(t)$ are treated as scaled and shifted copies of each other within the analysis window so that $s_2(t) = As_1(t - \tau)$ where A is the scale factor and τ is the frequency-independent delay. The cross spectrum is

$$S_{12}(f) = S_1^*(f)S_2(f)$$

$$= Ae^{2\pi i f \tau}S_1^*(f)S_1(f) \tag{1.1}$$

where the S_i are Fourier transforms of the seismograms. The phase of the cross spectrum is given by $\phi = 2\pi f\tau$, so the delay, τ, is just the slope of the unwrapped phase. This can be determined by fitting a line to the phase by least squares. The phase estimate is only stable over portions of the spectrum where the seismograms are indeed highly similar, so it is necessary to weight the line fit to avoid a bias in the delay estimate. The weighting function commonly used is the Hannon-Thomson processor [*Frémont and Malone, 1987*] expressed as

$$W(f) = \frac{C(f)^2}{\left(1 - C(f)^2\right)} \tag{1.2}$$

where $C(f)$ is the coherency

$$C(f) = \frac{\overline{S_{12}^2(f)}}{\overline{S_{11}(f)S_{22}(f)}} . \tag{1.3}$$

In Equation 1.3 the S_{ii} are auto spectra and the bars denote smoothing. This procedure is illustrated in Figure 1.2 (a - c) where (a) shows the two signals to be analyzed, (b) shows their coherency for frequencies up to 15 Hz, and (c) shows the phase of their cross spectrum. Because of the coherency weighting, the line fit is not affected by the large
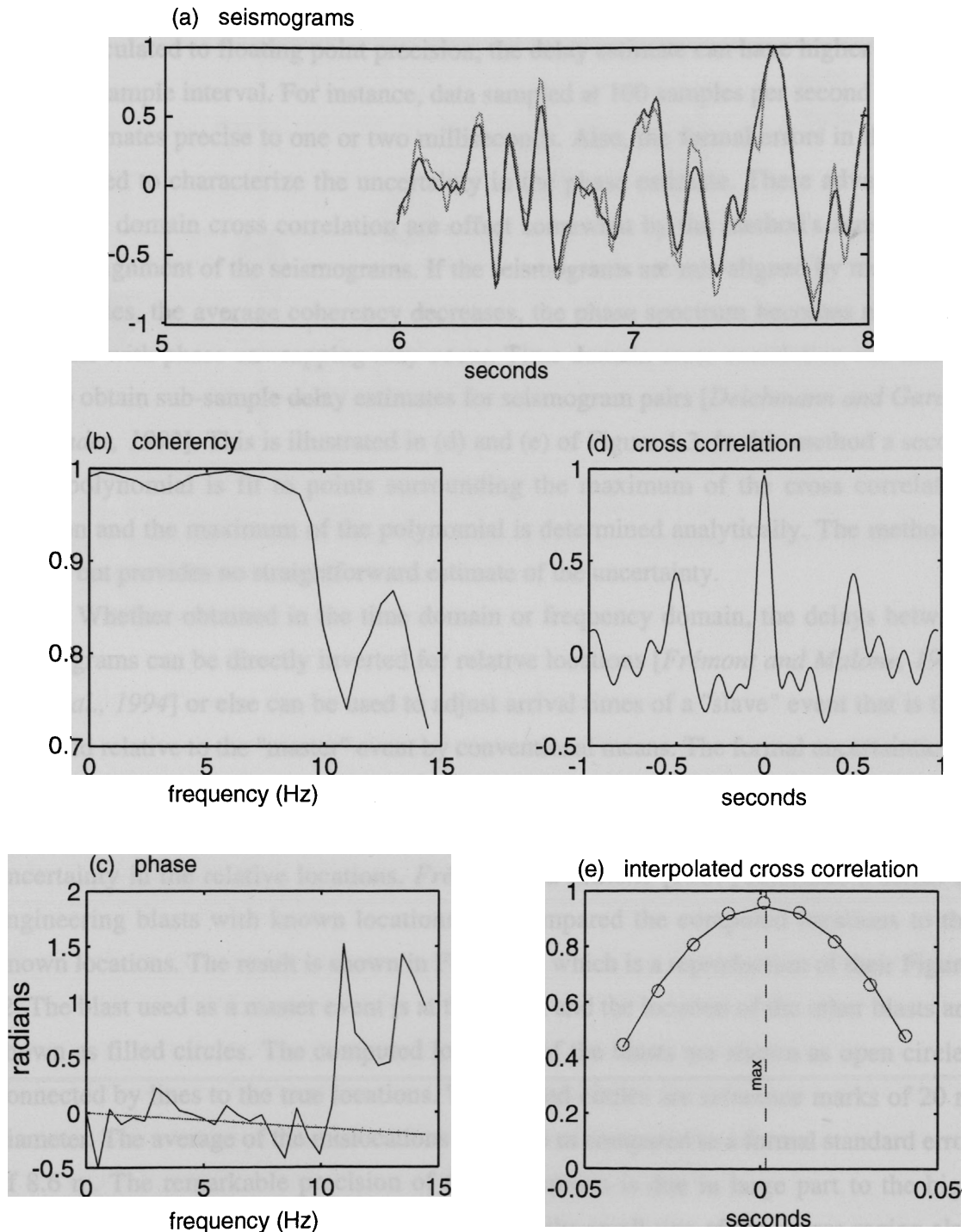
Figure 1.3. Illustration of frequency domain and time domain delay estimation. (a) 2 s of the seismograms for which the delay is to be determined. (b) Coherency spectrum. (c) Phase spectrum. (d) The cross correlation function for lags from -1 s to +1 s. (e) Close-up of the cross correlation function for lags near zero showing the quadratic fit and the maximum of the quadratic.

excursions in the phase curve for frequencies greater than 10 Hz. Since the slope of the line is calculated to floating point precision, the delay estimate can have higher precision than one sample interval. For instance, data sampled at 100 samples per second can yield delay estimates precise to one or two milliseconds. Also, the formal errors in the line fit can be used to characterize the uncertainty in the phase estimate. These advantages of frequency domain cross correlation are offset somewhat by the method's sensitivity to starting alignment of the seismograms. If the seismograms are mis-aligned by more than a few samples, the average coherency decreases, the phase spectrum becomes noisy, and problems with phase unwrapping may occur. Time domain cross correlation can also be used to obtain sub-sample delay estimates for seismogram pairs [*Deichmann and Garcia-Fernandez, 1992*]. This is illustrated in (d) and (e) of Figure 1.3. In this method a second order polynomial is fit to points surrounding the maximum of the cross correlation function and the maximum of the polynomial is determined analytically. The method is robust, but provides no straightforward estimate of the uncertainty.

Whether obtained in the time domain or frequency domain, the delays between seismograms can be directly inverted for relative locations [*Frémont and Malone, 1987; Got et al., 1994*] or else can be used to adjust arrival times of a "slave" event that is then relocated relative to the "master" event by conventional means. The formal uncertainties in these relative locations may be remarkably small, often less than 10 m. Despite their small size, these formal uncertainties probably are an accurate characterization of the true uncertainty in the relative locations. *Frémont and Malone* [*1987*] relocated a series of engineering blasts with known locations and compared the computed locations to the known locations. The result is shown in Figure 1.3 which is a reproduction of their Figure 2. The blast used as a master event is at the origin and the location of the other blasts are shown as filled circles. The computed locations of the blasts are shown as open circles connected by lines to the true locations. The shaded circles are reference marks of 20 m diameter. The average of the mislocations was 11.6 m compared to a formal standard error of 8.6 m. The remarkable precision of these locations is due in large part to the high precision of the cross correlation picks. However, the small size of the source region also played a major role in these results. Had the source region had been much larger, the waveforms would have been too dissimilar to cross correlate. Moreover, even if the traces could have been repicked with the same precision, the master event relocation process would not have worked as well since the ray paths of the master event would not have
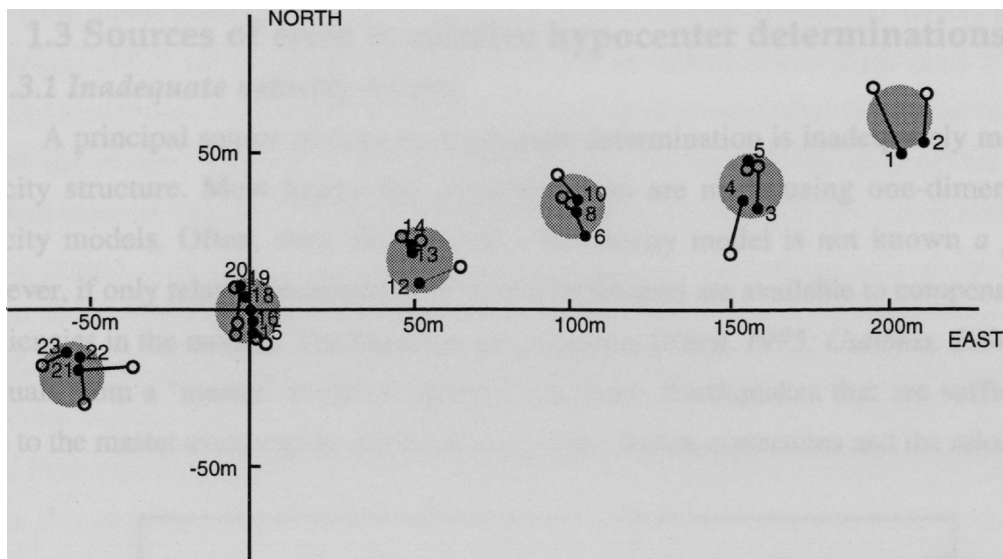
Figure 1.4. Reproduction of Figure 2 from *Frémont and Malone* [*1987*]. Filled circles are true locations of engineering blasts. Open circles are computed locations of blasts. Gray shaded circles are for reference and are 20 m in diameter.

been similar to those of the other events. Some of the research problems explored in this thesis have a scale length of a kilometer or more. Before attempting to apply cross correlation techniques to these larger regions it is useful to understand the importance of different error sources in the relocation process to see to what extent improved arrival time picks can will improve location estimates over bigger length scales. Because of the fundamental importance of the hypocenter in many seismological investigations, much effort has been expended in examining error sources in hypocenter estimation *e.g.* [*Flinn, 1965; Evernden, 1969; Lee and Lahr, 1975; Buland, 1976*]. A common consensus is that pick errors, velocity model errors, and numerical instability arising from the geometry of the problem account for the errors in computed hypocenters. I take that as a given, and in the next section explore their relative importance in order to characterize the maximum size of the source region for which cross correlation picking is likely to be useful.

1.3 Sources of error in relative hypocenter determinations

1.3.1 Inadequate velocity models

A principal source of error in hypocenter determination is inadequately modeled velocity structure. Most hypocenter determinations are made using one-dimensional velocity models. Often, even the optimal 1-D velocity model is not known *a priori*. However, if only relative locations are required, techniques are available to compensate for deficiencies in the models. The master event technique [*Fitch, 1975; Gubbins, 1990*] uses residuals from a "master" event as station corrections. Earthquakes that are sufficiently close to the master event can be relocated using these station corrections and the relocations
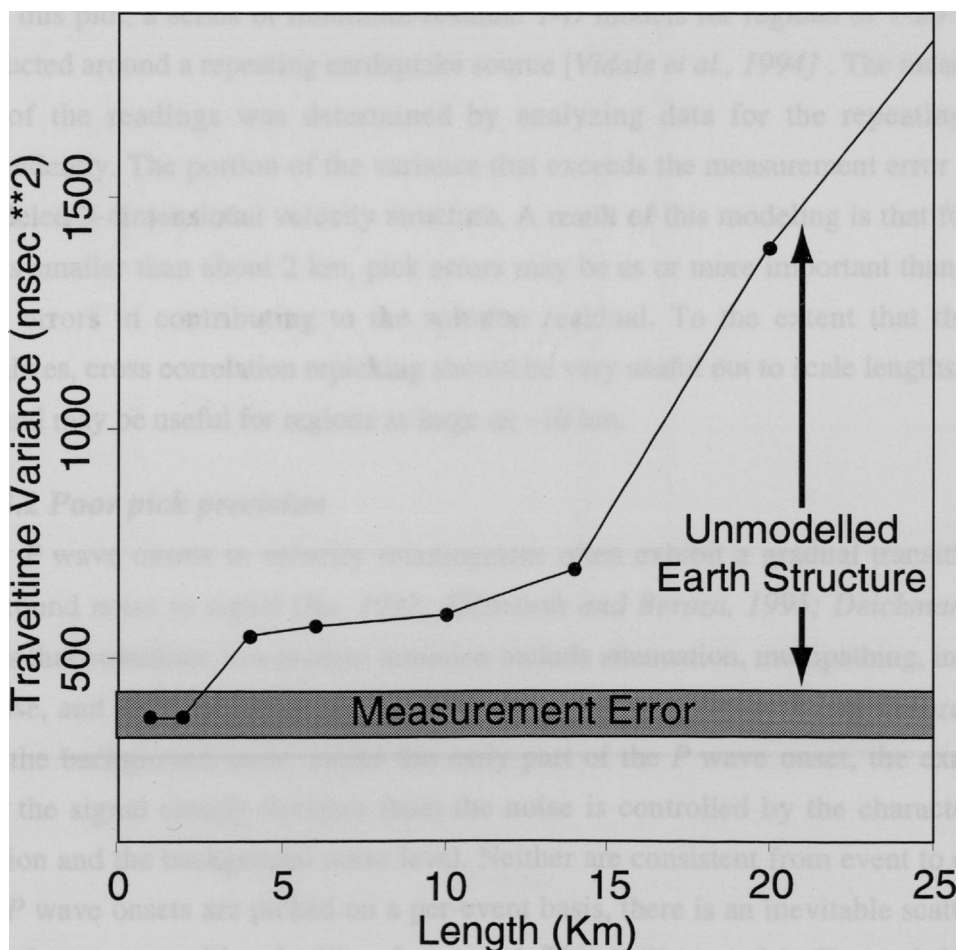
Figure 1.5. Reproduction of figure from [*Ellsworth,* 1994]. This is a plot of travel time variance as a function of problem scale length produced by relocating groups of earthquakes using a best 1-D model with station corrections and plotting the average travel time variances against the group dimension.

will have small solution residuals. The joint hypocenter determination (JHD) method [*Douglas, 1967*] solves simultaneously for a set of station corrections (and possibly velocity model corrections) that minimize in a least squares sense the travel time residuals for all the events. These methods decrease in effectiveness as the dimensions of the problem increase because the ray paths become more dissimilar with increasing size of the source region. The rate at which residuals increase with increasing size of the source region is dependent on the strength and distribution of velocity heterogeneities and therefore varies from place to place. However, some insight may be gained by studying a particular region. Figure 1.5 is a reproduction from *Ellsworth et al.* [*1994*] and shows travel time variance as a function of scale length for the earthquake location problem. To obtain this plot, a series of minimum-residual 1-D models for regions of 1-20 km were constructed around a repeating earthquake source [*Vidale et al., 1994*] . The measurement error of the readings was determined by analyzing data for the repeating source independently. The portion of the variance that exceeds the measurement error is due to unmodeled 3-dimensional velocity structure. A result of this modeling is that for source regions smaller than about 2 km, pick errors may be as or more important than velocity model errors in contributing to the solution residual. To the extent that this result generalizes, cross correlation repicking should be very useful out to scale lengths of about 2 km and may be useful for regions as large as ~10 km.

1.3.2 Poor pick precision

P wave onsets in velocity seismograms often exhibit a gradual transition from background noise to signal [*Iio, 1992; Ellsworth and Beroza, 1995; Deichman, 1996*]. Factors that contribute to a gradual initiation include attenuation, multipathing, instrument response, and may also result from a nucleation process [*Ellsworth and Beroza, 1995*]. Since the background noise masks the early part of the *P* wave onset, the exact place where the signal clearly deviates from the noise is controlled by the character of the transition and the background noise level. Neither are consistent from event to event, so when *P* wave onsets are picked on a per-event basis, there is an inevitable scatter in the picks of up to several hundredths of a second. This is illustrated in Figure 1.6. The top shows a group of similar seismograms aligned by cross correlation. The events range in magnitude from M=1.2 to M=2.1. The vertical bar shows the location of a common *P* wave pick. The lower part shows a number of the same seismograms with the same alignment, but with the traces offset from one another vertically so that individual signal
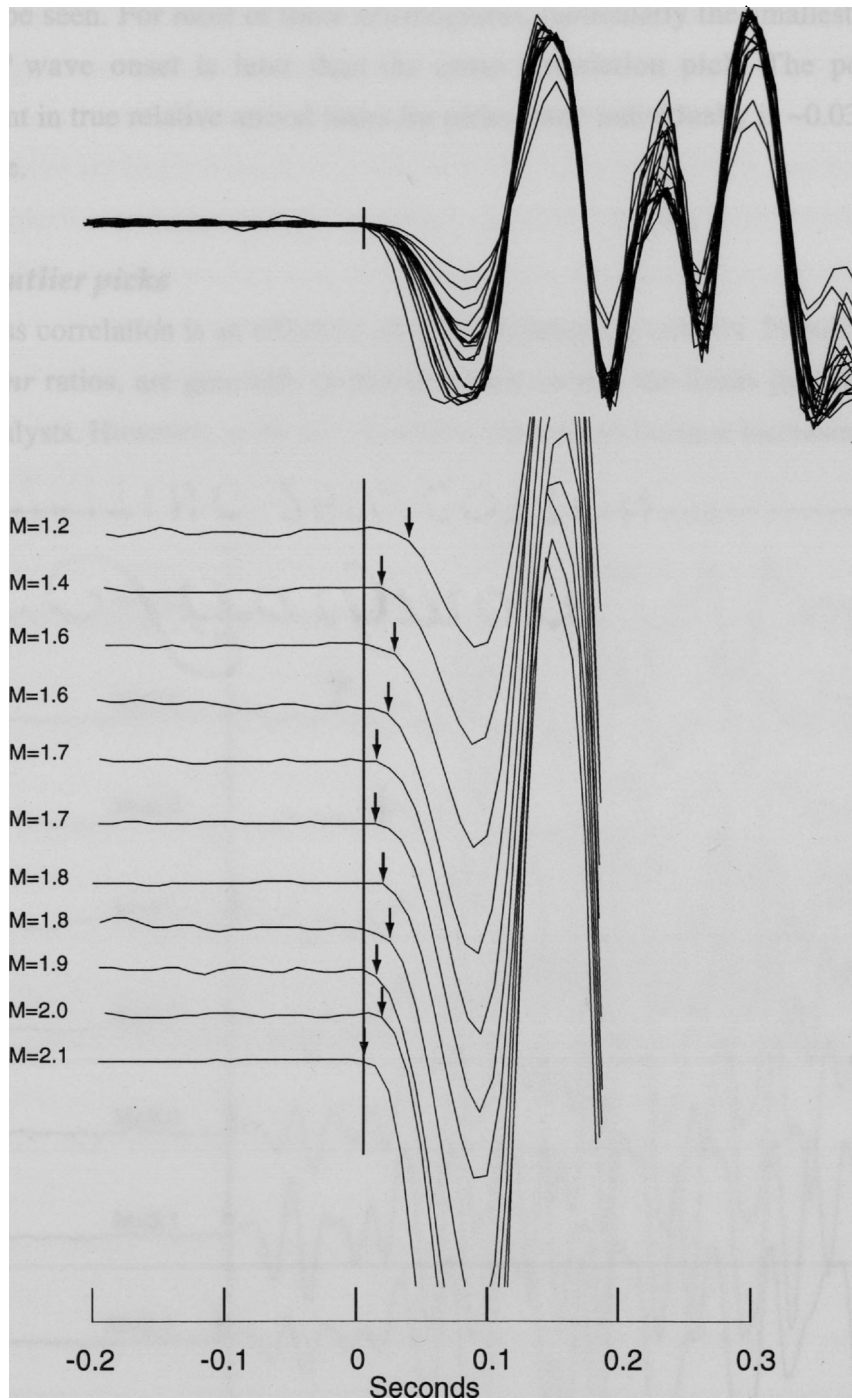
Figure 1.6. Illustration of pick errors induced by emergent onset of P waves. (top) Seismograms aligned by cross correlation. Vertical bar at t=0 is the pick for the largest event. (bottom) Same alignment of seismograms but with vertical separation so that individual onsets may be distinguished. Note that for many of the smaller events, the apparent onset when viewed in isolation is much later than the relative onset determined by cross correlation.

onsets can be seen. For most of these seismograms, particularly the smallest events, the apparent *P* wave onset is later than the cross correlation pick. The potential for disagreement in true relative arrival times for picks made individually is ~0.03 seconds in this example.

1.3.3 Outlier picks

Cross correlation is an effective means of eliminating outliers. Impulsive arrivals, with high *snr* ratios, are generally picked precisely (within the limits just discussed) by network analysts. However, as the *snr* decreases, the arrivals become increasingly
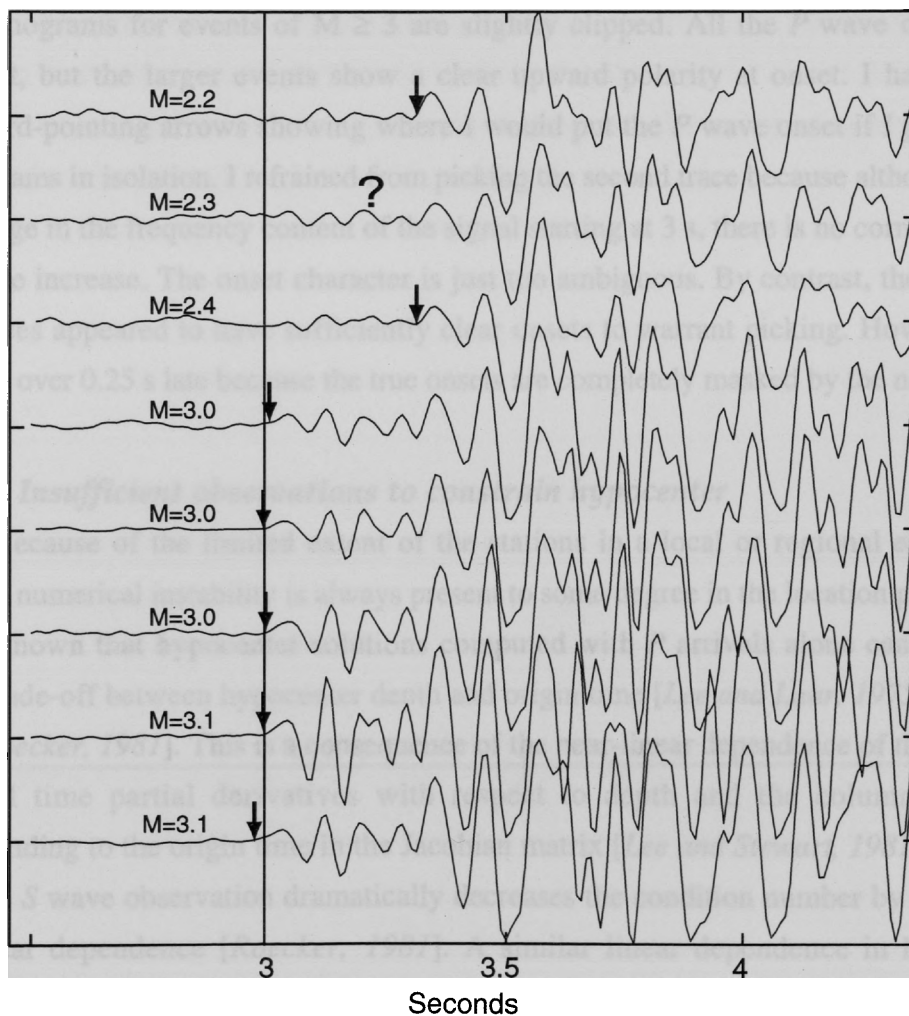
Figure 1.7. Avoiding outlier picks and gaining additional observations by cross correlation. Events shown range in magnitude from 2.2 to 3.1. Direct arrival is preceded (about 0.3 s) by a relatively weak arrival that is below the noise level for the smaller events.

indistinct, until at some point, the trace is not used. Within this region of decreasing usability, significant pick errors are possible when the traces are picked by hand. These outliers are relatively uncommon, but when they do occur they can seriously bias the solution. If there are many redundant observations the effect of outliers may be suppressed by robust solution techniques [*Meremonte et al., 1995; Maurer and Kradolfer, 1996; Shearer, 1996*] as long as they are not leverage points. But, if the solution is poorly constrained by the available observations then the only recourse is to identify and fix the errors since removing observations may only worsen the situation. For example, Figure 1.7 shows seismograms aligned by cross correlation. Magnitudes range from M = 2.2 to M = 3.1. Note that the seismograms are very similar, sharing all major features, although the seismograms for events of M $\geq$ 3 are slightly clipped. All the *P* wave onsets are emergent, but the larger events show a clear upward polarity at onset. I have added downward-pointing arrows showing where I would put the *P* wave onset if I picked the seismograms in isolation. I refrained from picking the second trace because although there is a change in the frequency content of the signal starting at 3 s, there is no corresponding amplitude increase. The onset character is just too ambiguous. By contrast, the first and third traces appeared to have sufficiently clear onsets to warrant picking. However, my picks are over 0.25 s late because the true onsets are completely masked by the noise.

1.3.4 Insufficient observations to constrain hypocenter

Because of the limited extent of the stations in a local or regional earthquake network, numerical instability is always present to some degree in the location problem. It is well known that hypocenter solutions computed with *P* arrivals alone can exhibit a strong trade-off between hypocenter depth and origin time [*Lee and Lahr, 1975; Buland, 1976; Roecker, 1981*]. This is a consequence of the near-linear dependence of the column of travel time partial derivatives with respect to depth and the column of ones corresponding to the origin time in the Jacobian matrix [*Lee and Stewart, 1981*]. Adding even one *S* wave observation dramatically decreases the condition number by removing that linear dependence [*Roecker, 1981*]. A similar linear dependence in horizontal coordinates can occur when events occur outside the network or at least have no observations over a large range of azimuths. In these cases very small errors in timing or velocity model parameterization can produce large biases in the computed hypocentral coordinates [*Lahr, 1992*].

Because of time constraints and the desire to avoid outlier picks, analysts are generally reluctant to pick traces with very weak onsets. So, for small (M < 2.0) events only a fraction of the usable traces may be picked. Often there are no S wave picks made at all because of the lack of horizontal component data. This can result in poorly constrained hypocenters for the reasons just discussed. However, if the traces can be cross correlated, many additional P wave picks can be obtained. Cross correlation can also be used quite effectively in picking relative S wave arrivals. If the seismograms are similar and the S wave amplitudes are significantly larger than the P wave coda, then cross correlating the traces in a window around the expected S wave arrival can produce sets of relative S wave picks that are as consistent as the cross correlation-derived P wave picks. Although the exact location of the true S wave arrival may not be well determined by this method, the ambiguity is common to all the traces, and can be absorbed in a station correction, provided the wavegroup identified with the S wave has the assumed slowness in the source region. An example is shown in Figure 1.8.
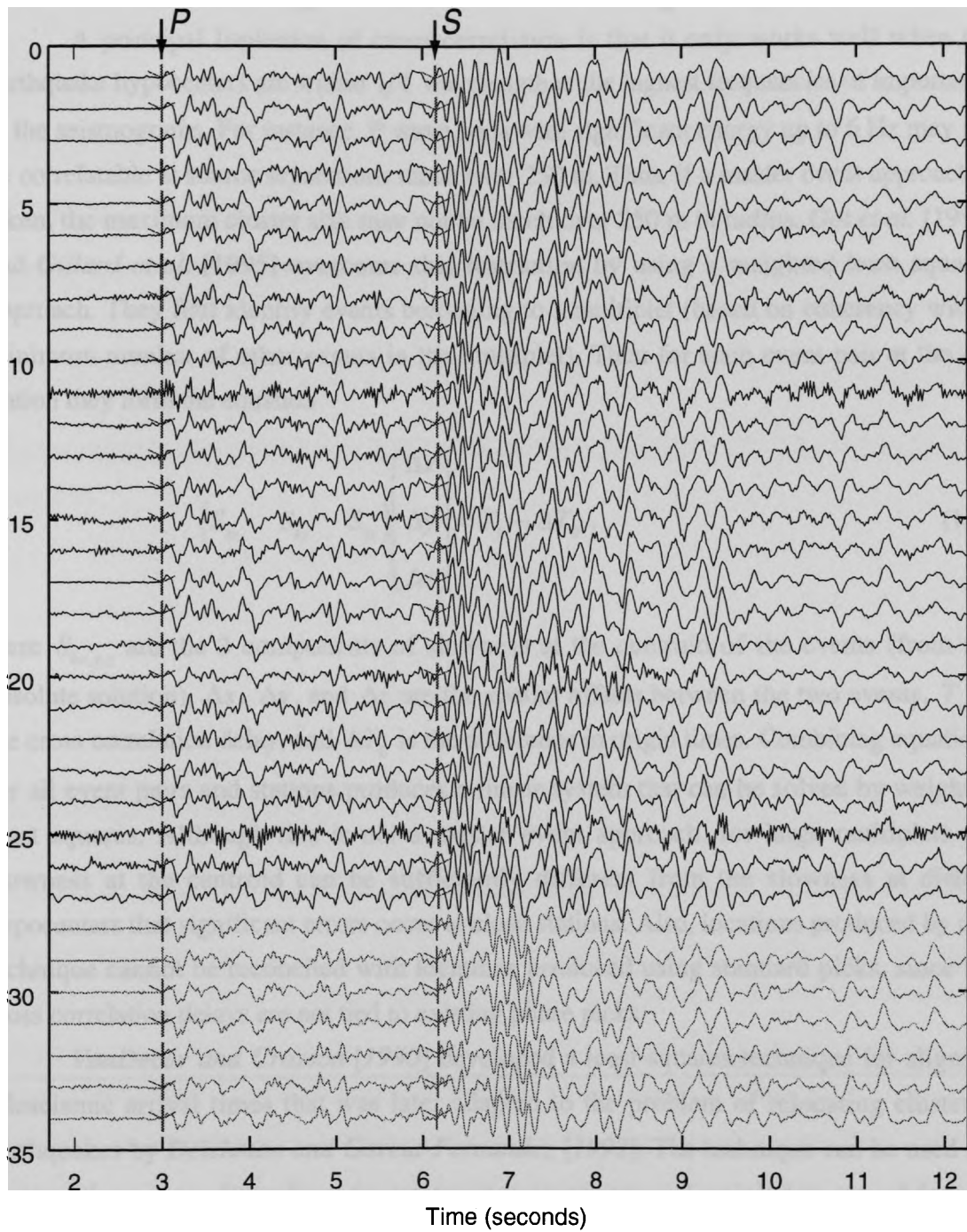
Figure 1.8. Example of *S* wave picks by cross correlation. In this example every trace with a *P* wave pick also has an *S* wave pick. The exact location of the *S* wave pick is not critical since a separate *S* wave station correction is calculated.

1.4 Extending cross correlation to larger sequences

A principal limitation of cross correlation is that it only works well when the earthquake hypocenters are within 1/4 wavelength at the highest frequencies of importance in the seismograms. For instance, *P* wave coda with significant energy up to 6 Hz may not be correlatable at source separations much over 250 m. Thus, if a master event approach is taken, the maximum cluster size may not be much over 250 m in radius. *Got et al.* [1994] and *Gillard et al.* [1995] overcome this restriction by using a weighted least squares approach. They first identify events belonging to a multiplet (based on coherency with a minimum number of other events in the multiplet). Then for each event pair at the *kth* station they form the equation

$$\begin{pmatrix} S_{kx} & S_{ky} & S_{kz} \end{pmatrix} \begin{pmatrix} \Delta x \\ \Delta y \\ \Delta z \end{pmatrix} = T_k - \Delta T_0 \ . \tag{1.4}$$

Here $S_{kx,y,z}$ are the 3 components of slowness at the centroid of the events (from the absolute solution), Δx, Δy, and Δz are the spatial offsets between the two events, T_k is the cross correlation delay, and ΔT_0 is the difference in origin times. Combining equations for all event pairs and stations produces a linear system that can be solved by weighted least squares. Although this is not a master event approach, for large multiplets the slowness at the centroid can be sufficiently different from the slowness at distant hypocenters that significant errors occur at close stations. Also, locations produced by this technique cannot be reconciled with locations produced using standard picks, since the cross correlation delays are not tied to existing phase picks.

VanDecar and Crosson [*1990*] developed a least-squares technique for aligning teleseismic arrival times that was later adapted to the problem of relocating clustered earthquakes by *Deichman and Garcia-Fernandez* [*1992*]. The technique can be used for clusters that are too large for a master event approach since the pick determined for any trace is influenced primarily by the cross correlation delays relative to similar traces. The approach is to calculate all possible cross correlation delays and use a weighted least-squares adjustment to solve for a set of arrival time corrections most consistent with the set of delays. The corrected arrival times may then be input to a hypocenter location program. For a set of *N* traces, one calculates all *N(N-1)/2* cross correlations. For the *i,j* pair of

traces the cross correlation delay is Δt_{ij} and the value of the cross correlation at that delay is C_{ij}. The set of arrival times that will make all the delays zero (for consistent data) must satisfy

$$t_i - t_j = \Delta t_{ij}.$$ (1.6)

An additional constraint must also be imposed to make the system non-singular (for solution by least squares), and a convenient constraint is

$$\sum_{i=1}^{N} t_i = 0.$$ (1.7)

The resulting linear system has a data kernel of dimension *N(N-1)/2+1* by *N*. For *N=3* the system is

$$\begin{pmatrix} 1 & -1 & 0 \\ 1 & 0 & -1 \\ 0 & 1 & -1 \\ 1 & 1 & 1 \end{pmatrix} \begin{pmatrix} t_1 \\ t_2 \\ t_3 \end{pmatrix} = \begin{pmatrix} \Delta t_{12} \\ \Delta t_{13} \\ \Delta t_{23} \\ 0 \end{pmatrix}.$$ (1.8)

The least-squares solution is of the form

$$\tilde{t} = \left[\underline{\underline{A}}^T \underline{\underline{W}} \underline{\underline{A}} \right]^{-1} \underline{\underline{A}}^T \underline{\underline{W}} \underline{d}_t.$$ (1.9)

Here the weighting matrix $\underline{\underline{W}}$ is derived from the cross correlation values C_{ij}. The simple form of the data kernel $\underline{\underline{A}}$ allows the expressions $\underline{\underline{A}}^T \underline{\underline{W}} \underline{\underline{A}}$ and $\underline{\underline{A}}^T \underline{\underline{W}} \underline{d}_t$ to be directly determined from the data, so the largest array required is only *N* by *N*. Because the least squares adjustment is only used to modify arrival times, complications arising from spatial variability of slowness do not occur. In principal, the weighted least squares adjustment procedure could be used with arbitrarily large clusters of earthquakes since the weighting matrix nearly zeros-out rows corresponding to delays between non-similar traces. In practice, for very dissimilar seismograms, the cross correlation is subject to cycle-skipping, and severe errors can be introduced at that stage. However, if seismograms are pre-grouped by similarity and groups are processed individually then problems with cross correlation are minimal and the method performs quite well.

My study of foreshock sequences has required precise relative hypocenter locations for sequences that extend to more than a kilometer in at least one dimension. Often the sequences have clusters of seismicity near the eventual mainshock hypocenter, and it is important to resolve the internal features of these clusters to model stress changes that might influence main shock nucleation. It is also important to resolve the larger scale structure of the sequences to understand how fault zone geometry might influence initiation. Relocation by JHD helps to identify major features of the sequences, but the location errors for solutions based on network P wave picks are too large to resolve small-scale features. Also, where network coverage is poor, relatively small pick errors can
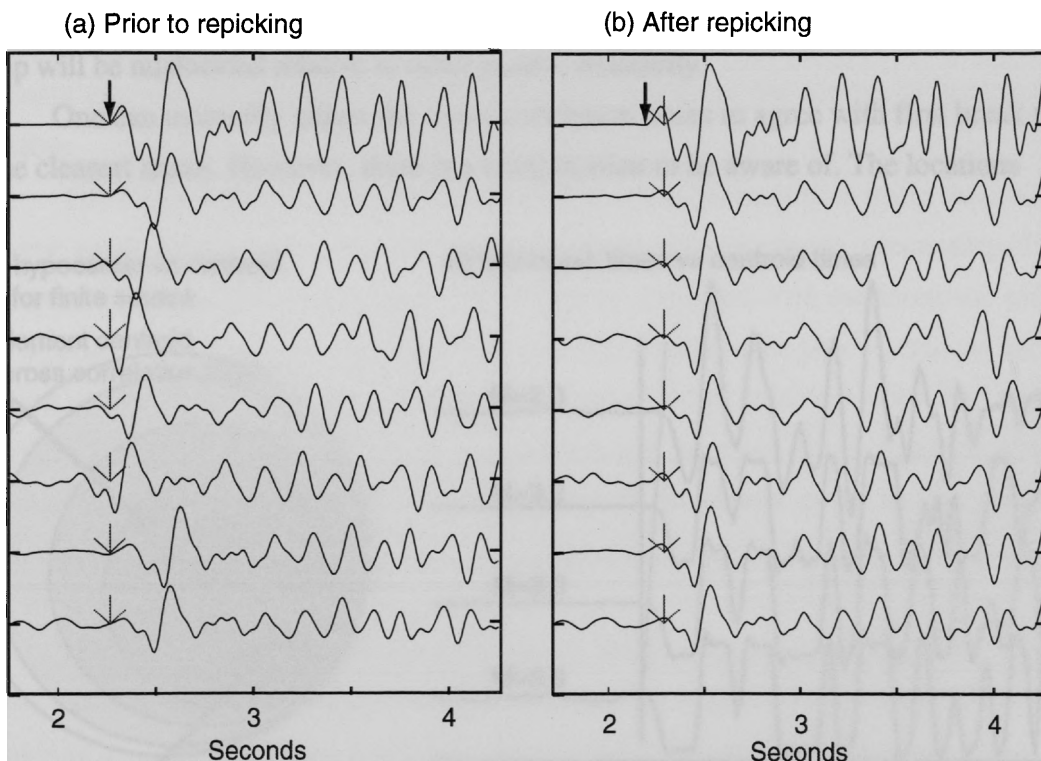
Figure 1.9. Example showing the possible bias in pick locations produced by the *VanDecar and Crosson* [*1990*] least squares algorithm. (a) Seismogram alignment prior to repicking. (b) Alignment after repicking.

translate into large location errors, particularly in depth. Applying the *VanDecar and Crosson* [*1990*] algorithm to seismograms from the clustered earthquakes is often quite effective in resolving those problems. However, there is no assurance that the least squares picks will be consistent between groups or will be consistent with hand picks

made on the ungrouped traces. The adjustment vector $\tilde{t}$ is zero mean, so unless the starting pick errors are distributed with a zero mean, the final picks will be biased. This is illustrated in Figure 1.9 which shows a set of seismograms prior to repicking by least squares (a) and after (b). In both (a) and (b) the location of the P wave picks is shown by the light down-pointing arrows. The top trace has an exceptionally clear onset marked with a heavy down-pointing arrow. Prior to repicking (a) it is clear from the waveform misalignment that some of the picks must be in error, but at least, the first trace is correctly picked. After repicking by least squares, the trace alignments are correct but it is obvious from inspection of the first trace that the picks are systematically late. This error will not affect the relative locations of the events within this group, but it guarantees that the entire group will be mislocated relative to other nearby seismicity.

One can manually adjust the cross correlation times to agree with first break times of the clearest traces. However, there is a complication to be aware of. The locations

a) hypocenter vs centroid
for finite source

b) first-break times vs centroid times
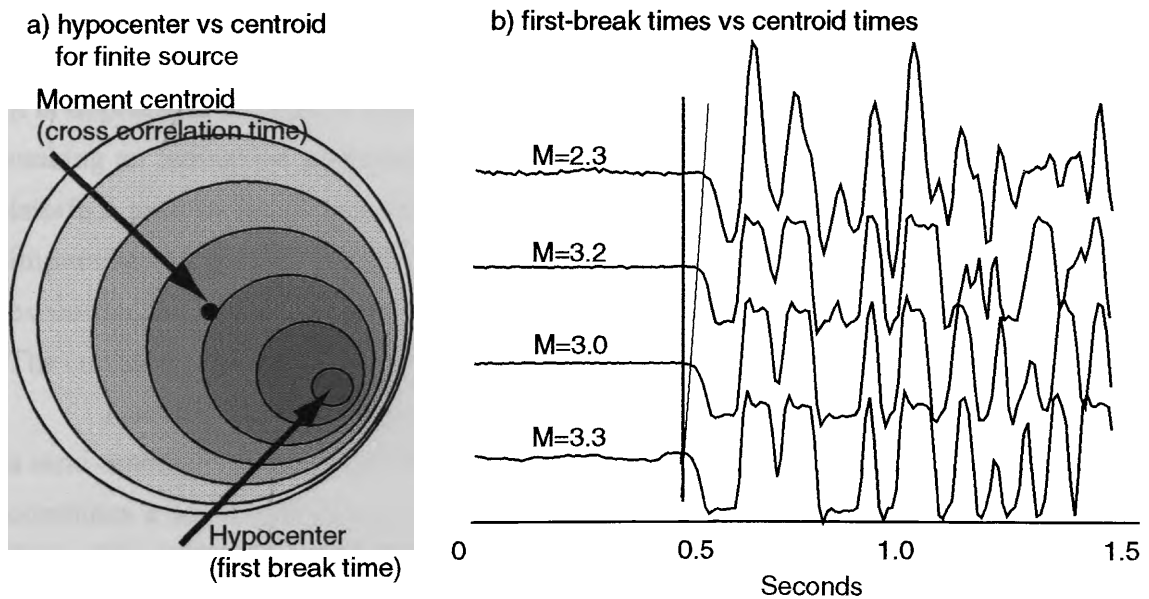
Figure 1.10. (a) Comparison of hypocenter location to moment centroid location and (b) comparison of relative centroid times as obtained by cross correlation to times from first breaks.

calculated using first breaks are hypocenter locations, but the locations calculated using cross correlation are relative centroid locations. For finite sources, these may not be the same (Figure 1.10 a), and without knowing the details of the rupture process for each

earthquake, it is impossible to reconcile them. For sufficiently small earthquakes, the errors introduced by combining the two types of picks may be comparable to or even less than errors from unmodeled earth structure. However, as shown in Figure 1.10 (b) for earthquakes as small as M 3+, the difference between first break times and centroid times can be several hundredths of a second.

Despite the limitations introduced by mixing first-break times with cross correlation alignments, this approach is still preferable to allowing groups of similar events to "float" relative to one another by unknown, random amounts. Most of the earthquakes I have processed have magnitudes less than M 2.5. The source dimensions of these earthquakes are probably so small that the differences between the first-break times for events with the same centroid times are less than 0.02s. Also, within the groups, times are all determined by cross correlation, so the relative locations of events in the groups is as precise as possible.

The major difficulty with interactive, first-break picks is that while their use can prevent gross errors in the relative group locations, the automatic processing flow is interrupted. If the interactive picking is not efficiently integrated with the automatic picking, it is impractical to process anything other than the smallest data sets. A critical factor in making an interactive program efficient is the nature of its interface with the user. The interface must be intuitive and simple, to minimize user time and effort. Also, because it is impossible to predict what the user may want to do at any point in the program's execution, the underlying program must be event-driven rather than procedural in nature. The current technology that meets these goals is the graphical user interface (GUI).

I created a GUI program using the MATLAB programming language that provides a semi-automatic means of producing sets of consistent *P* and *S* wave picks. The program combines a set of interactive tools for viewing seismograms and adjusting picks, with tools for automatic sorting, grouping, and repicking by least squares. At its core is an implementation of the *VanDecar and Crosson* [*1990*] least-squares algorithm and an adaptation of the nearest-neighbor clustering algorithm [*Jain and Dubes, 1988*].

The similarity measure used for grouping is peak cross correlation value of a windowed seismogram relative to a stack of seismograms already included in the group. If the cross correlation peak exceeds the threshold value, the seismogram is added to the group and the group stack is updated. No similarity matrix is constructed, so very large numbers of seismograms can be grouped this way. The speed of the algorithm varies

inversely with the percentage of similar seismograms in the candidate group. In the worst case when no groups are found, $N(N-1)/2$ cross correlations must be computed. In the best case, when all seismograms belong to one group, N-1 cross correlations must be computed.

By merging the manual processing required for seismograms that cannot be cross correlated with automatic grouping and cross correlation-repicking, this program provides a relatively efficient way to process waveform data. While clearly not as efficient as fully automatic cross correlation pickers, the program has a greater domain of applicability. It has been used to obtain high-precision locations for several foreshock sequences and for two source arrays. It has also been used to study details of aftershock sequences of the Landers and Loma Prieta earthquakes. In each of these instances, only a portion of the seismograms could be repicked automatically, and that portion by itself could not provide the necessary information to meet the study requirements. Only by merging the manual and automatic picks, as my program does, was it possible to complete these studies.

1.5 Example Relocations

Figures 1.10-1.11 show the results of several attempts to relocate clusters of earthquakes, each attempt a refinement of the previous solution. These figures illustrate both the level at which the cross correlation picks become important in refining the solution, and the effectiveness of the adjustment procedure just described in producing consistent picks for earthquakes in discontinuous clusters. Shown are 172 earthquakes that occurred from 1984 to 1996 on the San Andreas fault north of San Juan Bautista at depths of 8 to 12 km. The earthquakes (Figure 1.10) were recorded by the USGS Calnet array and the stations used are shown as filled triangles As the final locations reveal, the seismicity is strongly clustered. The dimensions of individual clusters are generally less than 100 m and within clusters the waveforms are highly correlated. However, the inter-cluster distances are much larger (in some cases over 1 km) so the seismograms are poorly correlated between clusters. It is not possible to build a multiplet that spans all the events (at any reasonably high coherency value) so the *Got et al.* [*1994*] method is not useful here. The *VanDecar and Crosson* [*1990*] technique applied to the entire group of earthquakes would probably have been more effective, but could not have repicked all the seismograms accurately since some do not correlate well with any others.
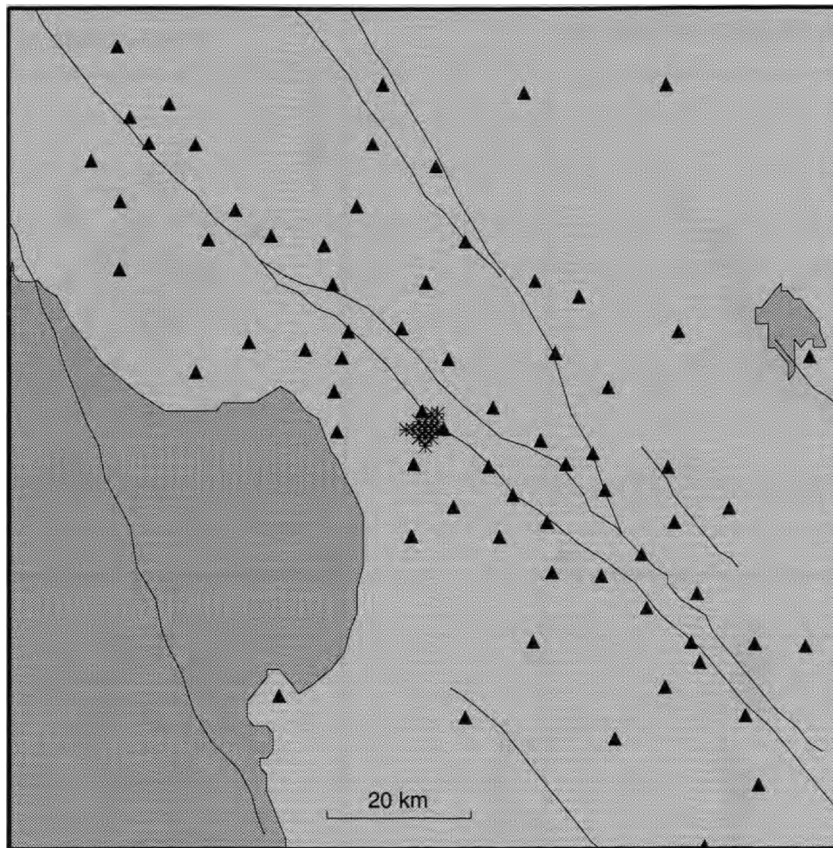
Figure 1.10. Basemap for the location problem. The cluster of earthquakes to be relocated is on the San Andreas fault north of San Juan Bautista in central California. The network locations for these events are shown as asterisks near the center of the map. Stations of the USGS Calnet network used in the relocation are shown as filled triangles.

Figure 1.11 shows (a) the earthquakes located using a 1-D velocity model with no station terms using the network picks and (b) relocated by JHD. The top panels are map views and the bottom panels are the cross sections indicated on the map views. In both cases, 4529 observations were used. The hypocenters are shown as open circles for the original locations (a), and as crosses the size of which indicate the 2σ uncertainty in the relative locations (b). In (a) essentially no structure can be distinguished. The uncertainties are much larger than the average inter-event spacing (700 m horizontal and 1500 m vertical), so the spatial pattern that emerges is attributable to errors in the hypocenter estimates. The average residual is 0.3 s. The JHD locations (b) clearly define a fault plane,
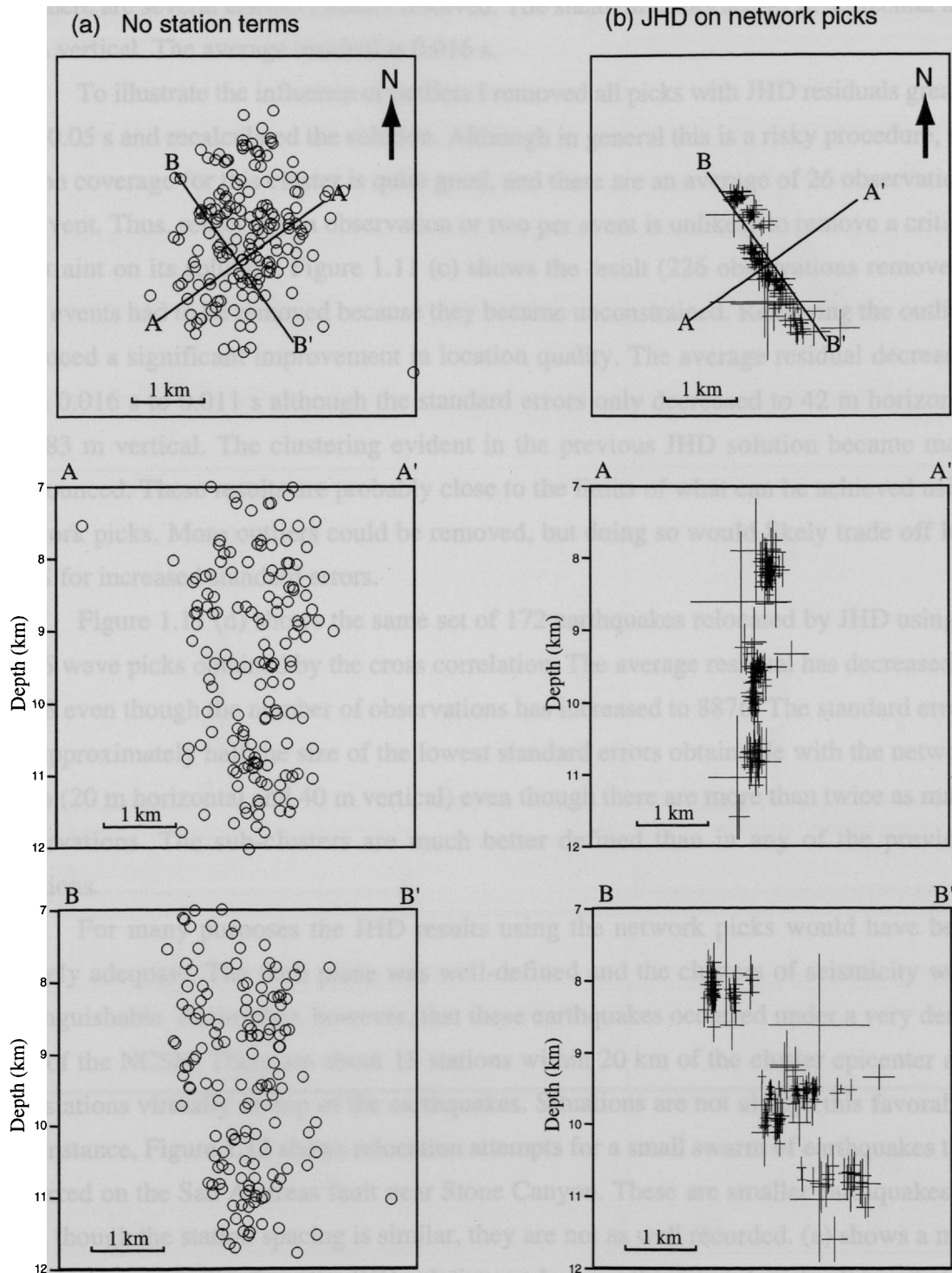
Figure 1.11. (a) Locations produced using final velocity model with no station terms and using network picks. (top) Map view of the seismicity. (center and bottom) Cross sections indicated on the map view. The standard errors are so large relative to the cluster dimensions that they are not shown. (b) The same earthquakes relocated by JHD using the network picks.

and there are several distinct clusters resolved. The standard errors are 45 m horizontal and 95 m vertical. The average residual is 0.016 s.

To illustrate the influence of outliers I removed all picks with JHD residuals greater than 0.05 s and recalculated the solution. Although in general this is a risky procedure, the station coverage for this cluster is quite good, and there are an average of 26 observations per event. Thus, removing an observation or two per event is unlikely to remove a critical constraint on its solution. Figure 1.11 (c) shows the result (226 observations removed). Two events had to be removed because they became unconstrained. Removing the outliers produced a significant improvement in location quality. The average residual decreased from 0.016 s to 0.011 s although the standard errors only decreased to 42 m horizontal and 83 m vertical. The clustering evident in the previous JHD solution became more pronounced. These results are probably close to the limits of what can be achieved using network picks. More outliers could be removed, but doing so would likely trade off low RMS for increased standard errors.

Figure 1.11 (d) shows the same set of 172 earthquakes relocated by JHD using *P* and *S* wave picks obtained by the cross correlation. The average residual has decreased to 0.008 even though the number of observations has increased to 8876. The standard errors are approximately half the size of the lowest standard errors obtainable with the network picks (20 m horizontal and 40 m vertical) even though there are more than twice as many observations. The sub-clusters are much better defined than in any of the previous locations.

For many purposes the JHD results using the network picks would have been entirely adequate. The fault plane was well-defined and the clusters of seismicity were distinguishable. Remember, however, that these earthquakes occurred under a very dense part of the NCSN. There are about 18 stations within 20 km of the cluster epicenter and two stations virtually on top of the earthquakes. Situations are not always this favorable. For instance, Figure 1.12 shows relocation attempts for a small swarm of earthquakes that occurred on the San Andreas fault near Stone Canyon. These are smaller earthquakes so even though the station spacing is similar, they are not as well recorded. (a) shows a map view and cross section from the JHD solution made using the network picks. It is not at all clear from these locations that these earthquakes occurred on a NW striking fault. By contrast, the JHD solution made using the cross correlation picks (b) leaves no doubt.
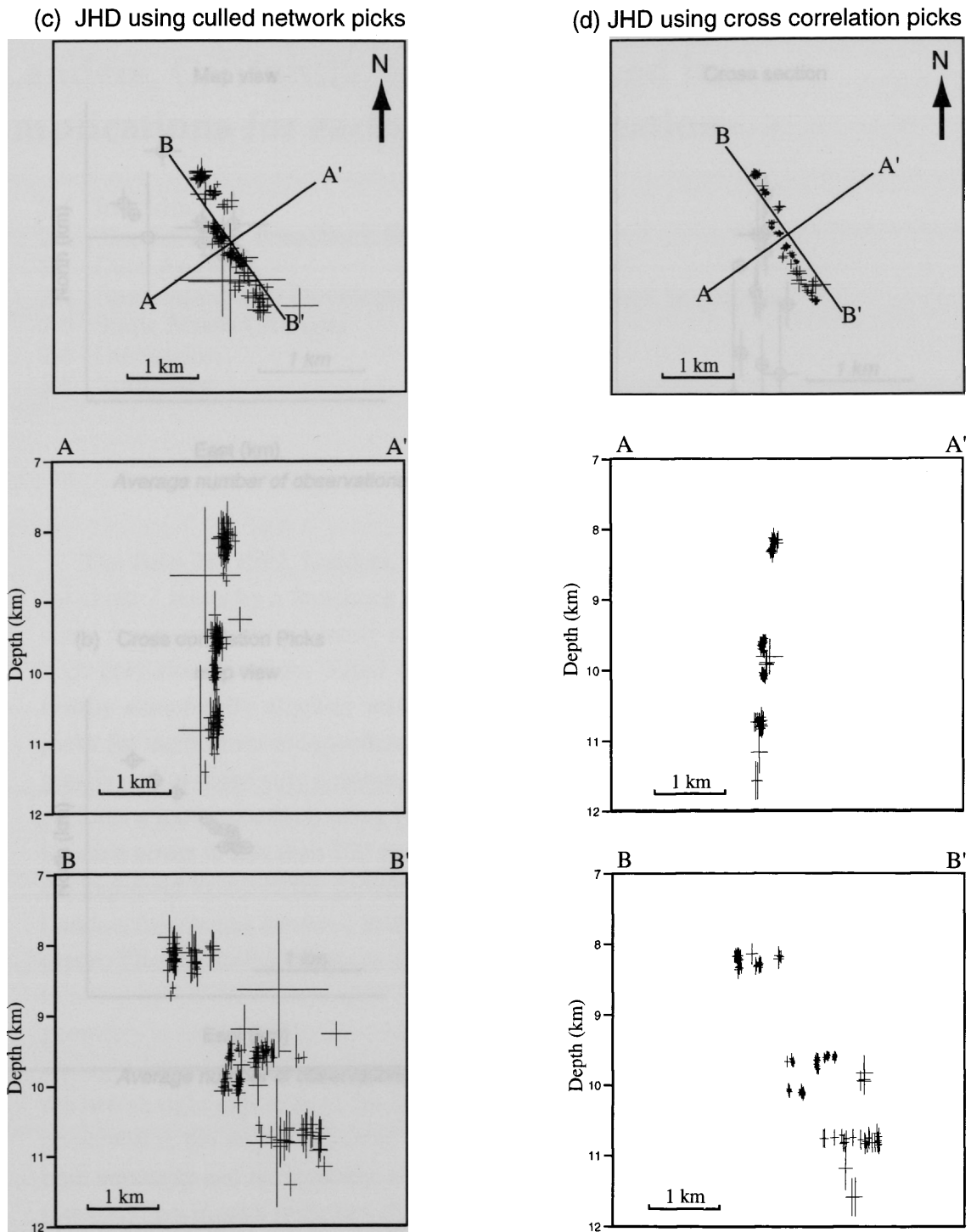
Figure 1.11. (c) JHD Locations after removing observations with residuals greater than 0.05 seconds in the previous solution. (d) Same events relocated by JHD with cross correlation picks.

(a) Network Picks
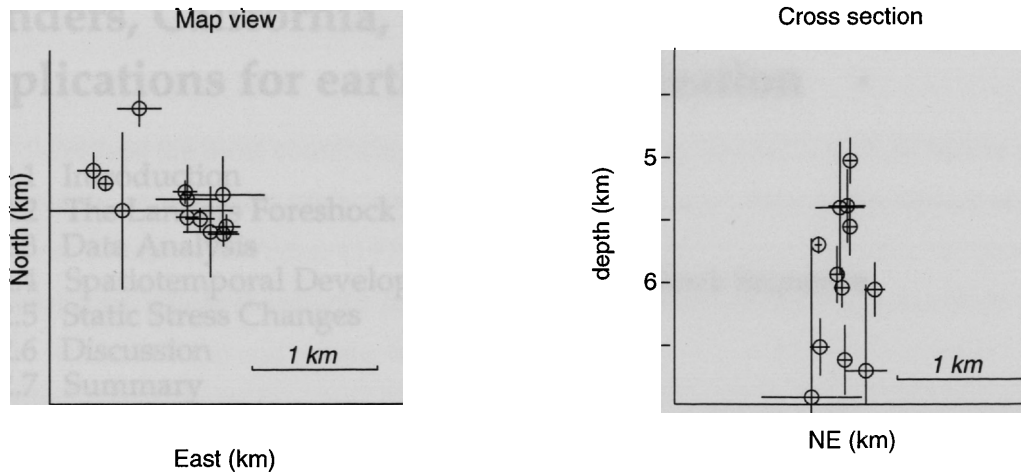
Average number of observations = 16 Average RMS = 0.024 Number of S-picks = 6
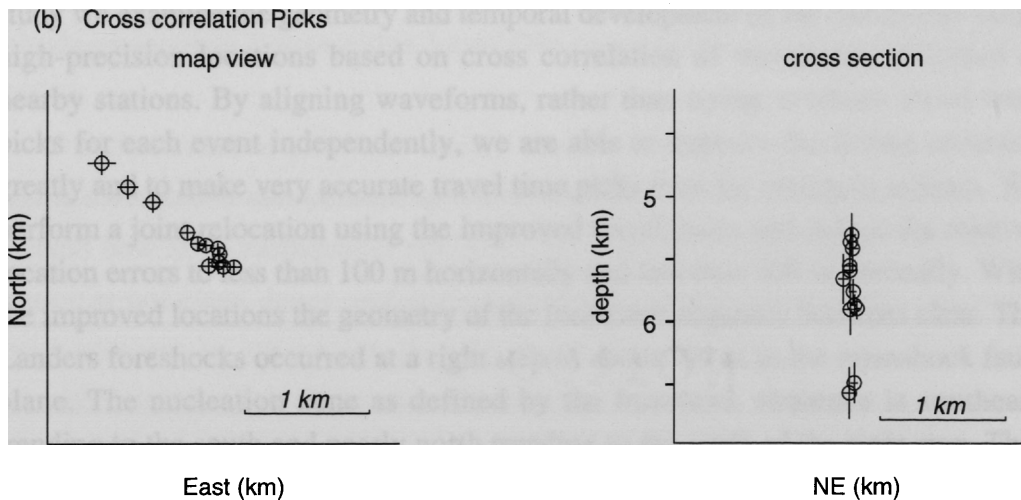
Average number of observations= 30 Average RMS = 0.014 Number of S-picks = 45

Figure 1.12. (a) Map and cross section views of a small cluster of earthquakes relocated by JHD using network picks. b) Same earthquakes relocated by JHD using cross correlation picks. Number of observations has nearly doubled while average RMS has been nearly halved. The fault plane is clearly defined in the second set of locations.

Chapter 2 — Foreshock sequence of the 1992 Landers, California, earthquake and its implications for earthquake nucleation

Abstract

The June 28, 1992, Landers, California, earthquake (M_W=7.3) was preceded for about 7 hours by a foreshock sequence consisting of at least 28 events. In this study we examine the geometry and temporal development of the foreshocks using high-precision locations based on cross correlation of waveforms recorded at nearby stations. By aligning waveforms, rather than trying to obtain travel time picks for each event independently, we are able to improve the timing accuracy greatly and to make very accurate travel time picks even for emergent arrivals. We perform a joint relocation using the improved travel times and reduce the relative location errors to less than 100 m horizontally and less than 200 m vertically. With the improved locations the geometry of the foreshock sequence becomes clear. The Landers foreshocks occurred at a right step of about 500 m in the mainshock fault plane. The nucleation zone as defined by the foreshock sequence is southeast trending to the south and nearly north trending to the north of the right step. This geometry is confirmed by the focal mechanisms of the foreshock sequence, which are right-lateral and follow the trend as determined by the foreshock locations on the two straight segments of the fault, and are rotated clockwise for foreshocks that occur within the step. The extent of the foreshock sequence is approximately 1 km both vertically and horizontally. Modeling of the Coulomb stress changes due to all previous foreshocks indicates that the foreshocks probably did not trigger each other. This result is particularly clear for the M_W=4.4 immediate foreshock. Since stress transfer in the sequence appears not to have played a significant role in its development, we infer an underlying aseismic nucleation process, probably aseismic creep. Other studies have shown that earthquake nucleation may be controlled by fault zone irregularities. This appears to be true in the case of the

Landers earthquake, although the size of the irregularity is so small that it is not detectable by standard location techniques.

2.1 Introduction

Perhaps the most convincing evidence that there is a nucleation stage before major earthquakes comes from observations of foreshocks. In a study of foreshock activity worldwide, *Jones and Molnar* [1979] found that 44% of ($M > 7$) earthquakes are preceded by foreshocks, where foreshocks are classified as any event greater than magnitude 4 that occurs within 100 km and within 40 days of the mainshock. *Ishida and Kanamori* [1978] classified as foreshocks five very similar events that occurred in the vicinity of the eventual hypocenter and within the 2 years before the 1971 San Fernando earthquake. These are examples of what *Mogi* [1985] refers to as "foreshocks in the broad sense." Foreshocks in the strict sense occur within a few hours to days of the mainshock, and within a few source dimensions of the mainshock. For instance, the M_L=7.3 Haicheng earthquake was preceded by about 500 earthquakes within 4 days of the mainshock. Of these, all with magnitude greater than 2 were within 5 km of the eventual mainshock epicenter [*Zongjin et al.,* 1990].

Foreshocks are of particular interest because of their potential use in forecasting damaging earthquakes and because an understanding of foreshock behavior may help us understand how large earthquakes nucleate. The exact role of foreshocks in earthquake nucleation is not clear. *Jones and Molnar* [1979] attributed foreshocks to accelerating premonitory creep on the mainshock fault plane. This assumption was used by *Ohnaka* [1993] who linked the size of the nucleation zone to the region of foreshock activity. *Jones* [1984] found that the length of foreshock sequences is inversely proportional to depth, and concluded that this relation was due to increasing normal stress with depth. Since increased normal stress lengthens the time from creep onset to failure in theoretical nucleation models [*Dieterich*, 1978], a creep mechanism of foreshock generation was judged to be unlikely. Instead, *Jones* [1984] proposed a model of delayed multiple rupture with the time delay between ruptures, being the time required for static fatigue to bring adjacent patches to the failure point; however, *Ohnaka* [1992] maintains that earthquakes can nucleate without foreshocks near the base of the seismogenic crust, if the slip-weakening displacement is great enough.

In this paper we study the foreshock sequence of the 1992 M_W=7.3 Landers earthquake. The Landers foreshocks are interesting because they are well recorded and unambiguously associated with a major strike-slip earthquake. By detailed examination of this sequence, we are able to study some aspects of the nucleation process. Our basic data are seismograms recorded by the Southern California Seismic Network (SCSN). These are vertical component velocity seismograms recorded on 1 Hz sensors telemetered to the Southern California Earthquake Center, where they are digitized at 100 samples per second, analyzed, and eventually archived.

We relocate the foreshocks by the method of joint hypocenter determination (JHD) using relative arrival times determined by waveform cross correlation. With this method we obtain relative location uncertainties for most of the foreshocks that are less than 100 m in horizontal coordinates and less than 200 m in depth. We determine focal mechanisms for 14 of the largest foreshocks and the first of the two immediate foreshocks identified by *Abercrombie and Mori* [1994] to help confirm the geometry of the sequence and for use in modeling the static stress changes generated by the foreshock sequence. We estimate stress drops of several of the foreshocks using an empirical Green's function technique, and use these to constrain the static stress change modeling. We then estimate the static stress changes resolved on the foreshock fault planes due to the preceding foreshocks. Finally, we use the information obtained from our analysis to evaluate models of earthquake nucleation.

2.2 The Landers Foreshock Sequence

The M_W 7.3 Landers, California, earthquake was the largest earthquake in a sequence that began April 23 with the M_W=6.1 Joshua Tree earthquake. The Landers earthquake occurred on June 28, 1992, at 1157 UT, approximately 2 months after the Joshua Tree earthquake. The mainshock initiated with a M_W=4.4 immediate foreshock [*Abercrombie and Mori*, 1994] before propagating ~70 km along strike to the northwest [*Cohee and Beroza*, 1994]. The epicenter was about 30 km north-northwest of the Joshua Tree epicenter, and the Joshua Tree aftershock zone extended to within a few kilometers of the Landers epicenter (Figure 2.1). There was an unmistakable foreshock sequence for the Landers earthquake. It consisted of 27 events that occurred within 7 hours of the Landers mainshock and that were tightly clustered within about 1.5 km of the mainshock hypocenter [*Hauksson et al.*, 1994]. There were an additional eight events that occurred
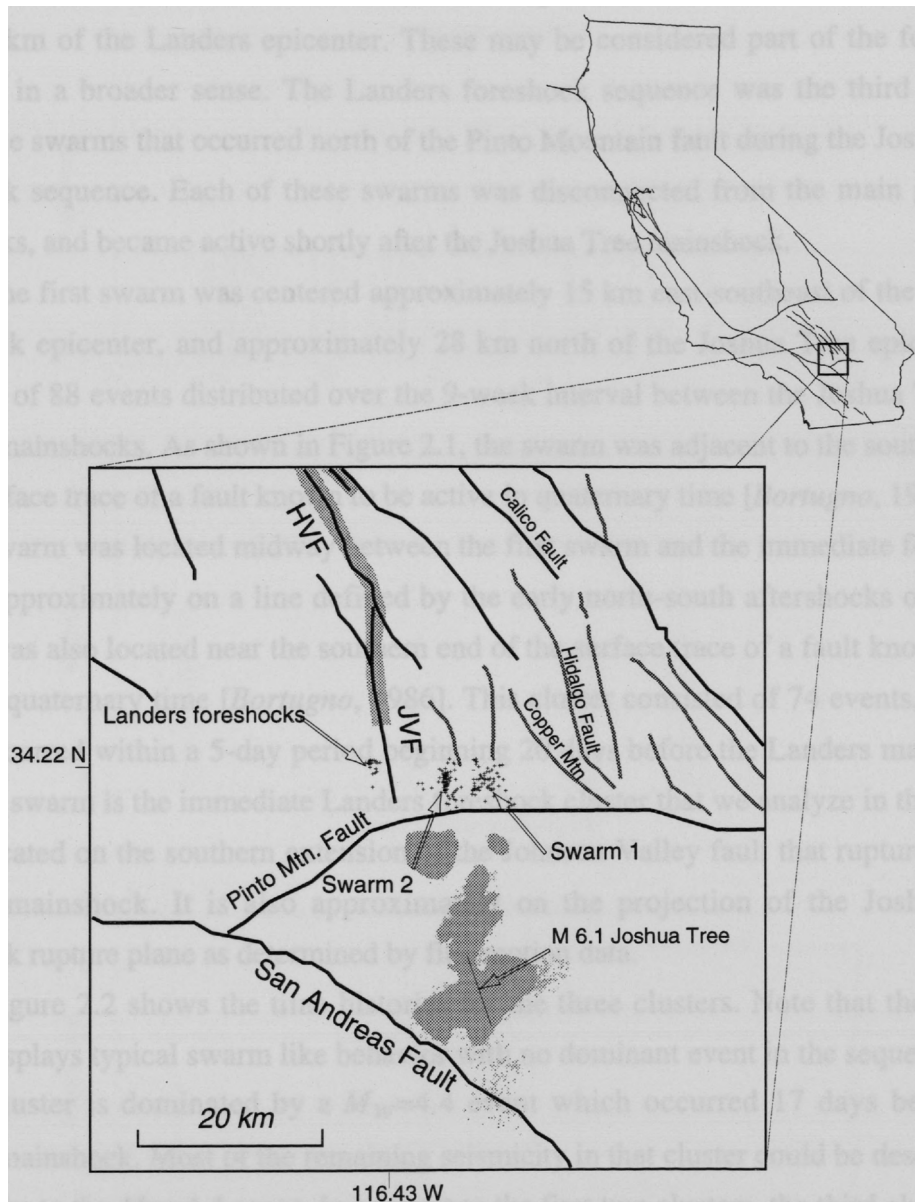
Figure 2.1. Base map centered on the Landers epicenter. The light gray regions south of the Pinto Mountain fault show the extent of aftershocks of the Joshua Tree earthquake. Just north of the Pinto Mountain fault are three swarms of preshocks to the Landers earthquake. The swarm which contains the immediate foreshocks to the Landers earthquake is just off the southern extension of the Johnson Valley fault (JVF). The fault segments which ruptured in the Landers earthquake are shown as heavy lines extending north along the JVF and the Homestead Valley fault (HVF).

between the date of the Joshua Tree mainshock (April 23) and June 28 and were located within 5 km of the Landers epicenter. These may be considered part of the foreshock sequence in a broader sense. The Landers foreshock sequence was the third of three earthquake swarms that occurred north of the Pinto Mountain fault during the Joshua Tree aftershock sequence. Each of these swarms was disconnected from the main group of aftershocks, and became active shortly after the Joshua Tree mainshock.

The first swarm was centered approximately 15 km east-southeast of the Landers mainshock epicenter, and approximately 28 km north of the Joshua Tree epicenter. It consisted of 88 events distributed over the 9-week interval between the Joshua Tree and Landers mainshocks. As shown in Figure 2.1, the swarm was adjacent to the southern end of the surface trace of a fault known to be active in quaternary time [*Bortugno*, 1986]. The second swarm was located midway between the first swarm and the immediate foreshock cluster, approximately on a line defined by the early north-south aftershocks of Joshua Tree. It was also located near the southern end of the surface trace of a fault known to be active in quaternary time [*Bortugno*, 1986]. This cluster consisted of 74 events, most of which occurred within a 5-day period beginning 20 days before the Landers mainshock. The third swarm is the immediate Landers foreshock cluster that we analyze in this paper. It was located on the southern extension of the Johnson Valley fault that ruptured in the Landers mainshock. It is also approximately on the projection of the Joshua Tree mainshock rupture plane as determined by first motion data.

Figure 2.2 shows the time histories for the three clusters. Note that the eastern cluster displays typical swarm like behavior with no dominant event in the sequence. The central cluster is dominated by a M_W=4.4 event which occurred 17 days before the Landers mainshock. Most of the remaining seismicity in that cluster could be described as aftershocks to the M_W=4.4 event. In contrast to the first two clusters, the third cluster was nearly aseismic until the day of the mainshock.
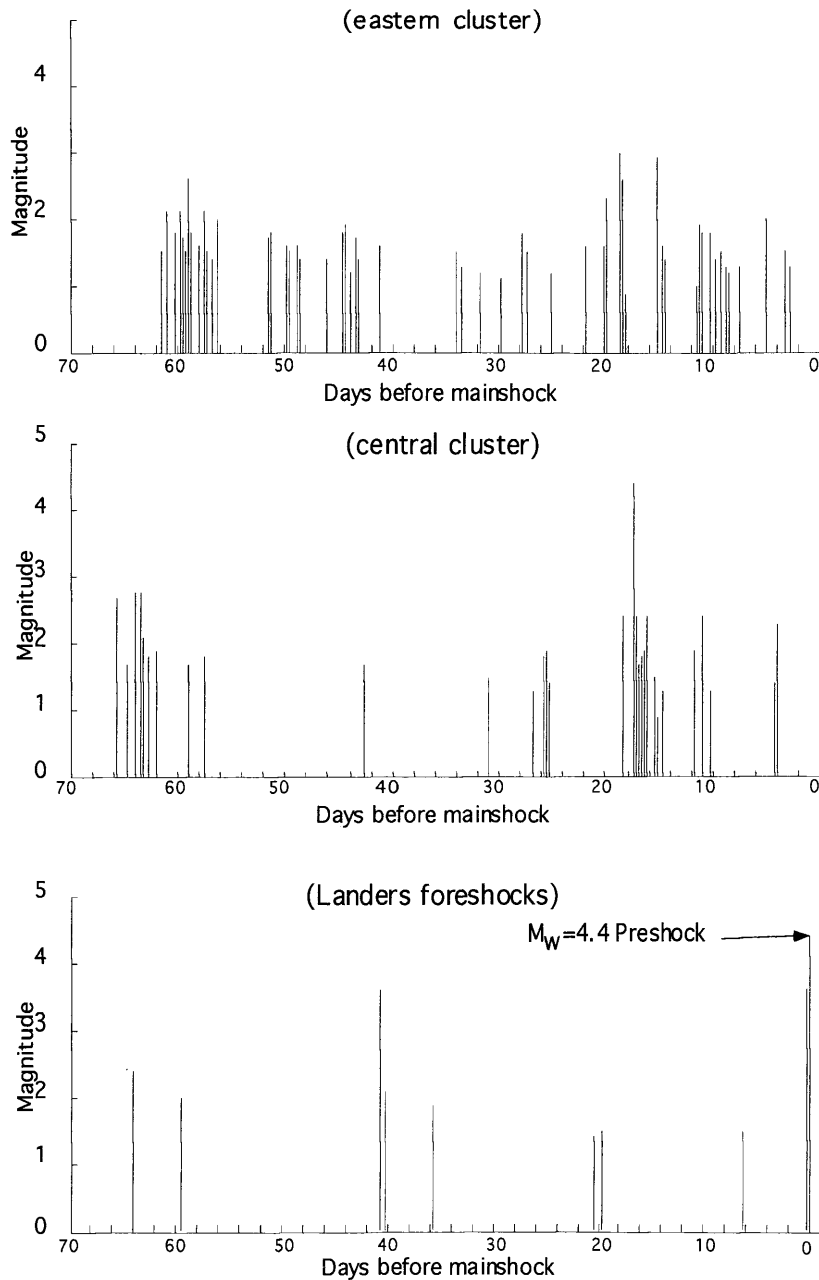
Figure 2.2. Time history of the three earthquake clusters near the Landers mainshock. The eastern cluster (farthest from epicenter) shows swarm like behavior with no well-defined dominant event. The central cluster is dominated by a *Mw*=4.4 event which has its own aftershock sequence. The cluster which includes the Landers foreshocks is nearly aseismic until the day of the mainshock.
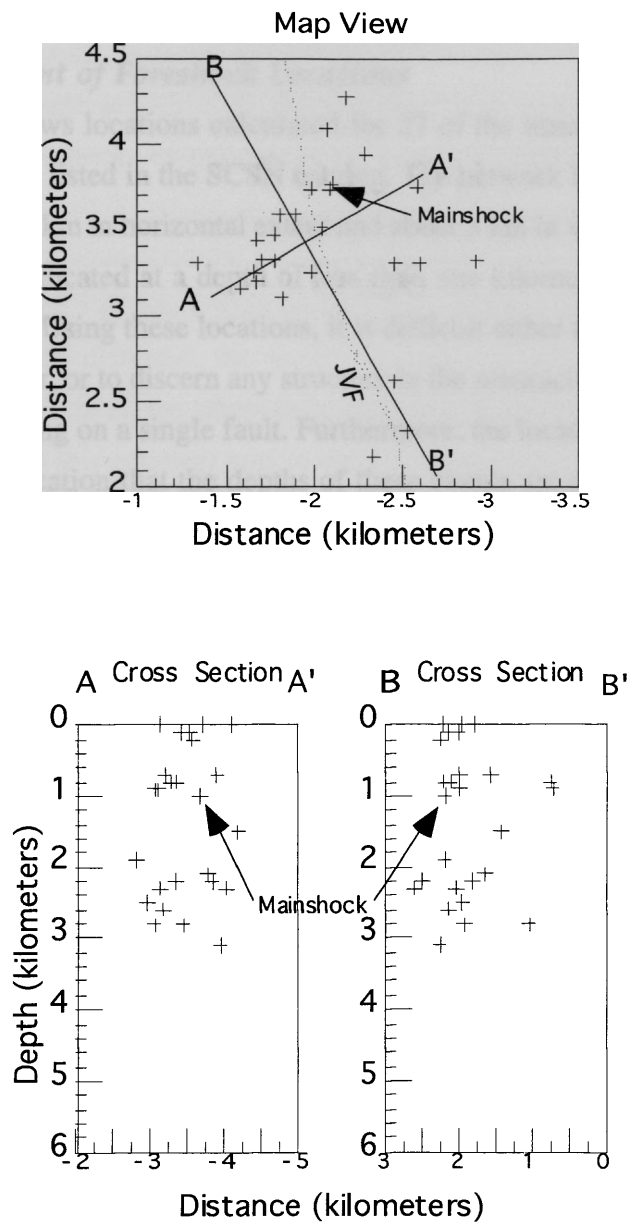
Figure 2.3. Locations of the immediate Landers foreshocks calculated by the Southern California Seismic Network. The top frame shows a map view of the events. The dotted line is the surface trace of the Johnson Valley fault. The lines A-A' and B-B' indicate the orientation of the two cross sections shown below. All distances are in kilometers.

2.3 Data Analysis

2.3.1 Improvement of Foreshock Locations

Figure 2.3 shows locations calculated for 27 of the immediate foreshocks to the Landers earthquake as listed in the SCSN catalog. The network locations define a diffuse cloud approximately 2 km in horizontal extent and about 3 km in vertical extent. About half of the foreshocks are located at a depth of less than one kilometer, and three events are located at the surface. Using these locations, it is difficult either to assess how close these events are to each other, or to discern any structure in the seismicity that would indicate the foreshocks are occurring on a single fault. Furthermore, the location of three events at the surface is a clear indication that the depths of these events are poorly constrained. Such errors are typical of network locations, and are due to a variety of factors including poor station distribution, inadequate velocity model, and inconsistent arrival time picks.

If only relative locations are required, as is often the case when studying clustered seismicity such as foreshocks, the problems with the velocity model can be minimized by using the arrival times to simultaneously estimate hypocenters, velocity model corrections, and station corrections. If the events are clustered in a small volume, the ray paths from all the events are virtually identical, and almost all the unmodeled velocity structure can be absorbed in the station corrections. We use the VELEST earthquake location program [*Ellsworth*, 1977; *Roecker, 1981*] to relocate the foreshocks in this study.

2.3.2 S Wave Picks and P Wave Picks By Waveform Cross Correlation

Because the immediate Landers foreshocks are clustered within a small volume, and because foreshocks have been observed to have very similar waveforms [e.g., *Ishida and Kanamori*, 1978], we expected that we could use cross correlation techniques to improve the precision of the *P* wave picks. Previously *Poupinet et al.*, [1984] and *Frémont and Malone* [1987] used a frequency-domain cross correlation technique to calculate differential *P* wave arrival times precise to a few milliseconds for similar events recorded by regional earthquake networks. *Frémont and Malone* [1987] used differential times to relocate a set of explosions with a precision of about 20 meters. *Deichmann and Garcia-Fernandez* [1992] used time domain cross correlation to relocate microearthquakes with a precision of a few tens of meters. *Dodge et al.* [1993] used frequency domain cross correlation to relocate a cluster of microearthquakes recorded by the US Geological Survey

(USGS) Calnet with a precision of a few tens of meters. The relocation procedures cited above are all master event procedures. With these procedures, a single event with clear arrivals that is similar to all the remaining events, is first located by conventional methods, and the remaining events are all relocated relative to the master. However, as we will show, the Landers foreshocks extend about 1700 m along strike and over a kilometer in depth. The foreshocks also do not lie on a single plane. Rather, they define a plane with a 500 m right step, and the earthquake focal mechanisms vary across the step. So, even though there are about 15 events within about 300 m of each other in the step, the focal mechanisms are slightly different, the waveforms are dissimilar, and there is no single event sufficiently similar to all the others to be used as a master event for cross correlation.

Our solution to this problem was to employ a technique developed by *VanDecar and Crosson* [1990] for determining relative arrival times of teleseisms recorded by a regional seismic network. This technique uses the cross correlations between all pairs of signals and a weighted least squares adjustment of the corresponding shifts to determine an optimum set of arrival time corrections and estimates of the errors in the resulting adjusted picks. The least squares weights are the maximum values of the inter channel cross correlation functions, so the corrections calculated for a given channel are influenced primarily by the channels most similar to the channel in question. Thus there is no requirement for a single event which is highly similar to all the other events.

At each station we begin with preliminary estimates of the P wave and S wave arrival times for all events and cross correlate each event against every other using windows centered around the estimated arrival. For each pair we determine the maximum and the shift corresponding to the maximum, and use this to construct a system of equations relating arrival time differences and cross correlation delays to a set of arrival time corrections. The system is solved by weighted least squares using a zero mean constraint on the arrival time corrections, and the arrival time corrections are then added to the estimated times. The error estimates for the improved picks are the standard deviations of the data residuals for each pick. See *VanDecar and Crosson* [1990] for details.

In most cases, only a subset of the events recorded at a given station are sufficiently similar to adjust this way. Accordingly, our implementation of this algorithm automatically removes events with mean cross correlation maxima less than a threshold value (usually 0.8). We also allow interactive removal of problematic traces. The removed
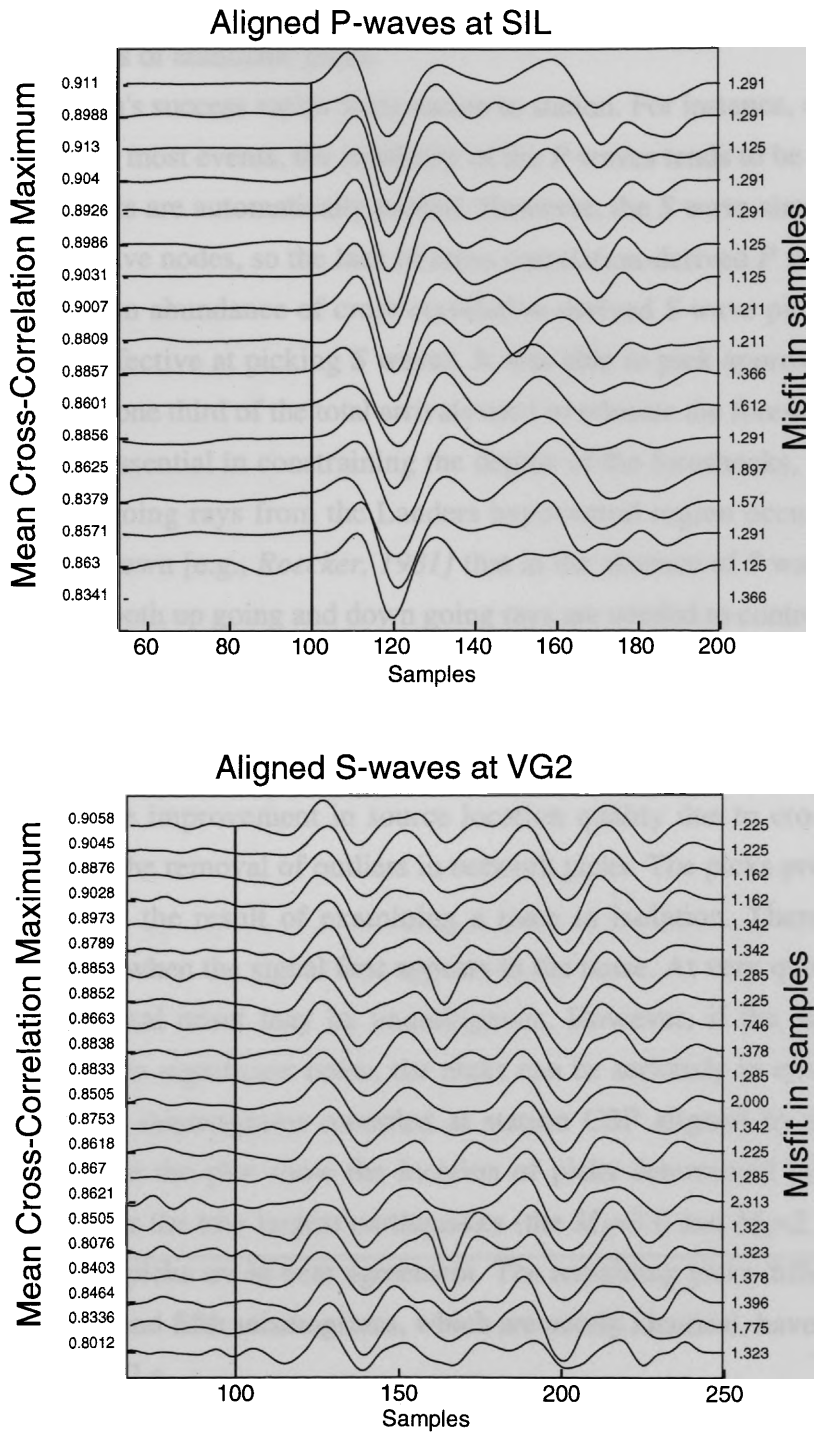
Figure 2.4. Examples of seismograms aligned by least squares adjustment of cross correlation-derived delays. The upper panel shows 2 s of *P* waves sampled at 100 samples per second. The lower panel shows 2.5 s of *S* waves sampled at 100 samples per second. The numbers on the left axes are the mean values of the cross-correlation maxima relative to all the other traces. The numbers on the right axes are the average values of the cross correlation delays relative to the other traces.

traces are then either picked by hand if the onsets are clear, or else are not used. Figure 2.4 shows some examples of automatic picks.

The algorithm's success varies from station to station. For instance, at stations near the P wave nodes for most events, the similarity of the P waves tends to be low and fewer than half of the events are automatically picked. However, the S wave similarity tends to be higher at the P wave nodes, so the lack of cross correlation-derived P wave picks may be compensated by an abundance of cross correlation derived S wave picks. In fact, the algorithm is quite effective at picking S waves. It was able to pick approximately 400 S wave arrivals (about one third of the total arrivals used to relocate the foreshocks). These S wave picks proved essential in constraining the depths of the foreshocks, since with our velocity model, up going rays from the Landers hypocentral region occur at only three stations. It is well known [e.g., *Roecker, 1981*] that in the absence of S wave readings, P wave readings from both up going and down going rays are needed to control the trade-off between origin time and depth.

The foreshock relocation results we present later, and a comparison of the picks produced by our algorithm to those produced by network analysts suggest that a significant part of the improvement in source location quality due to cross correlation picking results from the removal of outliers in network picks. The picks produced by the network analysts are the result of examining a trace in isolation. There is always a judgment made as to when the signal first appears in the noise. At very quiet sites, or for large events, the signal onset may be unambiguous. However, if the signal onset is emergent, or if there is significant noise, the picks can be seriously in error. Figure 2.5 shows the foreshock seismograms recorded at station CSP aligned by the automatic picker. The arrows on the plot show the location of picks determined by the network analysts. Note that for the two largest earthquakes (the M_L=3.0 and M_L=2.9 events) our picks and the analyst picks are in near agreement. The remaining picks differ by as much as 0.25 s. The fourth and fifth seismograms, which are nearly identical, have analyst picks that differ by about 0.2 s.
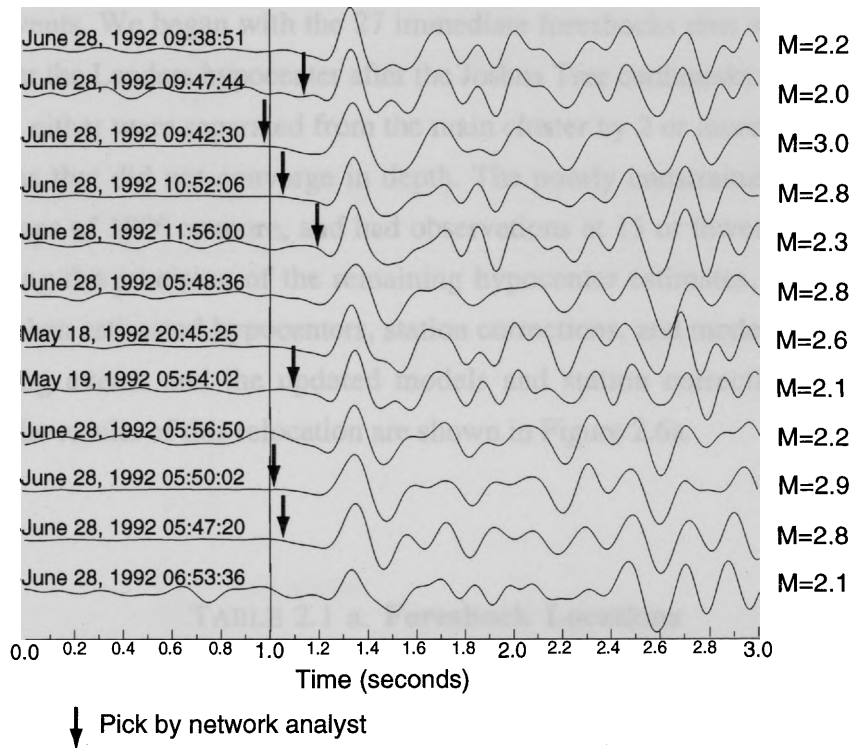
Figure 2.5. A comparison of *P* wave picks made by waveform comparison to those made by network analysts. These seismograms are from a set of 15 recorded at station CSP approximately 85 km distant from the foreshock cluster. The seismograms are shown aligned on the picks determined by waveform cross correlation. The down going arrows show the location of picks made by network analysts. Traces with no arrows were not picked by analysts

2.3.3 JHD Solutions Using Network Picks and Cross Correlation Picks

We first relocated the foreshocks by JHD using picks obtained from the SCSN database. The starting *P* wave velocity model was the *Hauksson et al.* [1994] model, and the starting *S* wave model was the *P* wave model scaled by $1/\sqrt{3}$. We only used observations out to 130 km from the epicenter. This restriction was applied so that the set of observations associated with smaller events would be comparable to that associated with the larger events. We began with the 27 immediate foreshocks plus six earthquakes that occurred near the Landers hypocenter after the Joshua Tree earthquake and the mainshock. Of these, 11 either were separated from the main cluster by 2 or more kilometers, or else had solutions that did not converge in depth. The poorly constrained solutions all had azimuthal gaps of 180° or more, and had observations at 15 or fewer stations. To avoid compromising the precision of the remaining hypocenter estimates, we removed these events. We then estimated hypocenters, station corrections, and model corrections, using the remaining events and the updated models and station corrections from the first inversion. The results of this relocation are shown in Figure 2.6a.

TABLE 2.1 a. **Foreshock Locations**

Events	Group	CUSP ID	Date	Time UT	Latitude °N	Longitude °W	Depth	Magnitude
1	1	2052770	May 18, 1992	2045:25.61	34.1868	116.4367	4.49	2.60
2	1	2052827	May 19, 1992	0554:02.50	34.1909	116.4388	4.64	2.10
3	1	2053369	May 23, 1992	1803:45.70	34.1905	116.4379	4.53	1.90
4	2	2056929	June 28, 1992	0521:30.59	34.2005	116.4403	4.35	2.00
5	2	2056931	June 28, 1992	0547:20.85	34.1974	116.4403	4.45	2.80
6	2	3031215	June 28, 1992	0548:05.00	34.1968	116.4402	4.34	2.80
7	2	3031226	June 28, 1992	0550:02.63	34.1935	116.4398	4.43	2.90
8	2	2056932	June 28, 1992	0554:41.04	34.1990	116.4393	4.22	3.60
9	2	3031167	June 28, 1992	0556:50.39	34.1929	116.4400	4.38	2.20
10	2	3031046	June 28, 1992	0558:38.46	34.1963	116.4409	4.55	2.80
11	2	2056934	June 28, 1992	0600:49.13	34.1952	116.4403	4.55	2.90
12	3	2056935	June 28, 1992	0630:00.19	34.1855	116.4362	4.02	1.80
13	3	2056937	June 28, 1992	0652:13.42	34.2007	116.4405	4.01	1.80
14	3	2056938	June 28, 1992	0653:36.88	34.1956	116.4408	4.65	2.10
15	4	2056953	June 28, 1992	0937:29.61	34.1937	116.4391	4.12	1.50
16	4	2056954	June 28, 1992	0938:51.16	34.1927	116.4403	4.48	2.20
17	4	2056955	June 28, 1992	0942:30.53	34.1937	116.4404	4.42	3.00
18	4	3031227	June 28, 1992	0947:29.24	34.1871	116.4364	3.75	2.00
19	4	2056956	June 28, 1992	0947:44.38	34.1909	116.4388	4.58	2.20
20	5	2056964	June 28, 1992	1052:06.49	34.1960	116.4411	4.68	2.80
21	5	2056965	June 28, 1992	1056:37.47	34.1930	116.4405	4.41	1.90
22	5	3031233	June 28, 1992	1057:24.00	34.1963	116.4424	3.93	1.60
23	6	2056970	June 28, 1992	1145:39.37	34.1956	116.4415	4.72	1.70
24	6	2056971	June 28, 1992	1156:00.33	34.1954	116.4412	4.70	2.30
25	6	3031111	June 28, 1992	1157:34.07	34.1990	116.4387	4.23	4.40

a) Relocations Using Network Picks

b) Relocations Using Improved Picks
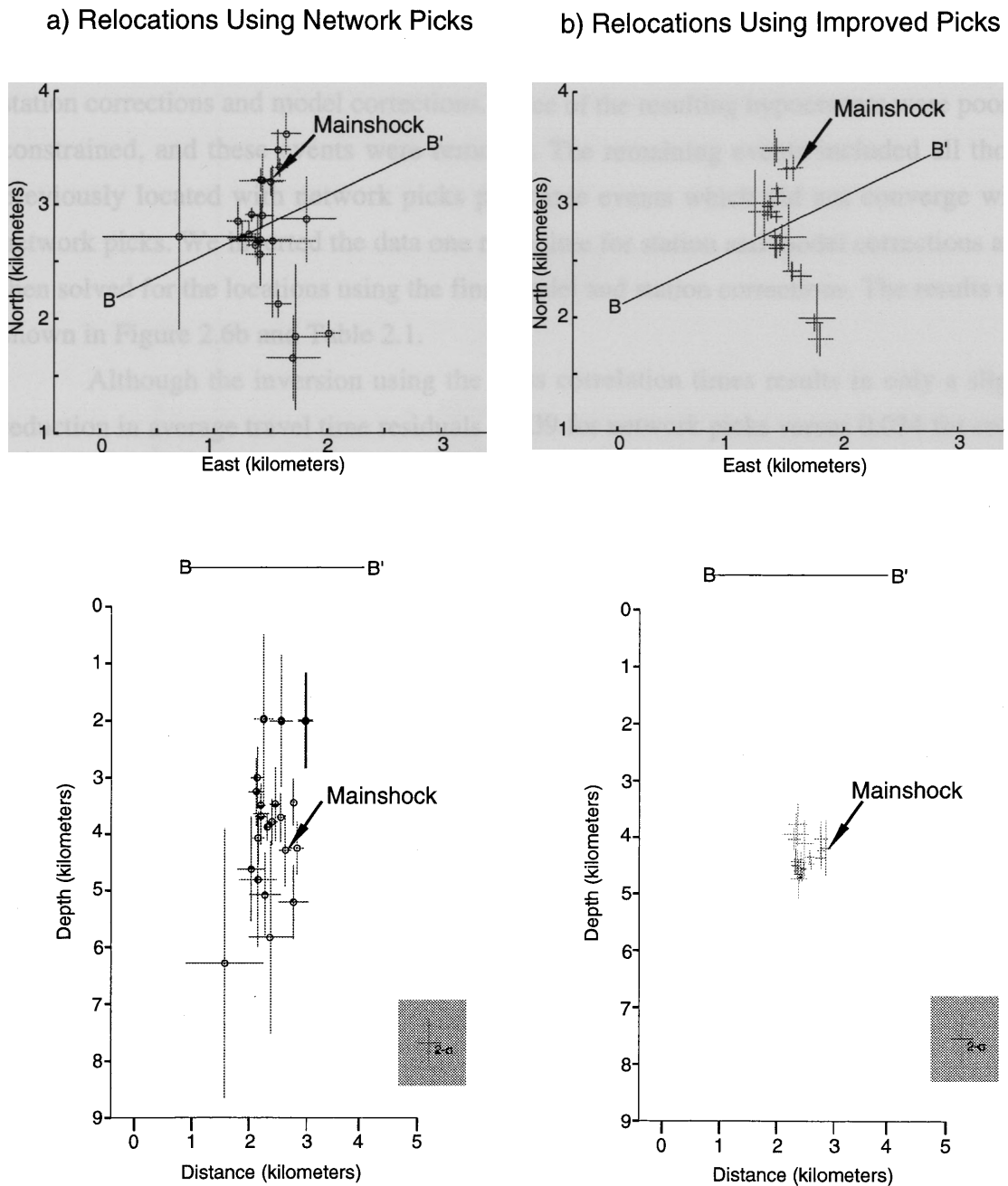
Figure 2.6. Relocated foreshocks in map and cross-sectional views. (a) The relocations made using JHD with network picks, and (b) the relocations made using JHD with *P* and *S* times determined by waveform cross correlation are shown. In both cases, the error bars are the 2σ limits for the coordinates. (top) A map view of the foreshocks is shown. (bottom) The cross sectional views A-A' defined on the map views of the epicenters are shown.

We determined improved arrival times by cross correlation for 28 events including the immediate foreshock and inverted these data starting with the previously obtained station corrections and model corrections. Three of the resulting hypocenters were poorly constrained, and these events were removed. The remaining events included all those previously located with network picks plus three events which did not converge with network picks. We inverted the data one more time for station and model corrections and then solved for the locations using the final model and station corrections. The results are shown in Figure 2.6b and Table 2.1.

Although the inversion using the cross correlation times results in only a slight reduction in average travel time residuals (0.039 for network picks versus 0.034 for cross correlation picks), there are significant reductions in the relative solution uncertainties. The standard errors in horizontal coordinates for JHD with network picks average 107 m. In depth they average 391 m. By contrast, the standard errors for JHD with cross correlation times average 52 m in horizontal coordinates and 100 m in depth. Undoubtedly, the improvement in depth control is due to the large number of cross correlation S wave picks. The reduction in horizontal uncertainty is probably due to the improved consistency of the P wave picks. Table 2.1b presents a more detailed comparison of the solution statistics.

Table 2.1 b. **Comparison of Network Picks and Cross Correlation Picks**

	Network Picks	Cross-Correlation Picks
Number of P observations	679	762
Number of S observations	26	403
Average observations per event	31	47
Average RMS, seconds	0.039	0.034
Average Gap	95°	54°
Average σ_x, meters	89	45
Average σ_y, meters	124	60
Average σ_z, meters	391	100

JHD is joint hypocenter determination.

The final hypocenters determined in this inversion are strongly clustered, both in map view and in depth. In particular, the vertical extent of the hypocenters is slightly over 1 km, rather than the 4 km seen in the JHD solutions with network picks. The relocated epicenters clearly define a narrow band of seismicity with a right step of about 0.5 km near the northern end of the sequence. The trend of the seismicity is similar to that of the Johnson Valley fault. All but two of the foreshocks occur to the south of the immediate foreshock.
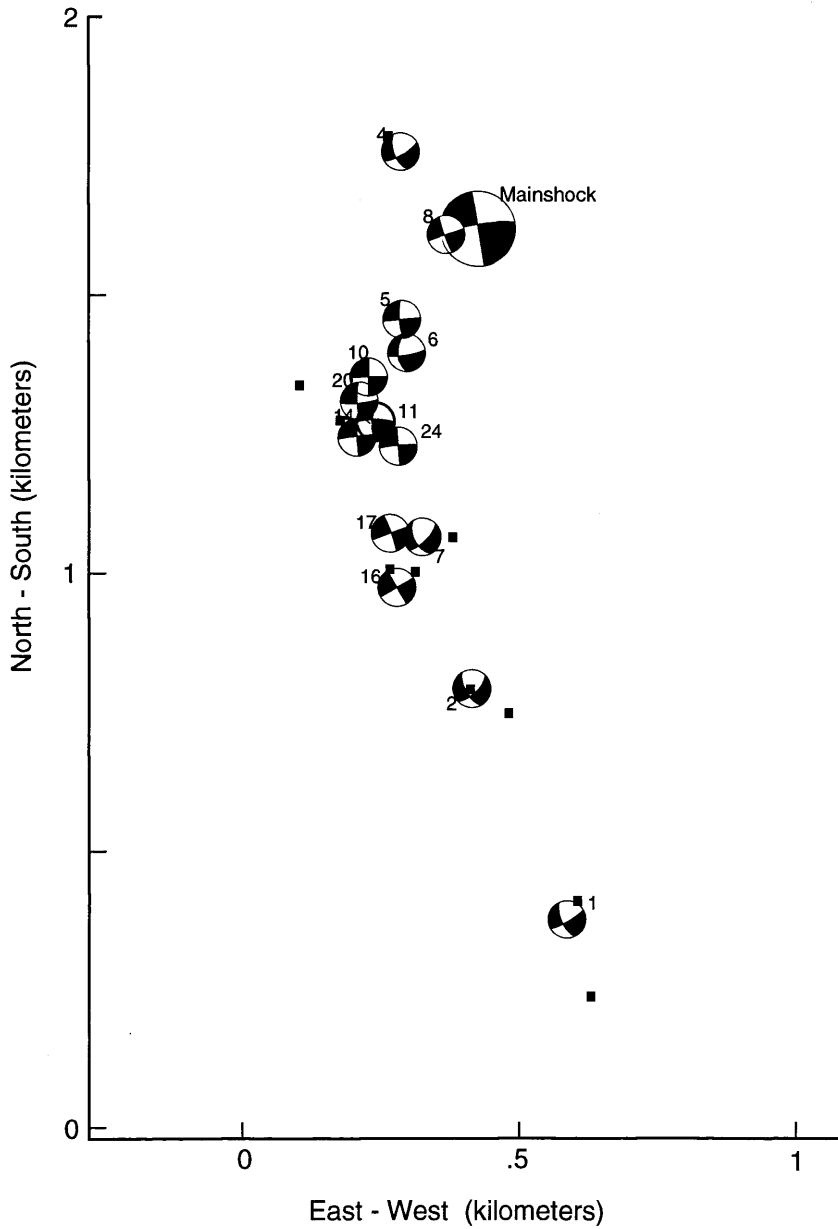
Figure 2.7. Fault plane solutions for 14 of the larger foreshocks and for the first of the two immediate foreshocks to the main rupture. Focal mechanisms were determined using the FPFIT program [*Reasenberg and Oppenheimer,* 1985]. The immediate foreshock (identified as Mainshock on the plot) symbol is shown larger than the other events, but otherwise, the symbol size is not proportional to magnitude.

We calculated focal mechanisms for 15 of the largest foreshocks using the FPFIT program [*Reasenberg and Oppenheimer*, 1985]. These are shown on a map of the foreshock locations in Figure 2.7. The focal mechanisms were determined using 18 to 41 first-motion polarities. Nearly all the observations plot near the equator of the focal sphere, so the dips are not well constrained. The average dip uncertainty is 26°. These events are primarily right-lateral strike-slip with average uncertainties of only 6° in strike. The focal mechanisms are remarkably consistent with the geometry determined from the foreshock relocations. The five events south of the jog have fault planes that strike 151° ± 3°. This is generally consistent with the strike of the seismicity south of the jog (140° to 145°). The three events north of the jog have fault planes that strike 163° ± 6°, again consistent with the strike of the seismicity (160°). The strike of the seven events in the jog is 178° ± 4°, a clockwise rotation of about 20° relative to the events outside the jog.

2.3.4 Source Parameter Determination

We determined stress drops for the larger foreshocks using the empirical Green's function technique of *Mori and Frankel* [1990]. For small earthquakes the corner frequency of the displacement spectrum may be controlled by site and propagation effects rather than by the earthquake source. A relatively uncorrupted estimate of the displacement spectrum may be obtained by using a much smaller, similar earthquake as an empirical Green's function to deconvolve the displacement spectrum from the spectrum of the larger earthquake [*Mueller, 1985; Frankel and Kanamori, 1983; Mori and Frankel,* 1990]. *Mori and Frankel* [1990] obtained successful deconvolutions for magnitude 3.4 to 4.4 earthquakes using Green's function events that were within 400 m of the event epicenters, and with magnitudes at least 1.3 units smaller than the event of interest. For these conditions they estimated an uncertainty of .02 seconds in the half widths of the deconvolved pulses.

We found three events of magnitude 1.8 to 2.0 that were within 400 to 500 m of most of the larger events, and used them to deconvolve displacement pulses at five stations within 100 km of the foreshock cluster. Because of the differences in focal mechanisms of the foreshocks, there is more *P* waveform variation near the nodal planes than near the center of the quadrants. To increase the range of usable events, we used SCSN stations CSP and SIL, which are within the northwest compressional quadrant for all the
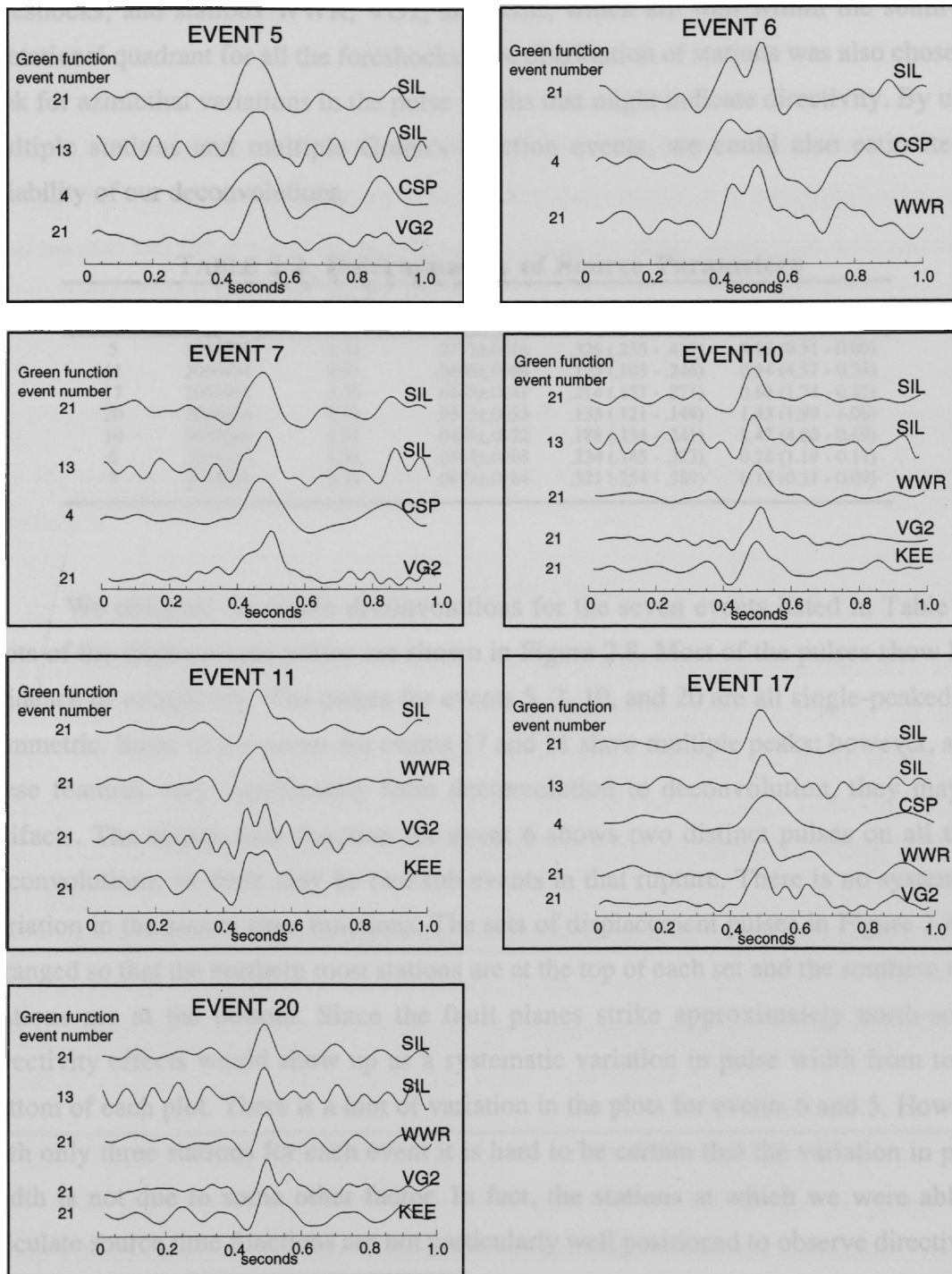
Figure 2.8. Source time functions determined for seven of the largest foreshocks. The displacement pulses were determined by deconvolving Green's function events from the displacement seismograms of the larger events. Deconvolutions were calculated using three different Green's function events at up to five stations. Each frame in this figure shows all the successful deconvolutions for one of the large foreshocks.

foreshocks, and stations WWR, VG2, and KEE, which are well within the southwest dilatational quadrant for all the foreshocks. The distribution of stations was also chosen to look for azimuthal variations in the pulse widths that might indicate directivity. By using multiple stations and multiple Green's function events, we could also estimate the reliability of our deconvolutions.

TABLE 2.2. **Determination of Source Parameters**

Event	CUSP ID	$M_0 *10^{13}$ Nm	$\tau_{1/2}$, s	a, km	$\Delta\sigma$, MPa
5	2056931	1.51	.0717±.0216	.326 (.235 - .417)	0.19 (0.51 - 0.09)
11	2056934	2.51	.0406±.0166	.175 (.103 - .246)	0.94 (4.57 - 0.34)
17	2056955	3.55	.0549±.0147	.214 (.157 - .271)	0.68 (1.74 - 0.33)
20	2056964	1.51	.0313±.0033	.135 (.121 - .149)	1.43 (1.99 - 1.06)
10	3031046	1.51	.0429±.0122	.188 (.134 - .241)	1.47 (4.00 - 0.69)
6	3031215	1.51	.0548±.0208	.234 (.145 - .323)	0.28 (1.19 - 0.11)
7	3031226	2.51	.0873±.0184	.321 (.254 - .389)	0.15 (0.31 - 0.09)

We obtained 30 usable deconvolutions for the seven events listed in Table 2.2. Plots of the displacement pulses are shown in Figure 2.8. Most of the pulses show little evidence of complexity. The pulses for events 5, 7, 10, and 20 are all single-peaked and symmetric. Some of the pulses for events 17 and 11 show multiple peaks; however, since these features vary significantly from deconvolution to deconvolution, they may be artifacts. The source time function for event 6 shows two distinct pulses on all three deconvolutions, so there may be two sub events in that rupture. There is no systematic variation in the source time functions. The sets of displacement pulses in Figure 2.8 are arranged so that the northern most stations are at the top of each set and the southern most stations are at the bottom. Since the fault planes strike approximately north-south, directivity effects would show up as a systematic variation in pulse width from top to bottom of each plot. There is a hint of variation in the plots for events 6 and 5. However with only three stations for each event it is hard to be certain that the variation in pulse width is not due to some other factor. In fact, the stations at which we were able to calculate source time functions are not particularly well positioned to observe directivity-induced variations in the source time functions particularly if rupture is bilateral, since they span only about 90° of azimuth relative to the sources.

We estimated the stress drops for the seven events following *Mori and Frankel* [1990]. The source radius, *a,* was calculated using an expression from *Boatwright* [1980] for a circular source,

$$a = \frac{\tau_{\frac{1}{2}} \upsilon}{1 - \upsilon \sin \theta / c(x_0)} \quad , \tag{2.1}$$

where $\tau_{\frac{1}{2}}$ is the risetime of the displacement pulse, υ is the rupture velocity (assumed to be 3.4 kms^{-1}), $c(x_0)$ is the local P wave velocity (6.1 kms^{-1}) and θ is the angle between the fault normal and the P wave takeoff direction. Then the static stress drop was calculated using an expression from *Brune* [1970],

$$\Delta\sigma = \frac{7}{16} \frac{M_0}{a^3} \quad . \tag{2.2}$$

For M_0 we converted the SCSN magnitudes to moments in Newton meters using the expression

$$\log M_0 = 1.5M + 9.05 \quad . \tag{2.3}$$

The risetime we used was a simple average of individual risetime measurements for all deconvolutions of each event. Because the stress drop depends on the cube of the source radius, estimates of the stress drop are very sensitive to errors in the pulse width. Thus although our nominal values for stress drop for the seven events range from 0.15 MPa to 1.47 MPa, the range of stress drops corresponding to a 1 σ variation in risetime is 0.09 to 4.57 MPa.

All the events with stress drop estimates are in the fault jog. Although these stress drops might not be appropriate for events well to the north or south of the jog, those more distant events have a very small effect on the static stress changes that we calculate for events in the jog, and with the exception of event 1 are not used.

2.4 Spatiotemporal Development of the Foreshock Sequence

For purposes of discussion we have divided the foreshocks into six groups. The group 1 foreshocks began in the hypocentral region weeks before the mainshock, and the mechanical relation of these early foreshocks to the eventual mainshock is unclear. Figure 2.9 shows the three early occurring foreshocks to be farther south than most of the other foreshocks. Their only obvious connection to the rest of the sequence is that they occurred on (apparently) a fault plane common to most of the other foreshocks, and the existence of later foreshocks as far south as event 1.
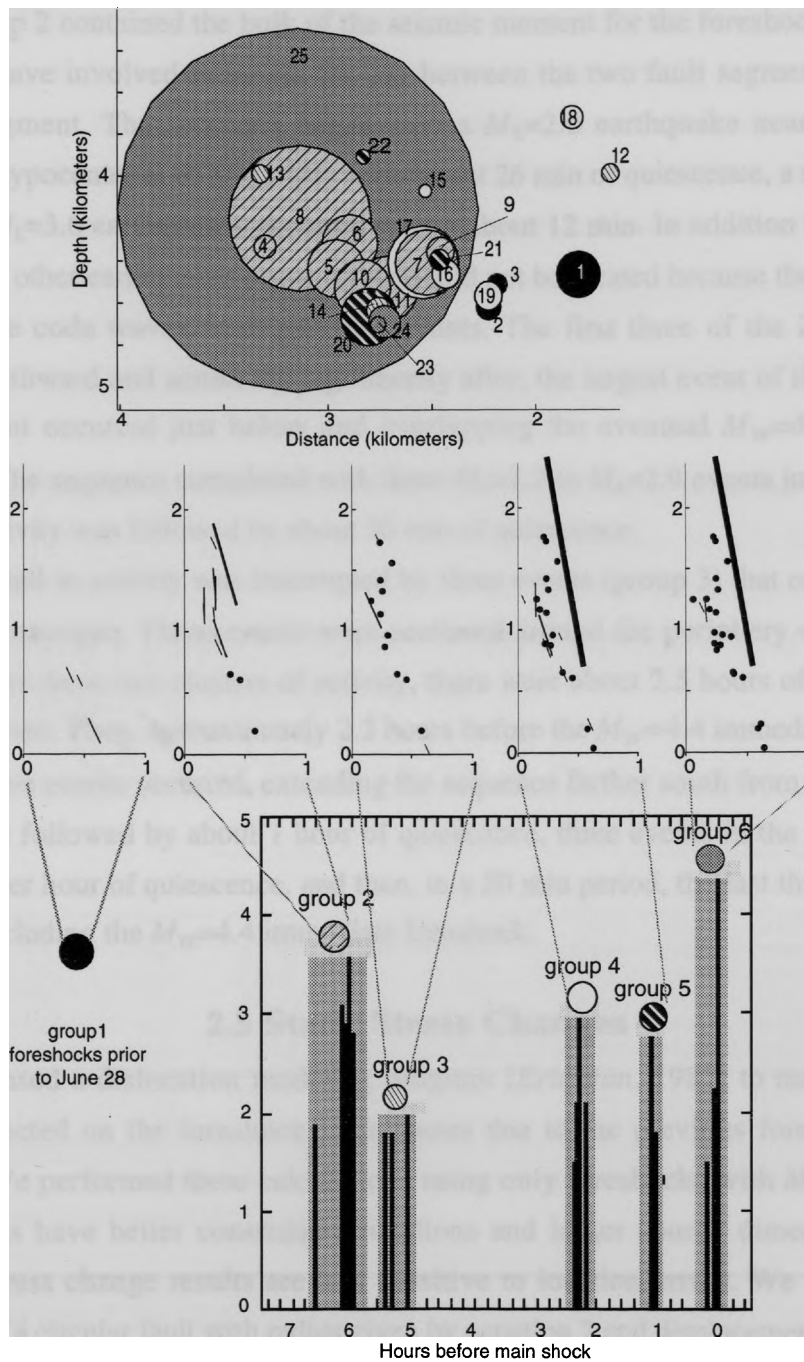
Figure 2.9 . Spatial and temporal distribution of foreshocks. (top) Foreshocks projected on a north-south plane. Dimensions based on 3 MPa stress drop. Shading of events corresponds to bottom key . (middle) Map views of foreshocks for time intervals defined. Foreshocks in each frame shown as bars scaled to source dimensions of the foreshocks with orientations equal to inferred or measured strikes. Foreshocks that occurred in previous time frames are shown as dots. (bottom) The temporal distribution of events in the 7 hours preceding the mainshock.

Group 2 contained the bulk of the seismic moment for the foreshock sequence. It appears to have involved failure in the jog between the two fault segments and on the northern segment. The sequence began with a M_L=2.0 earthquake near the eventual mainshock hypocenter at 0521:31 UT. After about 26 min of quiescence, a series of seven M_L=2.2 to M_L=3.6 earthquakes occurred within about 12 min. In addition to these seven earthquakes, other earthquakes occurred but could not be located because their onsets were buried in the coda waves from previous events. The first three of the located events ruptured southward and across the jog. Shortly after, the largest event of the sequence, a M_L=3.6 event occurred just below and overlapping the eventual M_W=4.4 immediate foreshock. The sequence completed with three M_L=2.2 to M_L=2.9 events just south of the jog. This activity was followed by about 30 min of quiescence.

The lull in activity was interrupted by three events (group 3) that occurred over a 23 minute time span. These events were scattered around the periphery of the group 2 activity. After these two clusters of activity, there were about 2.5 hours of quiescence at the M≥2.0 level. Then, approximately 2.3 hours before the M_W=4.4 immediate foreshock, a series of five events occurred, extending the sequence farther south from the jog (group 4). This was followed by about 1 hour of quiescence, three events in the jog (group 5), nearly another hour of quiescence, and then, in a 20 min period, the last three foreshocks (group 6) including the M_W=4.4 immediate foreshock.

2.5 Static Stress Changes

We used a dislocation modeling program [*Erickson*, 1987] to model the stress change expected on the foreshock fault planes due to the previous foreshocks in the sequence. We performed these calculations using only foreshocks with $M_L > 2.6$. These larger events have better constrained locations and larger source dimensions, so the Coulomb stress change results are less sensitive to location errors. We modeled each foreshock as a circular fault with radius given by equation 2 and displacement of a constant stress drop shear crack [*Keilis-Borok*, 1959]

$$\Delta u(r) = \frac{24}{7\pi}\sqrt{a^2 - r^2}. \qquad (2.4)$$

Here a is the radius of the fault, and r is the point at which slip is evaluated. All the foreshocks were modeled as vertical strike-slip earthquakes with strike direction based on

the focal mechanism for that event. The fault plane for each foreshock was discretized on a 21x21 grid with displacement on each element scaled according to the relation given above. The stress tensor due to the cumulative dislocation of the preceding events was calculated on a 21x21 grid superimposed on each foreshock fault plane, and at each grid point, the shear tractions resolved in the direction of slip and normal to the fault plane were determined from the stress tensor after *Beroza and Zoback* [1993]. From these we calculated a Coulomb failure criterion

$$F = \tau_s - \mu_0 \sigma_n .$$ (2.5)

Here τ_s is the shear traction increase, σ_n is the normal stress increase, and μ_0 is the coefficient of friction. F values greater than zero imply that the fault is moved closer to failure by the change in stress. On the basis of the stress drop estimates of a previous section, we decided to model the static stress changes using uniform stress drops of 1 and 3 MPa. The average values are presented in Table 2.3.

TABLE 2.3. **Resolved Stress Increase on Foreshock Fault Planes**

		1-MPa Stress Drop			3-MPa Stress Drop		
Event	Magnitude.	τ_s	σ_n	F	τ_s	σ_n	F
5	2.80	0.0007	0.0002	0.0009	0.0007	0.0002	0.0009
6	2.80	-0.0262	0.1345	0.0545	-0.2165	0.0120	-0.2093
7	2.90	0.0322	-0.0156	0.0228	0.0795	-0.0541	0.0470
8	3.60	-0.0313	0.0221	-0.0180	-0.0484	0.0506	-0.0181
10	2.80	-0.2873	0.1365	-0.2054	-0.2378	0.5030	0.0640
11	2.90	-0.3709	0.4378	-0.1083	-0.4767	0.5168	-0.1666
17	3.00	-0.4601	0.2704	-0.2979	-0.6562	0.1101	-0.5902
20	2.80	-0.3523	-0.0973	-0.4107	-0.3111	0.0094	-0.3055
25	4.40	-0.0393	0.0095	-0.0336	-0.0716	-0.0023	-0.0730

Here τ_s is the shear traction increase, σ_n is the normal traction increase, and F is the Coulomb stress for a coefficient of friction of 0.6.

Notice that of the nine events analyzed, seven of the foreshocks (for both the 1 and 3 MPa cases) slipped in the opposite direction to the cumulative shear traction change on the fault plane. Of the two foreshocks with a shear traction increase in the direction of slip, one had an increase of less than 0.001 MPa.

The Coulomb failure criterion results follow the shear traction results. For both the 1 and 3 MPa stress-drop cases, six foreshocks out of nine had a negative F value and one had an increase in F of less than 0.001 MPa. These results are not surprising, given the geometry of the sequence. Crack models predict a decrease in shear stress to the side of a

crack within a distance of one crack length after shear failure [*Das and Scholz*, 1982]. Event 6 is subparallel and immediately adjacent to event 5. Event 10 is parallel and adjacent to both events 5 and 6. Event 11 is in the shear stress-decrease zone of event 10, event 25 overlaps event 8, and so on. These results suggest that stress transfer from earlier events in the foreshock sequence was not important in triggering the larger foreshocks, although it is possible that adjustment of the foreshock locations and focal mechanisms within their confidence limits could change this conclusion in some cases.

The results for event 25, the immediate foreshock (M_W= 4.4) are much more definite. In this instance the location errors are much smaller than the size of the fault plane (860 to 1300 m in radius depending on the stress drop). The shear and normal traction changes on the fault plane of event 25 are dominated by the effects from the largest foreshock (event 8 in Figure 2.10), but the trend for all events is to decrease the shear traction in the direction of slip and to decrease the Coulomb failure criterion. These results are unlikely to be changed by adjustment of the foreshock locations within their error bounds, since the bounds are about an order of magnitude smaller than the size of the fault plane for event 25.

Although there was a net decrease in Coulomb stress on the fault plane of event 25, there were local regions of stress increase. It is possible that rupture could have initiated in one of these regions of stress increase. Although this scenario cannot be dismissed, we think it is unlikely since, for the most part, the regions of stress increase are outside the 2σ confidence limits for the immediate foreshock hypocenter location (Figure 2.11).
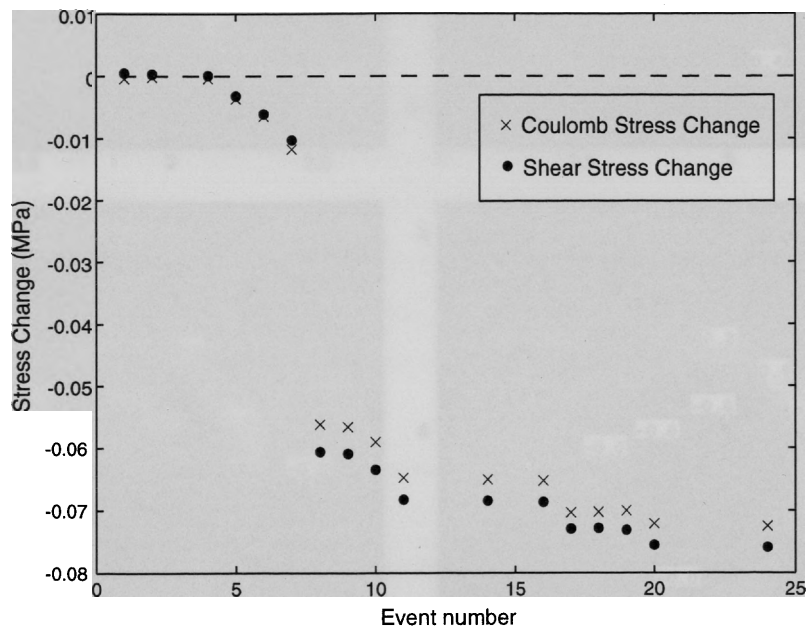
Figure 2.10. Cumulative change on the M_W=4.4 immediate foreshock fault plane. Stresses are calculated assuming a 3 MPa stress drop for all events and using only events with $M_L > 2.6$. The values shown on the plot are the median of the cumulative stress at each time step. The solid circles show the shear traction change in the direction of slip, and the crosses show the Coulomb stress change calculated assuming a coefficient of friction of 0.6. This shows that the foreshocks are driving the mainshock hypocenter further from failure.
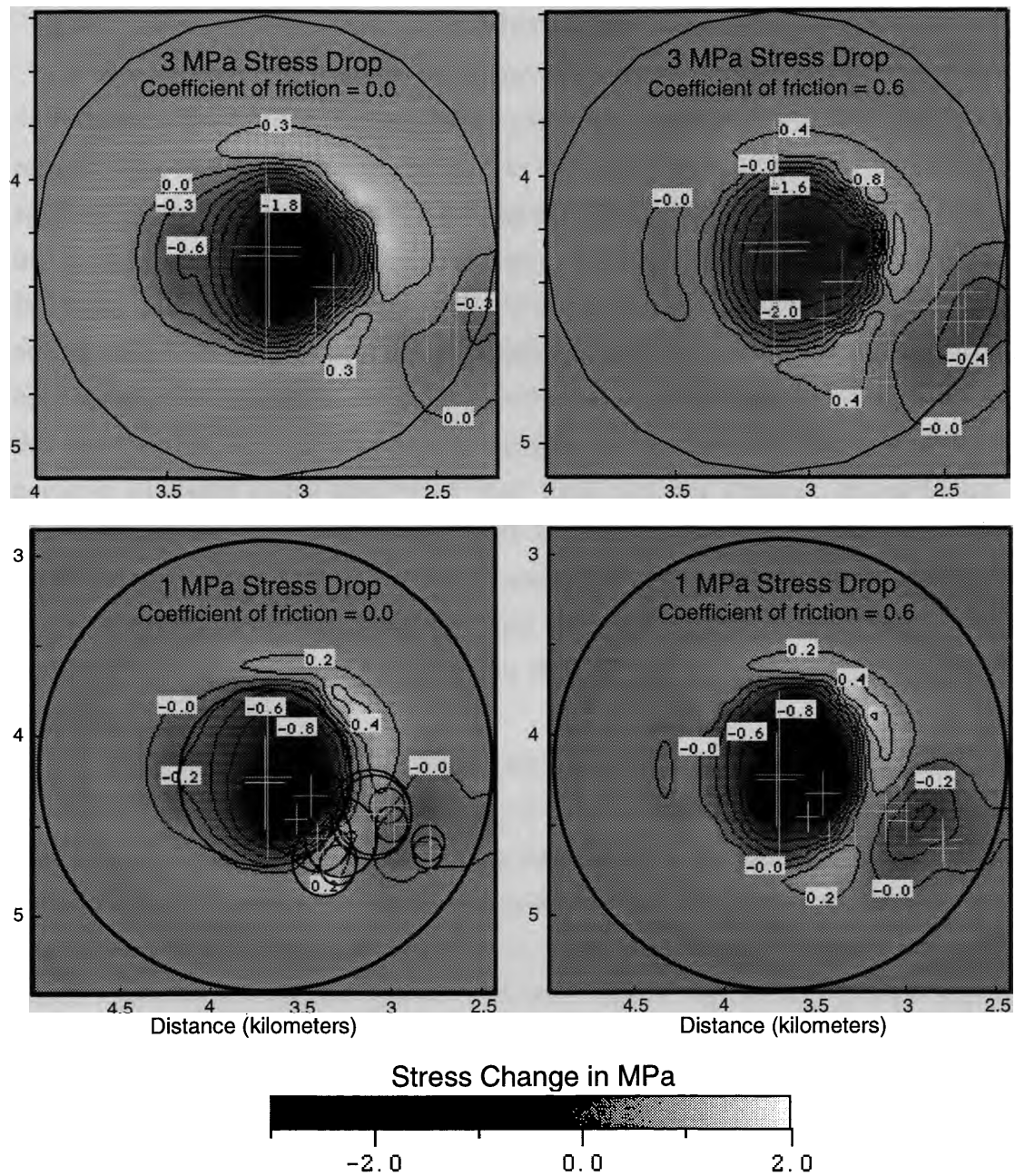
Figure 2.11. Stress change on the M_W=4.4 immediate foreshock fault plane. (top) The Coulomb stress change calculated assuming a 3 MPa stress drop for all foreshocks. (bottom) The Coulomb stress change calculated assuming a 1 MPa stress drop. (left) The Coulomb stress change calculated assuming a zero coefficient of friction is shown. (right) The Coulomb stress change calculated assuming a 0.6 coefficient of friction is shown. The crosses show the 2σ limits for the foreshock hypocenter locations. All distances are in kilometers.

2.6 Discussion

It is interesting to compare our observations of the Landers sequence with models of foreshock generation. *Jones* [1984] proposed a model in which a population of asperities fail by delayed multiple rupture. In this model the failure of each asperity causes additional stress to be applied to neighboring asperities, which then fail by static fatigue. If this model is applicable, then there should be a net shear stress increase on each foreshock fault plane prior to the occurrence of that event. Our results suggest that the foreshocks did not, in general, trigger each other. Although some of the smaller foreshocks may have been triggered by their immediate predecessors, most of the large foreshocks, for which the uncertainties in location are small, relative to the rupture dimension, either have negative Coulomb stress changes or very small positive changes. In particular, the M_W=4.4 immediate foreshock rupture plane is almost certain to have been destressed by the foreshocks that preceded it. It is worth noting that, had the foreshocks all occurred on a single plane with similar slip directions, they would have acted to trigger each other. It is the three dimensionality of the sequence that allows us to infer another process is operating.

If the foreshocks did not trigger each other, then they must have occurred in response to something else. One possibility is that the nucleation region was weakened by fluid flow [*Sibson*, 1992]. Another possible mechanism is loading by aseismic creep over the nucleation region. Aseismic creep during the nucleation process is predicted by several models of earthquake nucleation [*Dieterich*, 1992; *Ohnaka*, 1992]. The behavior of the Landers foreshock sequence (growth with time, size of region) may provide important constraints on these models.

The geometry of the foreshocks and their focal mechanisms is consistent with right-lateral creep having occurred on the two fault segments bounding the jog. *Segall and Pollard* [1980] showed that right-lateral earthquakes occurring within a dilatational jog should have a clockwise rotation of focal mechanisms due to the local perturbation to the stress field from slip on the adjacent fault segments. The first events of the immediate foreshock sequence (group 2) occurred in the jog and were rotated clockwise relative to the strike of the seismicity outside the jog. If the rotations are due to a local stress perturbation, then there must have been some slip north and south of the jog prior to the foreshock activity. A search of the SCSN catalog from 1981 revealed just two events of $M_L > 2.5$ within 2 km of the jog, and both of those were to the southeast and nearly 2 km

distant. Thus the loading of the jog, if it occurred within the 11 years prior to the Landers earthquake, is likely to have been by aseismic creep. An alternative explanation is that the focal mechanisms are controlled by preexisting fault geometry.

Ohnaka [1992] has proposed a theory of foreshock generation in which foreshocks result from failure of asperities loaded by accelerating premonitory creep. In this model, earthquake nucleation begins at a point on the fault where resistance to rupture growth is a minimum. Quasistatic creep begins there and grows outward until a critical dimension is achieved at which point resistance to further growth is exceeded by the stress change, and dynamic instability begins. In this model, foreshocks occur at asperities within the nucleation zone, and as the nucleation zone grows with time, the zone of foreshocks may also grow.

The Landers foreshocks were concentrated within a releasing fault jog, a weak point on the fault because of reduced normal stress. In this respect they are consistent with the Ohnaka model. If it is true that they were driven by aseismic creep, then this is also consistent with Ohnaka's model. However, there are notable inconsistencies between our observations and the behavior this model predicts. For instance, the group 1 events occurred near the southern end of the foreshock zone, yet they were the first events of the extended foreshock sequence. This is inconsistent with a model in which creep nucleates at the fault jog and expands from there. We could argue that since the group 1 events occurred days before the mainshock, they are not genetically related to the rest of the foreshocks. However, they occurred on the same fault plane as most of the other foreshocks, and foreshock number 12 actually occurred south of foreshock number 1, so it seems likely that the group 1 events were part of the nucleation process. Group 1 events aside, there is still very little indication that the zone of foreshocks expanded with time as predicted by the *Ohnaka* [1992] model. The group 2 events, which started the immediate foreshock sequence, span an area (in profile) that is over half that spanned by the entire sequence. In other words, the foreshock zone either did not grow significantly with time as required by the Ohnaka model, or else it expanded aseismically. These inconsistencies may reflect the difficulty of applying a two-dimensional theory of nucleation to a fault with three-dimensional geometry.

Other earthquakes have been observed to nucleate on or near a geometric complexity of a fault. For instance, *Bakun et al.* [1980] gave several examples of central California earthquakes which nucleated near fault bends. *Jones et al.* [1982] concluded that

the 1975 Haicheng (M_L=7.3) earthquake probably nucleated at an en echelon fault step. *Jones* [1984] showed that of seven California earthquakes with foreshock sequences, four of the earthquakes were associated with fault zone discontinuities, and the other three were possibly associated with fault zone discontinuities. *Lindh et al.* [1978] observed a change in the ratios of P wave amplitudes to S wave amplitudes between foreshocks and aftershocks for three California earthquakes, which they attributed to a systematic change in stress or fault orientation in the source region.

Our results for the Landers foreshocks and results from the studies cited above suggest that fault zone geometry can be an essential factor in earthquake nucleation. Such geometry can be easily missed, if the size of the irregularity is less than the uncertainties in the hypocenter locations. More high-resolution studies of foreshock sequences should reveal if rupture nucleation is commonly associated with fault zone discontinuities. If earthquakes often nucleate at strength heterogeneities, then it may be necessary to include the effects of three-dimensional fault structure in realistic models of earthquake nucleation.

2.7 Summary

We have relocated 24 foreshocks and the immediate foreshock to the 1992 Landers M_W=7.3 earthquake using P and S wave picks determined by waveform cross correlation. The relative event locations have 2σ uncertainties which are less than 100 m horizontally and 200 m vertically for most events. The relative locations clearly define a near-vertical fault striking approximately 330° with a right step of about 500 m. The geometry derives independent support from focal mechanisms determined for 15 of the largest events. All focal mechanisms are predominantly right-lateral strike slip on vertical planes with strikes that follow the trend of the seismicity. Within the jog, the focal mechanisms rotate clockwise, which is consistent with the expected rotation of the stress field for a right-stepping jog on a right-lateral fault [*Segall and Pollard*, 1980]. Stress drops were determined for six events in or near the jog, and these are all of the order of 1.0 MPa. The immediate foreshock sequence is discontinuous with five distinct temporal clusters and one quiescent period of about 2.5 hours. The first two of these clusters results from the failure of the jog, and the third from extension of the sequence along the southern segment. The final two clusters, which include the M_W=4.4 immediate foreshock to the mainshock, show no systematic relation to the previous seismicity. Modeling of the Coulomb stress change caused by previous foreshocks resolved on the foreshock fault planes suggests that

the sequence was not driven by the stress changes caused by the foreshocks alone. We suggest that the foreshock sequence may have been driven by aseismic creep over the nucleation zone, which is at least as large as the foreshock zone, and that the foreshocks themselves punctuate this larger process. The close association of the Landers foreshocks with the jog in the Johnson Valley fault indicates that the jog may have strongly influenced the nucleation process. If future high-resolution studies of foreshock sequences show that geometric complexities are involved, then it may be necessary to include such complexities in models of rupture nucleation.

Chapter 3 — Detailed observations of California foreshock sequences: Implications for the earthquake initiation process

Abstract

We find that foreshocks provide clear evidence for an extended nucleation process before some earthquakes. In this study, we examine in detail the evolution of six California foreshock sequences, the 1986 Mount Lewis (M_L = 5.5), the 1986 Chalfant (M_L = 6.4), the 1986 Stone Canyon (M_L = 4.7), the 1990 Upland (M_L = 5.2), the 1992 Joshua Tree (M_W = 6.1), and the 1992 Landers (M_W = 7.3) sequence. Typically, uncertainties in hypocentral parameters are too large to establish the geometry of foreshock sequences and hence to understand their evolution. However, the similarity of location and focal mechanisms for the events in these sequences leads to similar foreshock waveforms that we cross correlate to obtain extremely accurate relative locations. We use these results to identify small-scale fault zone structures that could influence nucleation and to determine the stress evolution leading up to the mainshock. In general, these foreshock sequences are not compatible with a cascading failure nucleation model in which the foreshocks all occur on a single fault plane and trigger the mainshock by static stress transfer. Instead, the foreshocks seem to concentrate near structural discontinuities in the fault and may themselves be a product of an aseismic nucleation process. Fault zone heterogeneity may also be important in controlling the number of foreshocks, i.e., the stronger the heterogeneity, the greater the number of foreshocks. The size of the nucleation region, as measured by the extent of the foreshock sequence, appears to scale with mainshock moment in the same manner as determined independently by measurements of the seismic nucleation phase. We also find evidence for slip localization as predicted by some models of earthquake nucleation.

3.1 Introduction

A key question in earthquake source mechanics is how do earthquakes begin. Do big earthquakes begin in the same manner as small earthquakes, or is there something different about the initiation process of large versus small events? If there is a difference, then large earthquakes may be predictable. Otherwise, earthquake prediction might require more detailed knowledge of the stress and strength distributions on faults than we are ever likely to have. Experimental and theoretical work [e.g., *Das and Scholz,* 1981*; Dieterich,* 1986, *1992; Ohnaka,* 1992*; Yamashita and Ohnaka,* 1991] indicates that earthquakes should be preceded by quasi-static slip within a nucleation zone. If real earthquakes begin this way and if the slip extent of the nucleation zone is sufficiently large, then it might be possible to detect the nucleation process. Observations to date have failed to detect direct evidence of the nucleation process such as a strain signal generated by aseismic slip prior to earthquakes [*Johnston et al.,* 1990, 1994; *Abercrombie et al.,* 1995].

Foreshocks are the most obvious manifestation of earthquake nucleation and, as such, can provide important constraints on the mechanics of the process. While a great deal is known about the statistics of foreshocks [*Jones and Molnar,* 1979; *Jones,* 1984; *Abercrombie and Mori,* 1995], foreshock mechanics have not generally been closely analyzed. One reason for this is that uncertainties in foreshock locations are often large relative to the dimensions of the sequence. Most earthquakes occur in sparsely instrumented areas where the detection and precise location of foreshocks may be problematic; however, even in well-instrumented areas, typical location uncertainties are on the order of the dimensions of a foreshock sequence, and one cannot easily draw conclusions about the interactions among the foreshocks.

Recently, *Dodge et al.* [1995] relocated the foreshocks of the 1992 Landers $M_W =$ 7.3 earthquake using waveform cross correlation to determine accurate P wave and S wave relative arrival times. The resulting locations had relative uncertainties of less than 100 m horizontally and 200 m vertically. With this level of resolution one can begin to test competing models for earthquake nucleation and foreshock generation. Specifically, one can distinguish between models in which foreshocks are a byproduct of an aseismic nucleation process and models in which the foreshock stress changes contribute to a cascading failure culminating in the mainshock. This distinction is made on the basis of the stress changes caused by the foreshocks. If the foreshocks are part of such a cascading failure process, then they should push the mainshock toward failure, i.e. act to increase the

shear traction, reduce the normal stress, or increase the pore pressure on the mainshock fault plane. Alternatively, if the foreshocks are triggered by an aseismic process or if something other than stress changes causes triggering, there need be no causative relation between the foreshock stress changes and the mainshock occurrence.

Dodge et al. [1995] estimated the stress change at the Landers mainshock hypocenter, due to the foreshocks and found that the foreshocks acted to de-stress the mainshock. However, our original point estimate of the stress change did not include the uncertainties in the hypocentral parameters. In this study, we extend our analysis to produce Stress-change distribution functions, consider the possible role that pore fluid effects can play in the failure process, and analyze five other California foreshock sequences to see whether the Landers results generalize to other earthquakes.

3.2 Relocation Procedure

The first step in studying the mechanics of foreshocks is to obtain accurate locations. This process requires improving the velocity model, minimizing errors in arrival picks, and obtaining a sufficient number and azimuthal distribution of observations to make the hypocentral estimation problem well constrained. Since only relative locations are required in our case, the problems with the velocity model can be minimized by using the arrival times to simultaneously estimate hypocenters, velocity model corrections, and station corrections. The foreshocks occupy small volumes so the ray paths are similar, and almost all the unmodeled velocity structure can be absorbed in the station corrections. We use the VELEST earthquake location program [*Ellsworth*, 1977; *Roecker*, 1981] to estimate velocity model and station corrections.

We use waveform cross correlation to minimize pick errors and to obtain additional *P* and *S* wave arrival picks. Both time domain and frequency domain cross correlation techniques have been used to produce high-precision relative earthquake locations by *Poupinet et al.* [1984], *Frémont and Malone* [1987], *Deichmann and Garcia-Fernandez* [1992], and *Dodge et al.* [1993]. Although the foreshock sequences we analyze are compact, there is typically enough waveform diversity within a sequence that no single event can be found that correlates well with all (or even most of) the other foreshocks. Our first solution to this problem [*Dodge et al.,* 1995] was to use a technique developed by *VanDecar and Crosson* [1990] for determining relative arrival times of teleseisms recorded by a regional seismic network. This technique uses the cross correlations between all pairs

of signals with a weighted least squares adjustment of the corresponding shifts to determine an optimum set of arrival time corrections and estimates of the errors in the resulting adjusted picks.

Although we had considerable success with the least squares approach, it has limitations. Often, the seismograms from a given sequence form distinct groups, highly similar within each group, but very different from group to group. If we attempt to adjust all seismograms simultaneously, we encounter problems with cycle skipping. Also, the seismograms of the larger earthquakes in each sequence are often strongly clipped, and their arrivals must be picked by hand. The results must be carefully inspected for consistency, or the larger event locations may be systematically skewed relative to the smaller events. Our current repicking algorithm first identifies groups of similar seismograms within a sequence and then allows interactive picking of the first arrival for the single seismogram with the highest *snr* in each group. These picks are then fixed, and the remaining group members adjusted by least squares.

One of the major advantages claimed for cross-correlation-derived picks has been that one can achieve subsample precision [*Poupinet et al.,* 1984; *Frémont and Malone,* 1987]. For instance, if the seismograms are digitized at 100 samples per second, the cross-correlation times may have a relative precision of the order of 1-2 ms. In the absence of other sources of error this precision implies relative source location errors of a few tens of meters at most. By introducing hand picks, it might appear that we throw away all the gains in accuracy obtained with cross correlation; however, in our experience, cross correlation reduces errors on two levels. The first and most dramatic improvement in accuracy is from the reduction or elimination of pick errors in excess of one sample. By analogy with the example just cited, this level of timing precision can limit source location errors to about 100 m. At this level, cross correlation is essentially a tool to correct pick errors. Impulsive arrivals with high *snr* are generally picked quite precisely by network analysts. However, as the *snr* decreases, the arrivals become increasingly indistinct until, at some point, the trace is not used. Within that region of decreasing usability, pick errors in excess of one sample are common, and our technique removes this error. Within groups we are able to achieve subsample timing precision. However, since groups of seismograms are tied together by hand picks, the relative positions of the groups are not as well determined as the relative position of seismograms within a group.
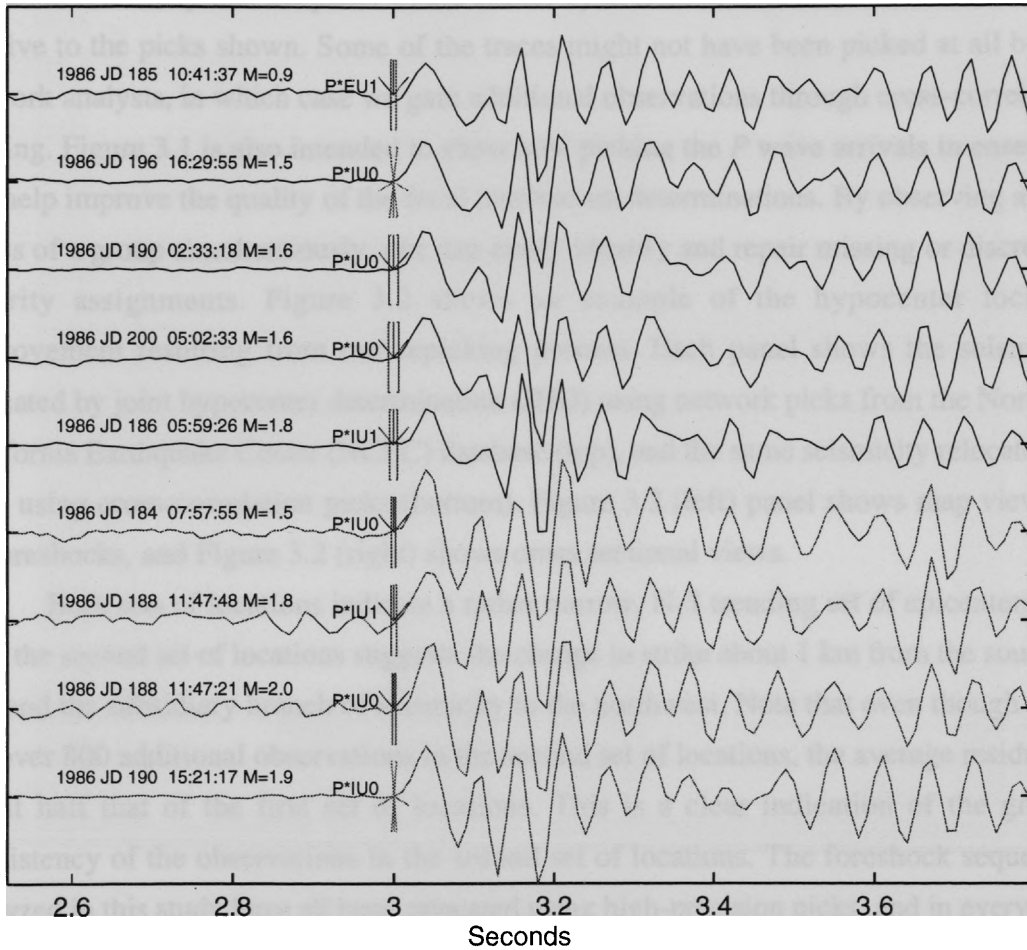
Figure 3.1. Waveforms from some Chalfant foreshocks recorded at station WVD aligned by cross correlation with resulting *P* wave picks. Bottom trace has highest *snr* ratio, and its onset is unambiguous. Remaining onsets have varying amounts of ambiguity that would likely cause picks made in isolation to scatter by several samples relative to the cross-correlation picks.

Figure 3.1 illustrates the results of this process. These are two groups of seismograms ranging in magnitude from 0.9 to 2.0. For each group, the trace marked with an upward pointing arrow has a clear arrival and the other picks are chosen relative to that arrival. In ensemble, all the picks make sense. However, if these traces were picked in isolation, it is likely that the picks would scatter by at least several hundredths of a second relative to the picks shown. Some of the traces might not have been picked at all by the network analysts, in which case we gain additional observations through cross-correlation picking. Figure 3.1 is also intended to show how picking the *P* wave arrivals in ensemble can help improve the quality of the focal mechanism determinations. By observing all the traces of a group simultaneously, one can easily identify and repair missing or discrepant polarity assignments. Figure 3.2 shows an example of the hypocenter location improvement resulting from our repicking process. Each panel shows the seismicity relocated by joint hypocenter determination (JHD) using network picks from the Northern California Earthquake Center (NCEC) database (top), and the same seismicity relocated by JHD using cross-correlation picks (bottom). Figure 3.2 (left) panel shows map views of the preshocks, and Figure 3.2 (right) shows cross sectional views.

Both sets of locations indicate a rather narrow, N-S trending set of epicenters, but only the second set of locations suggests the change in strike about 1 km from the southern end and the subsidiary branch of seismicity to the northwest. Note that even though there are over 800 additional observations in the second set of locations, the average residual is about half that of the first set of locations. This is a clear indication of the greater consistency of the observations in the second set of locations. The foreshock sequences analyzed in this study have all been relocated using high-precision picks, and in every case the resulting locations have significantly lower average residuals and smaller standard errors than locations made using uncorrected picks.

JHD using network picks
1383 P wave picks   44 S wave picks   RMS = .026 $2\sigma_h$= 190 m $2\sigma_v$ = 272 m

JHD using refined picks
2060 P wave picks   216 S wave picks   RMS = .014 $2\sigma_h$ = 79 m $2\sigma_v$ = 152 m
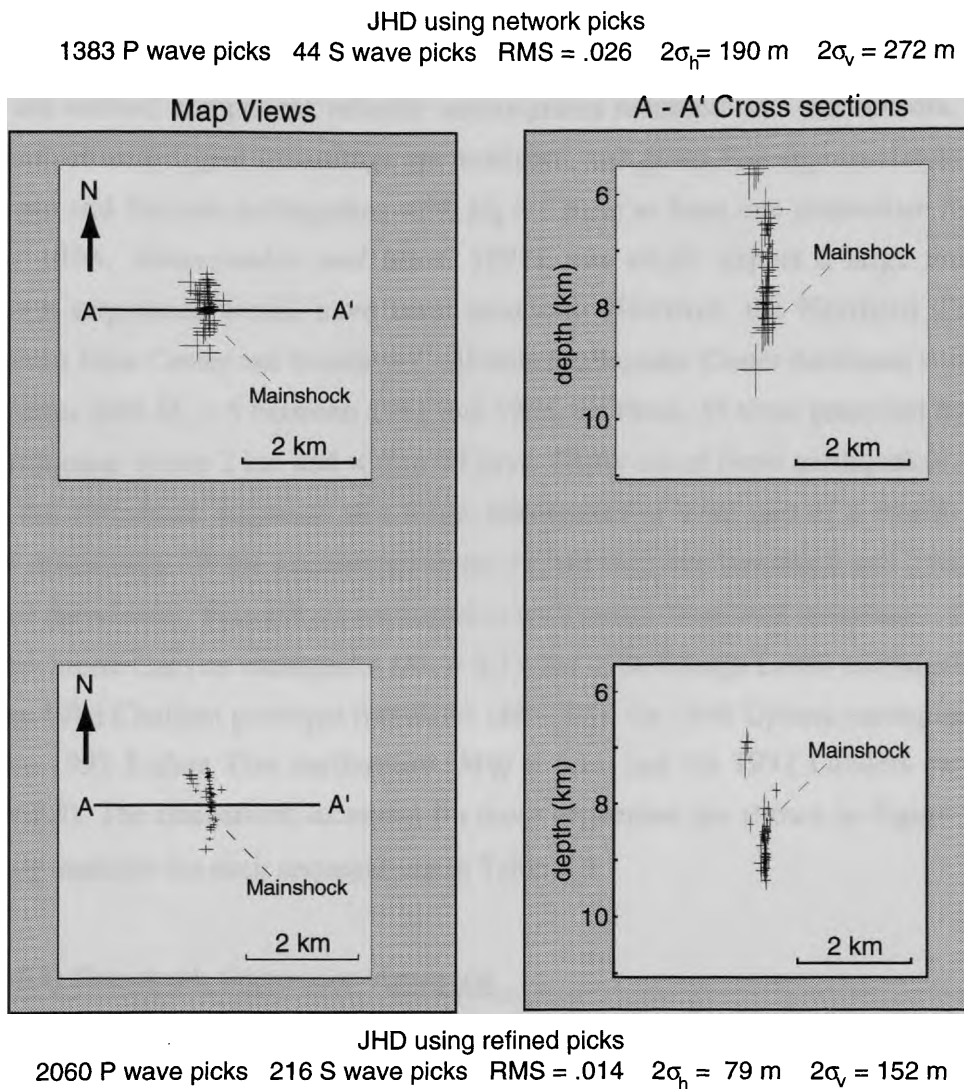
Figure 3.2. Comparison of relocations using network picks and cross-correlation-derived picks with (left) a map view and (right) a cross section looking to the north. (top) Fifty preshocks to the Mount Lewis earthquake relocated by joint hypocenter determination (JHD) using network picks. (bottom) The same events relocated by JHD but using the cross-correlation-derived picks. Note that although there are 677 more observations in the second set of relocations, the average residual decreased from 0.026 to 0.014 s. The average 2σ uncertainties have decreased from 190 to 79 m (horizontal) and from 272 to 152 m (vertical).

3.3 Foreshock Sequences

Our data in this study are seismograms recorded by the northern California, southern California, and University of Nevada, Reno, short-period seismic networks. These are vertical-component velocity seismograms recorded on 1-Hz sensors. Tens of thousands of such digital recordings are available, and given that approximately 44% of California and Nevada earthquakes with $M_L > 5$ have at least one immediate foreshock [*Jones*, 1984; *Abercrombie and Mori*, 1995], one might expect a large number of foreshock sequences would have been recorded. However, the Northern California Earthquake Data Center and Southern California Earthquake Center databases contain 108 earthquakes with $M_L > 5$ between 1981 and 1996. Of these, 55 were preceded by at least one earthquake within 2 km and within 30 days. Thirty-six of those earthquakes occurred within the aftershock sequence of a larger earthquake or were part of a swarm with no distinct mainshock. Of the remaining events, 11 had only one foreshock and 2 had poorly recorded foreshocks. This left six earthquakes with usable foreshock sequences. These are the 1986 Stone Canyon earthquake ($M_L = 4.7$), the 1986 Mount Lewis earthquake ($M_L = 5.7$), the 1986 Chalfant principal foreshock ($M = 5.8$), the 1990 Upland earthquake ($M_L = 5.2$), the 1992 Joshua Tree earthquake ($M_W = 6.1$), and the 1992 Landers earthquake ($M_W = 7.3$). The mainshock locations for these sequences are shown in Figure 3.3, and summary statistics for each sequence are in Table 3.1.

Table 3.1. Foreshock Sequences Analyzed

	Mt. Lewis	Stone Canyon	Chalfant*	Upland	Joshua Tree	Landers
Magnitude	5.7	4.7	5.8	5.2	6.1	7.3
Date	March 31, 1981	May 31, 1986	July 20, 1986	Feb. 20, 1990	April 23, 1992	June 28, 1992
Time, UT	1155:40	0847:56	1429:45	2343:36	0450:23	1157:34
Latitude, °N	37.48	36.64	37.57	34.13	33.96	34.20
Longitude, °W	121.68	121.25	118.44	117.70	116.32	116.44
Depth	8.9	5.9	6.7	4.7	10.0	4.5
Number recorded	18	4	40	7	5	30
Number relocated	15	4	30	6	5	24
Duration hours	260.2	0.9	414.8	501.9	2.4	6.6
†Average distance, km	11.5	5.8	13.0	17.6	18.5	27.0

* This is the principal foreshock to the $M_L = 6.4$ mainshock.
† Values show the average distance from the mainshock of the five nearest stations for each sequence.

1986 Mt. Lewis and Stone Canyon foreshocks

1986 Chalfant foreshocks

1990 Upland foreshocks

1992 Joshua Tree and Landers foreshocks
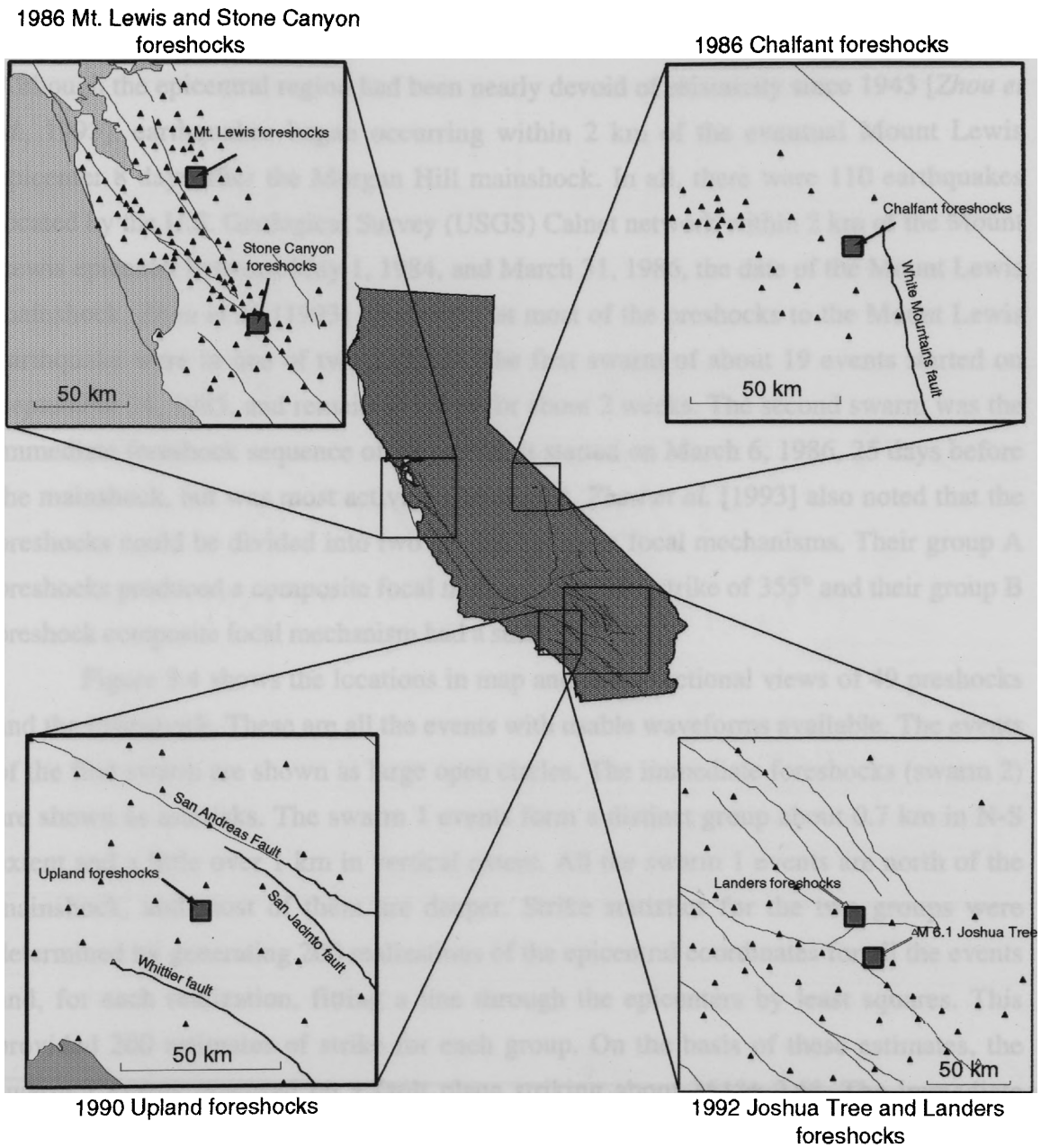
Figure 3.3. Base map showing the locations of the earthquake sequences examined in this study. Triangles show the locations of seismograph stations used in the relocations.

3.3.1 Mount Lewis Sequence

The 1986 Mount Lewis earthquake (M_L = 5.7) occurred on a near-north striking fault about 18 km north of the 1984 Morgan Hill earthquake (M_L = 6.2) epicenter. Although the epicentral region had been nearly devoid of seismicity since 1943 [*Zhou et al.*, 1993], earthquakes began occurring within 2 km of the eventual Mount Lewis epicenter 8 days after the Morgan Hill mainshock. In all, there were 110 earthquakes located by the U.S. Geological Survey (USGS) Calnet network within 2 km of the Mount Lewis epicenter between May 1, 1984, and March 31, 1986, the date of the Mount Lewis mainshock. *Zhou et al.* [1993] observed that most of the preshocks to the Mount Lewis earthquake were in one of two swarms. The first swarm of about 19 events started on September 24, 1985, and remained active for about 2 weeks. The second swarm was the immediate foreshock sequence of 18 events. It started on March 6, 1986, 25 days before the mainshock, but was most active on March 24. *Zhou et al.* [1993] also noted that the preshocks could be divided into two groups based on focal mechanisms. Their group A preshocks produced a composite focal mechanism with a strike of 355° and their group B preshock composite focal mechanism had a strike of 5°.

Figure 3.4 shows the locations in map and cross-sectional views of 49 preshocks and the mainshock. These are all the events with usable waveforms available. The events of the first swarm are shown as large open circles. The immediate foreshocks (swarm 2) are shown as asterisks. The swarm 1 events form a distinct group about 0.7 km in N-S extent and a little over 1 km in vertical extent. All the swarm 1 events are north of the mainshock, and most of them are deeper. Strike statistics for the two groups were determined by generating 200 realizations of the epicentral coordinates for all the events and, for each realization, fitting a line through the epicenters by least squares. This provided 200 estimates of strike for each group. On the basis of these estimates, the swarm 1 events occurred on a fault plane striking about 351°± 2.6°. The immediate foreshocks form a distinctly different group. They are centered below the mainshock hypocenter, and most of them are deeper than the swarm 1 events. There is little overlap between the two groups, but they may abut. The immediate foreshocks extend about 1.1 km along strike and range in depth from about 8.5 to 9.2 km. From the point of contact with the swarm 1 events to the south, the immediate foreshock epicenters lie on a line striking 1°± 2.1°. From the point of contact north they take on the strike of the swarm 1 preshocks. Evidently, these two swarms are adjacent to a change in strike on the fault. The

Map View

A - A' Cross section

	Events prior to 85/09/24
○	Swarm1, 85/09/24 - 85/10/09
+	Events from 85/10/10 - 86/03/19
✳	Foreshocks 86/03/10 - 86/03/31
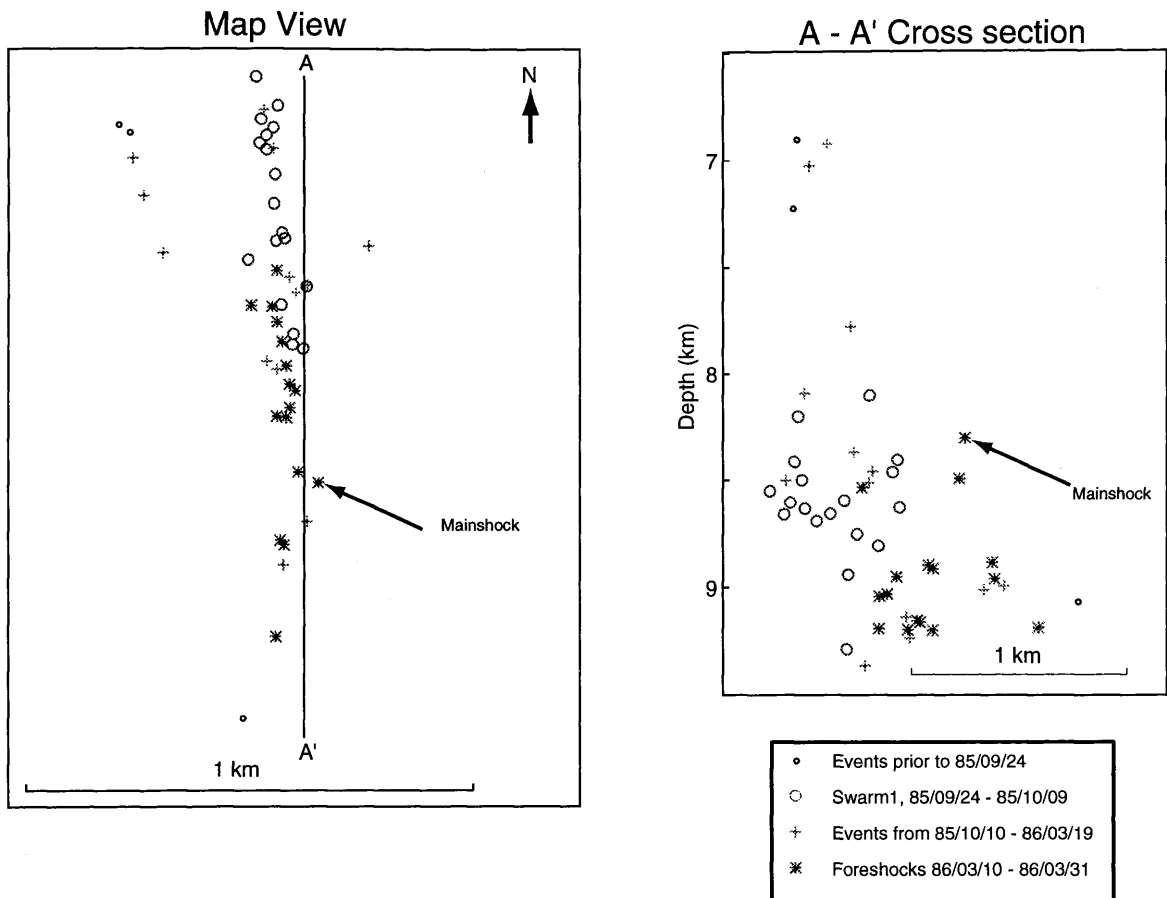
Figure 3.4. Relocated seismicity in the Mount Lewis epicentral region from July 1984 to March 31, 1986, (left) map view and (right) cross section. Events shown as circles are from the swarm that occurred in late 1985. These earthquakes are all north of the mainshock hypocenter and centered at a depth of about 8.5 km. The strike of the seismicity is about 352°. The immediate foreshocks are shown as asterisks and are mostly south of the events of the first swarm. Their average depth is about 0.5 km deeper than the earlier events. Except in the region of overlap with the earlier events, the strike of their epicenters is about 3°. The mainshock epicenter is located within 250 m of the change in strike of the two sequences. The four events at about 7 km depth west of the first swarm apparently occurred on a nearby fault striking more to the west.
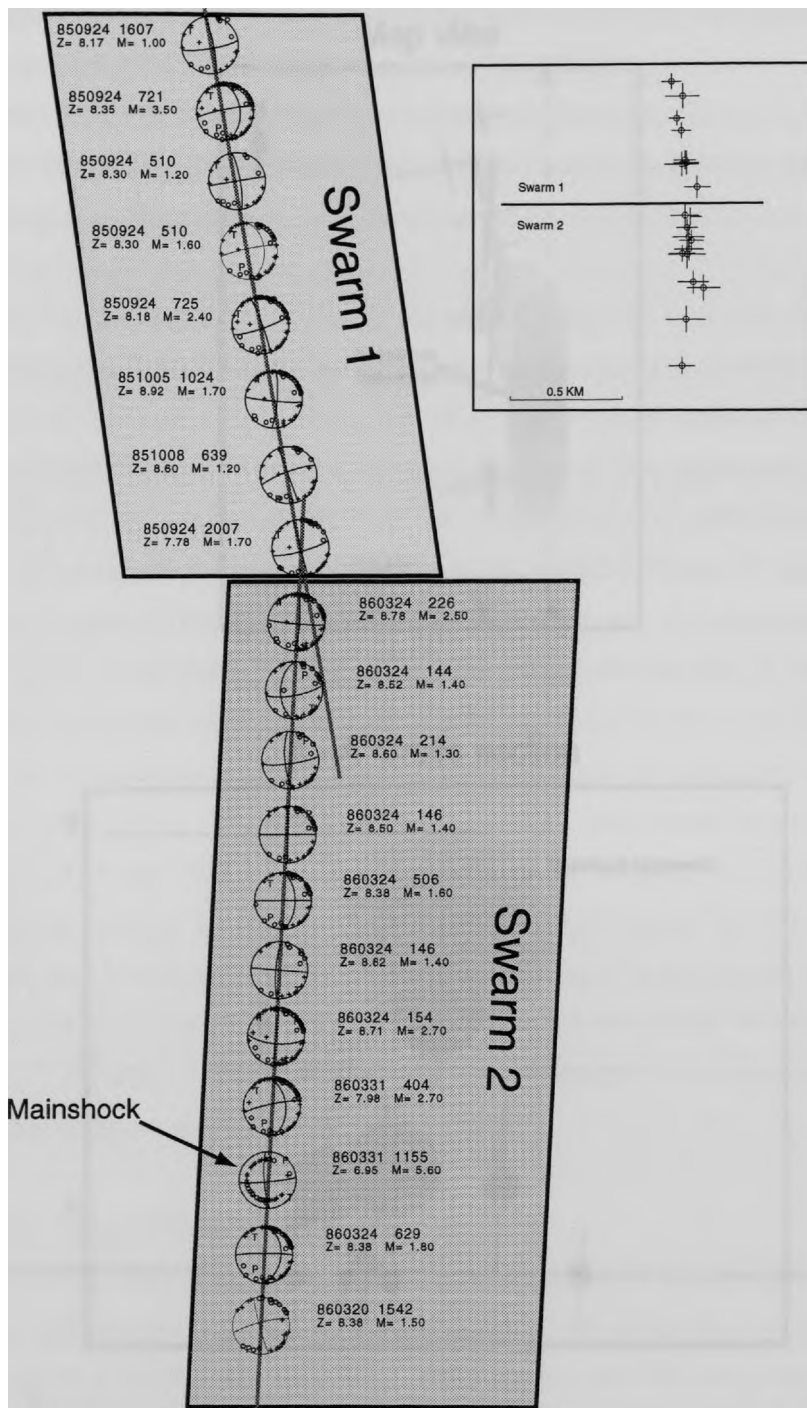
Figure 3.5. Well-constrained focal mechanisms with first motion polarities for the swarm 1 and swarm 2 events of the Mount Lewis sequence. Lower hemisphere plots are shown superimposed on lines with the strike of the seismicity for each group. Events are shown in order of spatial occurrence. Inset shows the actual location of the swarm events with location uncertainties.
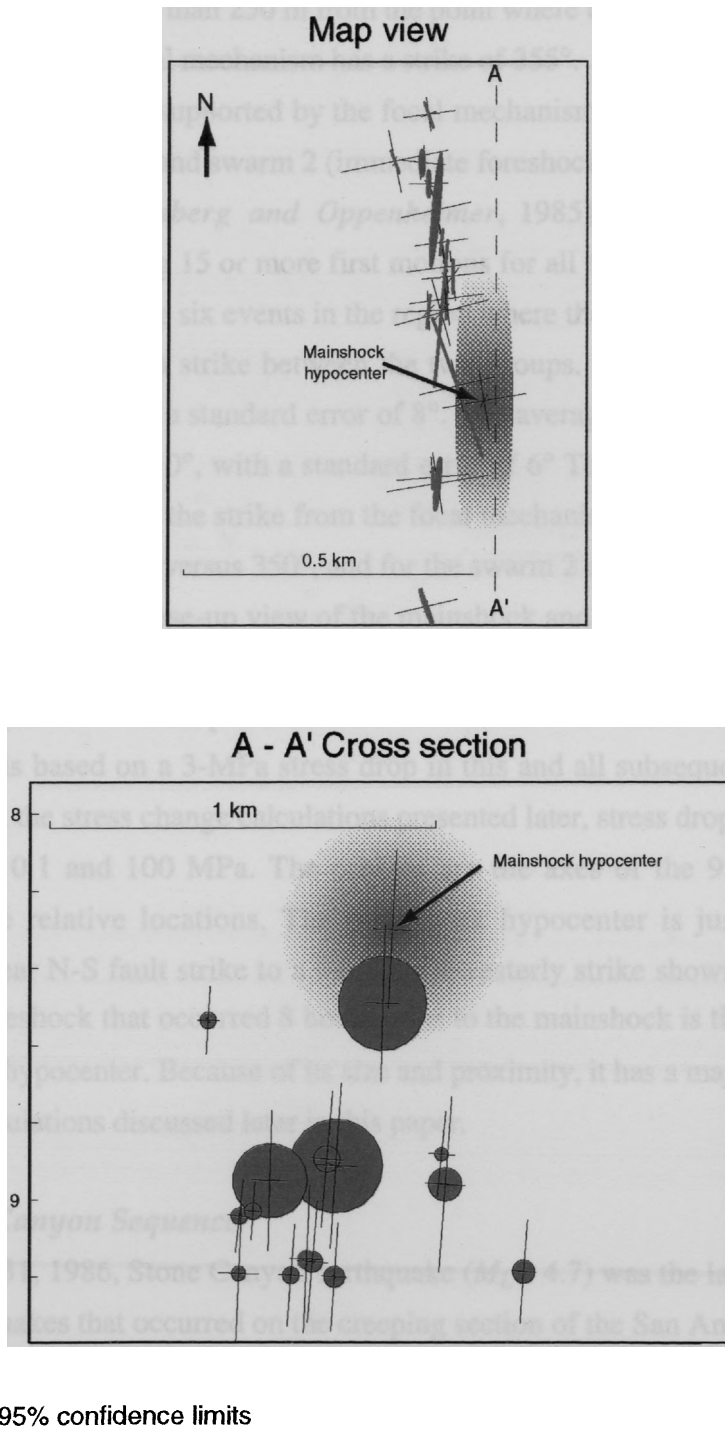
Figure 3.6. Relocated immediate foreshock and mainshock hypocenters for the Mount Lewis sequence. (top) map view and (bottom) cross section. Events are shown as disks with orientation determined from the focal mechanism solution. The size of the disks is estimated assuming a 3.0-MPa stress drop. (Mainshock disk is truncated so that details of sequence are preserved.) Crosses show the axes of the 95% confidence ellipsoids for the relative locations.

mainshock hypocenter is less than 250 m from the point where the fault appears to change strike, and the mainshock focal mechanism has a strike of 355°.

This interpretation is supported by the focal mechanisms. Figure 3.5 shows focal mechanisms for the swarm 1 and swarm 2 (immediate foreshocks) events computed using the FPFIT program [*Reasenberg and Oppenheimer*, 1985]. These are all the focal mechanisms determined using 15 or more first motions for all the relocated swarm 1 and swarm 2 events, but excluding six events in the region where the two swarms overlap and the focal mechanisms vary in strike between the two groups. The average strike of the swarm 1 events is 350°, with a standard error of 8°. The average strike of the immediate foreshocks and mainshock is 0°, with a standard error of 6° The agreement between the strike from the seismicity and the strike from the focal mechanism determinations is good (for the swarm 1 events 351°, versus 350°, and for the swarm 2 events, 1° versus 0°).

Figure 3.6 shows a close-up view of the mainshock and 15 immediate foreshocks that we were able to relocate. In this figure the events are shown as disks oriented according to the preferred nodal plane of the focal mechanisms and view direction. The size of the disks is based on a 3-MPa stress drop in this and all subsequent plots of this type. However, in the stress change calculations presented later, stress drops were allowed to vary between 0.1 and 100 MPa. The crosses are the axes of the 95% confidence ellipsoids for the relative locations. The mainshock hypocenter is just south of the transition from near N-S fault strike to a more northwesterly strike shown in Figure 3.5. The M_L = 2.7 foreshock that occurred 8 hours prior to the mainshock is the event closest to the mainshock hypocenter. Because of its size and proximity, it has a major effect on the stress change calculations discussed later in this paper.

3.3.2 Stone Canyon Sequence

The May 31, 1986, Stone Canyon earthquake (M_L = 4.7) was the last of a series of six M_L = 4 earthquakes that occurred on the creeping section of the San Andreas fault near Hollister between August 1982 and June 1986 [*Wyss and Habermann*, 1988]. The ruptures of the six earthquakes, defined by aftershock zones, abut each other to form an approximately 20-km long by 5-km deep patch that slipped during this period of activity. The May 1986 Stone Canyon earthquake occurred in a seismic gap between the first and third events of the series and was preceded by four immediate foreshocks within an hour of the mainshock.
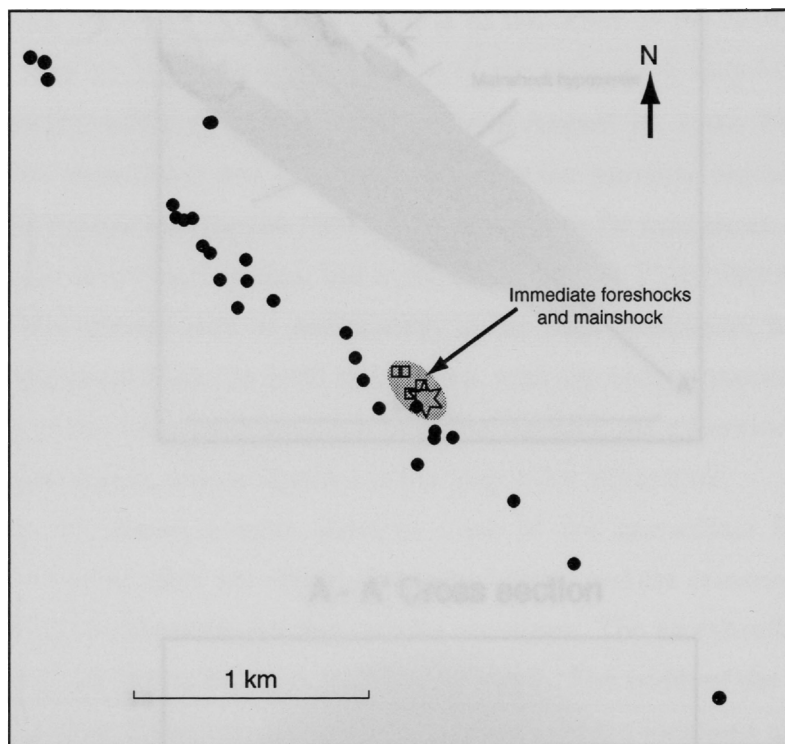
Figure 3.7. Relocated seismicity in the Stone Canyon epicentral region from July 1984 to May 31, 1986. Stippled region encloses the immediate foreshock and mainshock epicenters. There is no obvious change in strike of the seismicity that might indicate a change in fault strike. The mainshock and immediate foreshocks appear to be shifted somewhat to the NE, but the amount of the shift is of the order of the location uncertainties and could be an artifact.
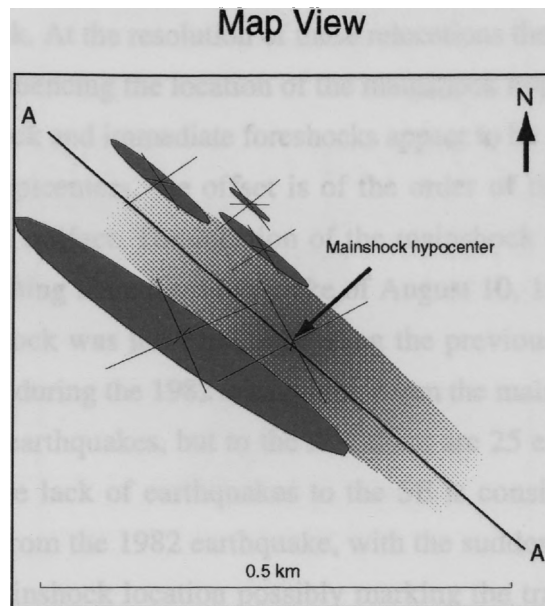
Map View

Figure 3.8. Relocated immediate foreshock and mainshock hypocenters of the Stone Canyon earthquake, (top) map view and (bottom) cross section looking to the NE.

Figure 3.7 shows a map view of relocated seismicity for the time period July 1984 to the time of the mainshock in May 1986 within a region 4 km long by 4 km deep and centered on the mainshock. At the resolution of these relocations there is little evidence for structural irregularity influencing the location of the mainshock hypocenter. Although the epicenters of the mainshock and immediate foreshocks appear to be displaced somewhat to the NE from the other epicenters, the offset is of the order of the uncertainties in the locations and may be an artifact. The location of the mainshock may be influenced by stress heterogeneity resulting from the earthquake of August 10, 1982. The region to the NW of the 1986 mainshock was not ruptured during the previous earthquakes, but the region to the SE ruptured during the 1982 earthquake. From the mainshock epicenter to the SE there are only seven earthquakes, but to the NW there are 25 earthquakes during this time period. This relative lack of earthquakes to the SE is consistent with that region having been destressed from the 1982 earthquake, with the sudden transition to a higher seismicity rate at the mainshock location possibly marking the transition to the higher-stress, unruptured region, which ruptured in the May 1986 mainshock.

Figure 3.8 shows a more detailed view of the immediate foreshocks and mainshock. The earthquakes are shown as oriented disks, and the crosses are the axes of the 95% confidence ellipsoids for the relative locations. The foreshocks are clustered within a region about 200 m in length by 350 m in depth. The width of the foreshock zone is a little over 100 m. However, since the uncertainties in the locations are a substantial fraction of the width, it is difficult to tell how much of the width is real and how much is due to errors in the foreshock relocation.

3.3.3 Chalfant Sequence

The 1986 Chalfant, California, earthquake ($M_L = 6.4$) occurred on July 21, 1986, in the Bishop-Mammoth Lakes area. The mainshock was preceded by a $M_L = 5.7$ foreshock that occurred about 24 hours earlier and 3 km to the north on an apparent conjugate fault plane [*Smith and Priestley,* 1988]. That principal foreshock was itself preceded by 40 foreshocks within 17 days recorded by the USGS Calnet and University of Nevada, Reno, short-period networks. Of these, 30 had usable waveforms and were analyzed in this study. Most of the Mammoth Lakes stations to the NW of the Chalfant valley are telemetered to Menlo Park. A group of stations immediately to the west and SW

Cross section, (Viewing azimuth 30 degrees)

Cross section, (Viewing azimuth 120 degrees)

$\perp$ 95% confidence limits

◯ More than 3 days before mainshock

⬤ Within 3 days of mainshock
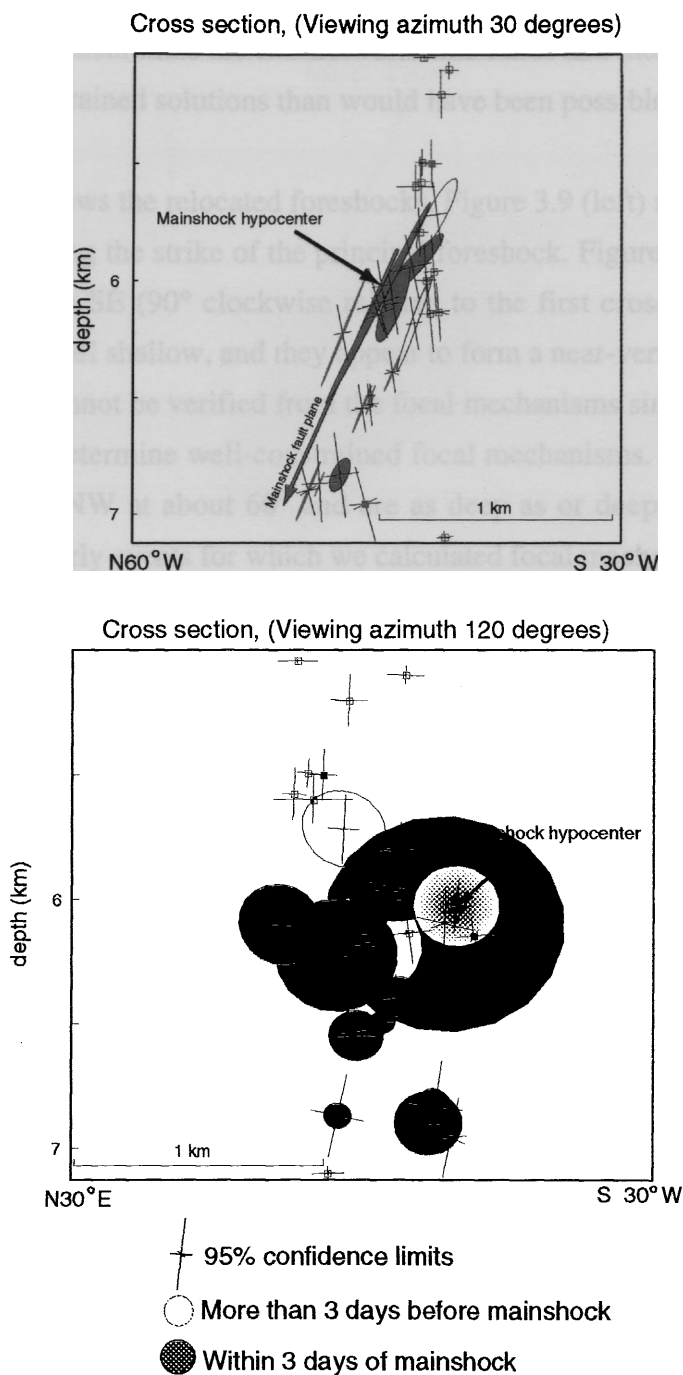
Figure 3.9. Relocated immediate foreshock and mainshock hypocenters of the Chalfant earthquake in cross sections (top) looking along strike to the NE and (bottom) perpendicular to the strike looking to the SE. Foreshocks occurring prior to 3 days before the mainshock are shown with open circles. Earthquakes without focal mechanisms are shown as squares.

is telemetered both to Menlo Park and to Reno. The remaining east and NE stations are telemetered only to Reno. Because there were five shared stations, we were able to use cross correlation to synchronize the two network time bases and merge the data sets, thus providing better constrained solutions than would have been possible using either data set individually.

Figure 3.9 shows the relocated foreshocks. Figure 3.9 (left) shows a cross section looking to the NE along the strike of the principal foreshock. Figure 3.9 (right) is a cross section looking to the SE (90° clockwise relative to the first cross section). The early foreshocks are nearly all shallow, and they appear to form a near-vertical plane. However, this fault geometry cannot be verified from the focal mechanisms since these events were mostly too small to determine well-constrained focal mechanisms. The later foreshocks nearly all dip to the NW at about 60° and are as deep as or deeper than the principal foreshock. The two early events for which we calculated focal mechanisms dip to the NW at about 60°, much the same as the later foreshocks. The later foreshocks appear to define two subparallel fault strands. The principal foreshock is offset about 400 m to the SW from most of the other foreshocks. However, the largest of the foreshocks to the principal foreshock, a M_L = 3.9 event, is nearly collocated with the principal foreshock hypocenter. This foreshock sequence appears to be another example of earthquake nucleation at a fault zone irregularity. The principal foreshock hypocenter is at a depth of about 6 km, the depth where the change in dip (based on seismicity) occurs. Nearly all the large foreshocks of the sequence occurred within 250 m of that apparent change in dip.

3.3.4 Upland Sequence

The 1990 Upland, California, earthquake (M_L = 5.2) was a predominantly left-lateral, strike-slip earthquake that occurred on the San Jose fault [*Hauksson and Jones,* 1991]. This was the second of a pair of moderate earthquakes that occurred at nearly the same location within two years of each other. The first was a M_L = 4.6 event that occurred about two km to the southwest and about 4 km deeper, also apparently on the San Jose fault [*Hauksson and Jones,* 1991]. The 1990 earthquake was preceded by three foreshocks on the same day, as well as by four other foreshocks that occurred within 20 days prior to the mainshock. The relocated seismicity is shown in Figure 3.10. The foreshock sequence is distinguished from the other sequences examined in this study in that although the foreshocks were tightly clustered, their hypocenters were well removed
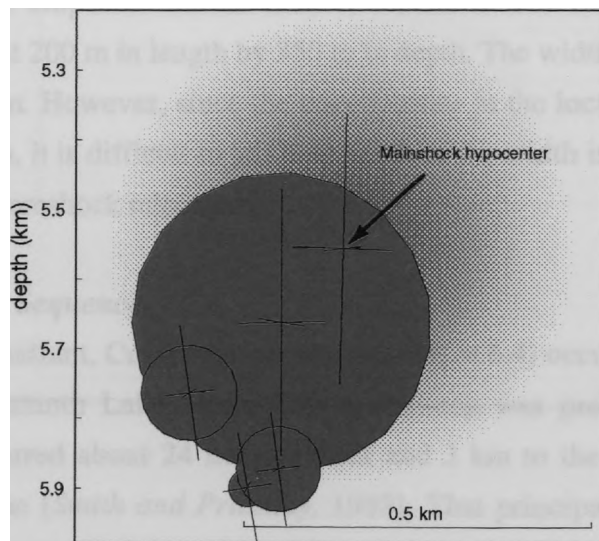
Figure 3.10. Relocated immediate foreshock and mainshock hypocenters of the Upland earthquake, (top) map view and (bottom) cross section perpendicular to the strike looking to the SE. Earthquakes without focal mechanisms are shown as squares.

(> 2 km) from the mainshock hypocenter. It is difficult to infer much about the geometry of the San Jose fault in the hypocentral region from the limited data of the foreshock sequence. However, *Hauksson and Jones* [1991] noted that the dip of the San Jose fault based on aftershocks varies with depth. Above 5-6 km the fault dips about 70° to the NW. Between 6 km and 9-10 km the fault is near vertical, from there to about 12 km the fault dips about 60°, and below 13 km the dip is again about 70°. The foreshocks range in depth from about 6.4 to 7.3 km, and the three for which we have focal mechanisms show near vertical dips, consistent with the geometry obtained by *Hauksson and Jones* [1991]. Most of the aftershocks of the 1988 earthquake occurred at depths greater than 5 km, below the hypocenter of the 1990 earthquake. If the aftershocks outline the part of the fault that slipped coseismically or postseismically, then we might expect that the region above 5 km was closer to failure than the deeper part of the fault. Together, these observations suggest that the location of the foreshocks could have been controlled both by structural complexity of the fault zone (the transition from steeply dipping to vertical to shallow dipping) and by stress concentration from the earlier event.

3.3.5 Joshua Tree Sequence

The 1992 Joshua Tree, California, earthquake ($M_W = 6.1$) was the first large earthquake of the Landers, California, earthquake sequence. It occurred about 10 km east of the San Andreas fault and 20 km south of the Pinto Mountain fault. The hypocenter was at about 10 km depth, and there was no associated surface rupture [*Hauksson et al.*, 1993]. The mainshock was preceded by five foreshocks within 2.4 hours, the first of which had a magnitude of 4.6. Figure 3.11 shows the relocated mainshock and foreshock hypocenters. Prior to the foreshocks there had been almost no earthquakes within 2 km of the epicenter since at least 1982. The $M_L = 4.6$ foreshock hypocenter was about 300 m from the mainshock hypocenter, and the focal mechanisms were both right-lateral on a plane striking 345°. This relative location is based on first-break times since seismograms of both the principal foreshock and the mainshock are clipped at all nearby stations.

3.3.6 Landers Sequence

The 1992 Landers, California, earthquake ($M_W = 7.3$) was the largest earthquake in the sequence that began with the Joshua Tree foreshocks. The Landers earthquake occurred on June 28, approximately 2 months after the Joshua Tree earthquake. The

mainshock initiated with a magnitude 4.4 sized immediate foreshock [*Abercrombie and Mori*, 1994] before propagating ~70 km along strike to the northwest [*Cohee and Beroza*, 1994]. The epicenter was about 30 km north-northwest of the Joshua Tree epicenter. The Landers earthquake was preceded by 27 foreshocks that occurred within 7 hours of the mainshock and within about 1.5 km of the mainshock hypocenter. There were an additional three events that occurred between the date of the Joshua Tree mainshock and June 28 that were located within 2 km of the Landers epicenter.

Figure 3.12 shows the relocated foreshocks. This is similar to *Dodge et al.* [1995, Figure 3.9] but uses locations made using the technique discussed in this paper. Figure 3.12 (left) is a map view, and Figure 3.12 (right) is a cross section looking to the NE perpendicular to the strike of the seismicity. The three foreshocks occurring before the day of the mainshock are shown unshaded. Foreshocks without focal mechanisms are shown as squares. All others are shown as oriented disks. The sequence extends about 1.7 km along the fault and about 1.5 km in depth. The foreshock epicenters define an approximate 500-m jog near the mainshock hypocenter. The existence of the jog is supported by the focal mechanisms, which show a systematic rotation in strike through the jog. Virtually all the moment release of the foreshock sequence is concentrated around the jog. The largest foreshock (M_L = 3.6) is nearly collocated with the mainshock hypocenter.
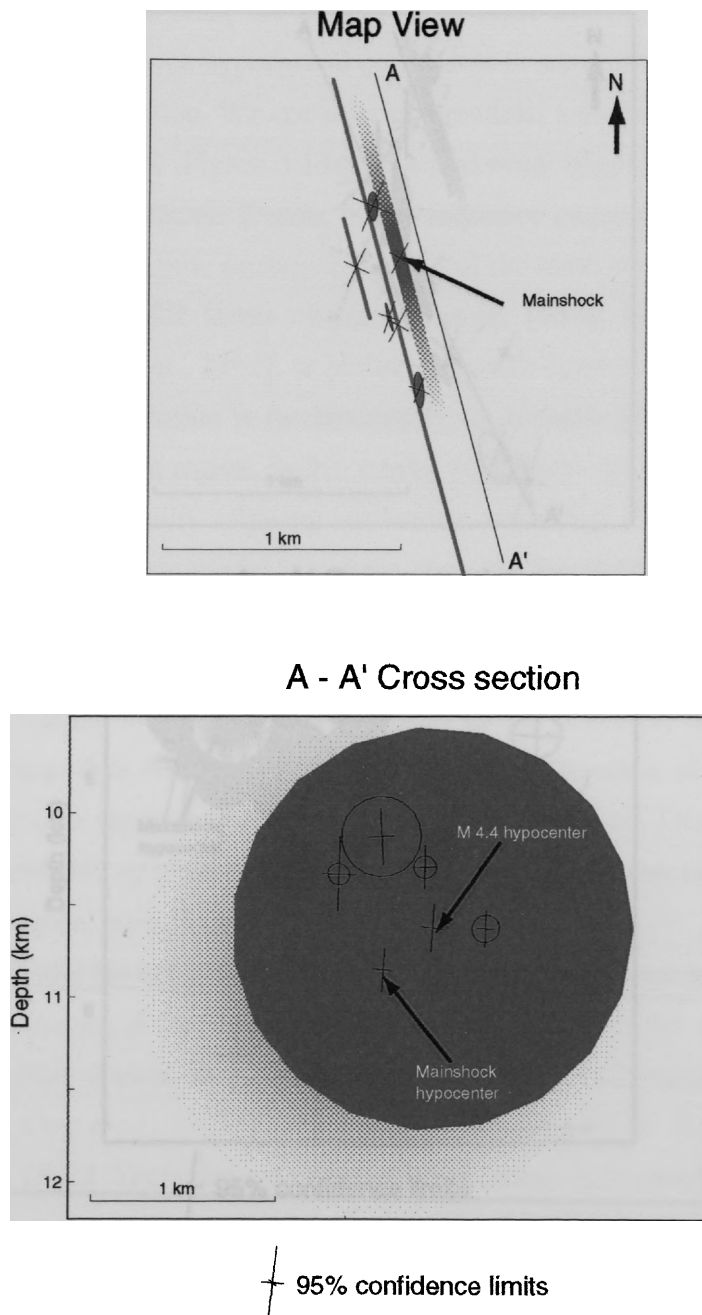
Figure 3.11. Relocated immediate foreshock and mainshock hypocenters of the Joshua Tree earthquake (top) map view and (bottom) cross section parallel to the strike looking to the NE. The largest foreshock has a focal mechanism very similar to that of the mainshock and is nearly collocated with the mainshock hypocenter.
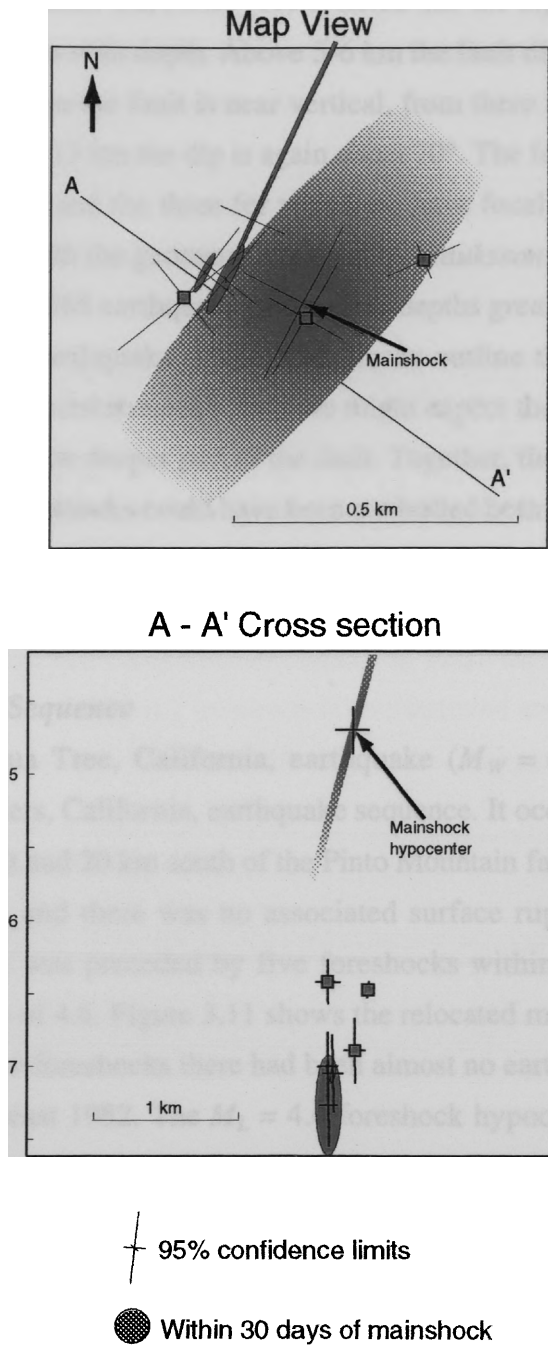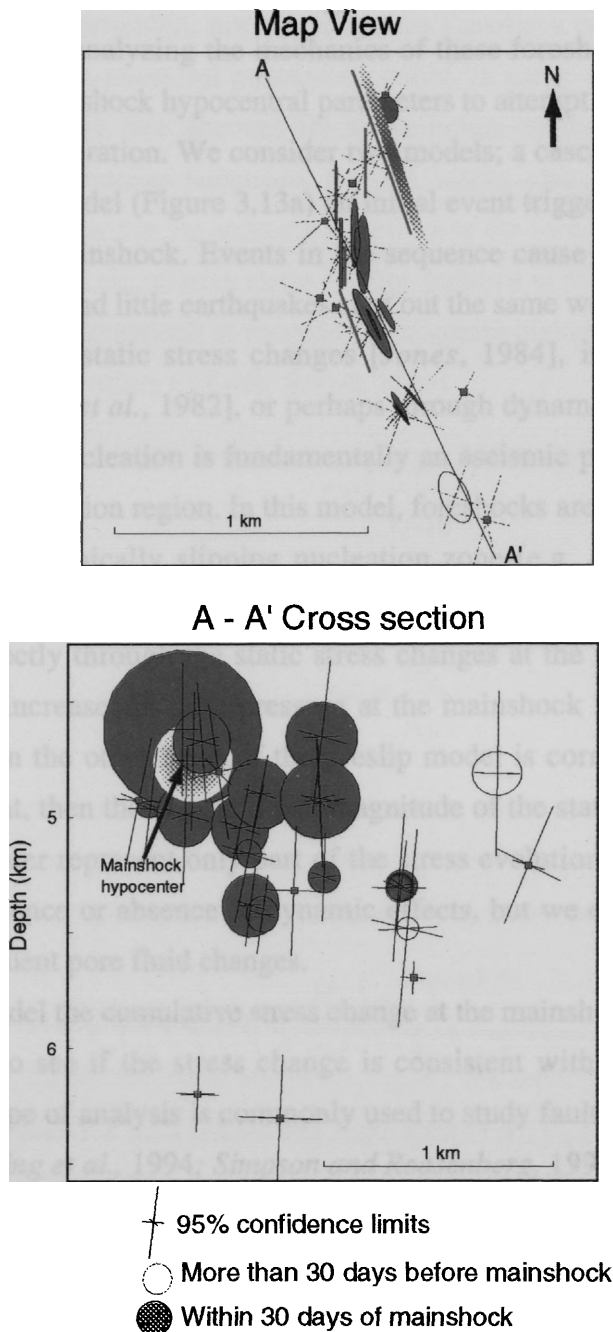
Figure 3.12. Relocated immediate foreshock and mainshock hypocenters of the Landers earthquake, (top) map view, and (bottom) cross section parallel to the strike of the sequence looking to the NE. In map view a pronounced right step is visible in the seismicity. The step is associated with a clockwise rotation of focal mechanisms. The largest foreshock has a focal mechanism very similar to that of the mainshock and is nearly collocated with the mainshock hypocenter.

3.4 Stress Change Calculations

The next step in analyzing the mechanics of these foreshock sequences is to use our knowledge of the foreshock hypocentral parameters to attempt to discriminate between models of foreshock generation. We consider two models; a cascade model and a preslip model. In the cascade model (Figure 3.13a) an initial event triggers a sequence of events that culminate in the mainshock. Events in the sequence cause the occurrence of later events. In this view, big and little earthquakes start out the same way. The triggering might be directly through the static stress changes [*Jones*, 1984], indirectly through pore pressure changes [*Jones et al.*, 1982], or perhaps through dynamic effects. In the preslip model (Figure 3.13b), nucleation is fundamentally an aseismic process involving quasi-static creep over a nucleation region. In this model, foreshocks are interpreted as localized failure within the aseismically slipping nucleation zone [e.g. *Das and Scholz,* 1981; *Ohnaka,* 1992]. If the cascade model is correct, then the foreshocks should act to trigger the mainshock, directly through the static stress changes at the mainshock hypocenter, indirectly through increases in pore pressure at the mainshock hypocenter, or through dynamic effects. On the other hand, if the preslip model is correct or if only dynamic effects are important, then the direction and magnitude of the static stress changes at the mainshock hypocenter represent only part of the stress evolution. Our modeling cannot distinguish the presence or absence of dynamic effects, but we can test for static stress changes and subsequent pore fluid changes.

We will model the cumulative stress change at the mainshock hypocenter from all of the foreshocks to see if the stress change is consistent with the mainshock failure mechanism. This type of analysis is commonly used to study fault interactions on a much larger scale [e.g., *King et al.,* 1994; *Simpson and Reasenberg,* 1994; *Harris and Simpson,* 1992; *Stein et al,* 1992]. There are a number of idealizations and uncertainties associated with this calculation. Potentially geometrically complex faults are modeled as one, or a few rectangular planes. An approximation of the actual slip distribution is made. The earth is modeled as an elastic half-space. Many unknown factors affecting the frictional properties of the target fault are lumped into an assumed coefficient of friction. These approximations affect details of the stress change calculations. However, if the target fault is not in a high-gradient part of the stress field, they have little effect on the magnitude or sign of the stress change.

Our relative locations are accurate (95% confidence limits less than 100 m horizontally and 200 m vertically), but the size of the foreshock zones is only of the order of 1 km. Thus errors in hypocentral parameters could, in some cases, induce significant errors in calculated stress. We account for those errors by mapping the hypocentral uncertainties into distribution functions for the stress changes on the mainshock hypocenters. For each sequence we estimate the effect of the foreshocks on the mainshock initiation by modeling the cumulative stress change induced at the mainshock hypocenter by the foreshocks. Each foreshock is modeled as a square dislocation with area equal to that of a circular patch of radius r [*Keilis-Borok,* 1959]

$$r = \left(\frac{7M_0}{17\Delta\sigma} \right)^{1/3}$$

(4.1)

and displacement

$$\Delta\bar{u} = \frac{M_0}{A\mu} .$$

(4.2)

Here $\Delta\bar{u}$ is the displacement, M_0 is the seismic moment, $\Delta\sigma$ is the static stress drop, A is the area that slipped, and μ is the shear modulus. We estimate M_0 from the earthquake magnitude M using the empirical relation [*Kanamori and Anderson,* 1975]

$$M_0 = 10^{(1.5M+9.05)} .$$

(4.3)

The locations of the foreshock hypocenters (x_s, y_s, z_s) are from our relocations, and the orientations of the foreshock fault planes and slip vectors ($\phi_s, \delta_s, \lambda_s$) are determined using the FPFIT program [*Reasenberg and Oppenheimer,* 1985]. Only foreshocks of at least magnitude 2.0 are used since smaller events have little effect on the stress field and since the smaller events usually do not have well-constrained focal mechanisms. These data, ($x_s, y_s, z_s, A, \Delta u, \phi_s, \delta_s, \lambda_s$) are used to calculate the stress-change tensor at the mainshock hypocenter (x_m, y_m, z_m) using a method developed by *Okada* [1992]. From that we obtain the shear stress change in the direction of the mainshock slip vector $\Delta\tau_s$, the normal stress change at the mainshock hypocenter $\Delta\sigma_N$, and the mean stress change at the mainshock hypocenter $\Delta\sigma_m$, where

$$\Delta\sigma_m = \Delta\sigma_{kk} / 3 .$$

(4.4)

The Coulomb stress change $\Delta\sigma_c$ due to one foreshock at the mainshock hypocenter is

$$\Delta\sigma_c = \Delta\tau_s - \mu_f\left(\Delta\sigma_N - \Delta p\right). \tag{4.5}$$

Here μ_f is the coefficient of friction for dry rock and $\Delta p = -B\Delta\sigma_m$ is the pore pressure change at the mainshock hypocenter assuming undrained conditions. B is Skempton's coefficient, an elastic constant introduced by Biot theory that is a combination of modulii for undrained and drained deformation. B ranges from 0.51 for Tennessee marble to 0.88 for Rhur sandstone [*Rice and Cleary*, 1976]. The exact value of B used does not influence our results much since the mean stress changes are relatively small. We used a value of 0.8. The cumulative Coulomb stress change due to a sequence of M foreshocks is

$$\Delta S_c = \sum_{i=1}^{M}\left[\Delta\tau_s^i - \mu_f\left(\Delta\sigma_N^i - \Delta p^i\right)\right]. \tag{4.6}$$

If our data were exact, this point estimate of the stress change would be the true stress change. However, although our relocations and focal mechanism determinations are very accurate, their uncertainties are significant relative to the dimensions of the sequence. If the mainshock hypocenter is in a high-gradient part of the stress field, then small errors in location, mechanism, or event size may cause large changes in the value or even the sign of the calculated Coulomb stress. To properly account for the effect of the uncertainties, we treat our data ($x_s, y_s, z_s, A, \Delta u, \phi_s, \delta_s, \lambda_s, x_m, y_m, z_m, \phi_m, \delta_m, \lambda_m$) as random variables mapped through the stress-change calculations into the random variable ΔS_c, for which we estimate the distribution by Monte Carlo simulation [*Press et al.*, 1986]. We assume that the errors in our data are normally distributed with zero mean. For the hypocenter locations the distribution of each variable is centered on its nominal value and the variance of its distribution is taken from the solution covariance. The variance of each focal mechanism parameter is taken as the squared parameter uncertainty from the FPFIT program. Stress drops are assumed to be distributed lognormally with a mean of 3.0 MPa and with 99% of the values between 0.1 and 100 MPa. From the stress drop distribution and magnitude we obtain distributions of foreshock size A and slip $\Delta\bar{u}$. To account for the focal plane ambiguity in the focal mechanisms, we generate another random variable uniformly distributed between -1 and +1 and choose the focal plane and rake based on the sign of this

(a) Slow Cascade
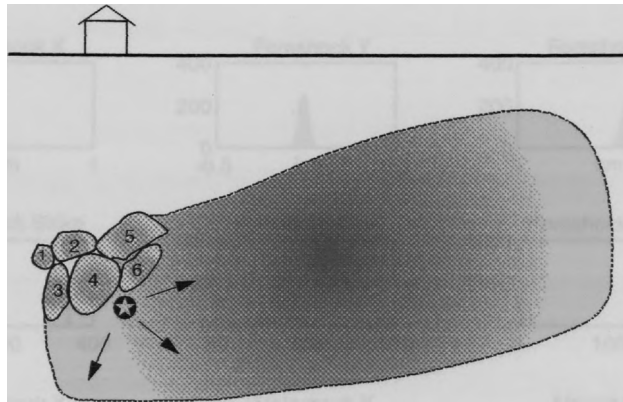
(b)Preslip Triggering
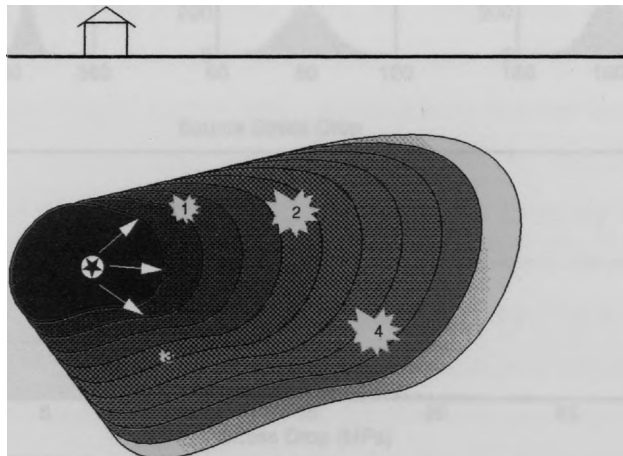
Figure 3.13. Schematic depiction of two possible mechanisms for foreshock generation. (a) Foreshocks triggered by previous foreshocks load the point of the eventual mainshock in a cascade of failure. (b) Foreshocks occurring at asperities within the nucleation region as the asperities are loaded by creep. Here foreshocks are a byproduct of the nucleation process.
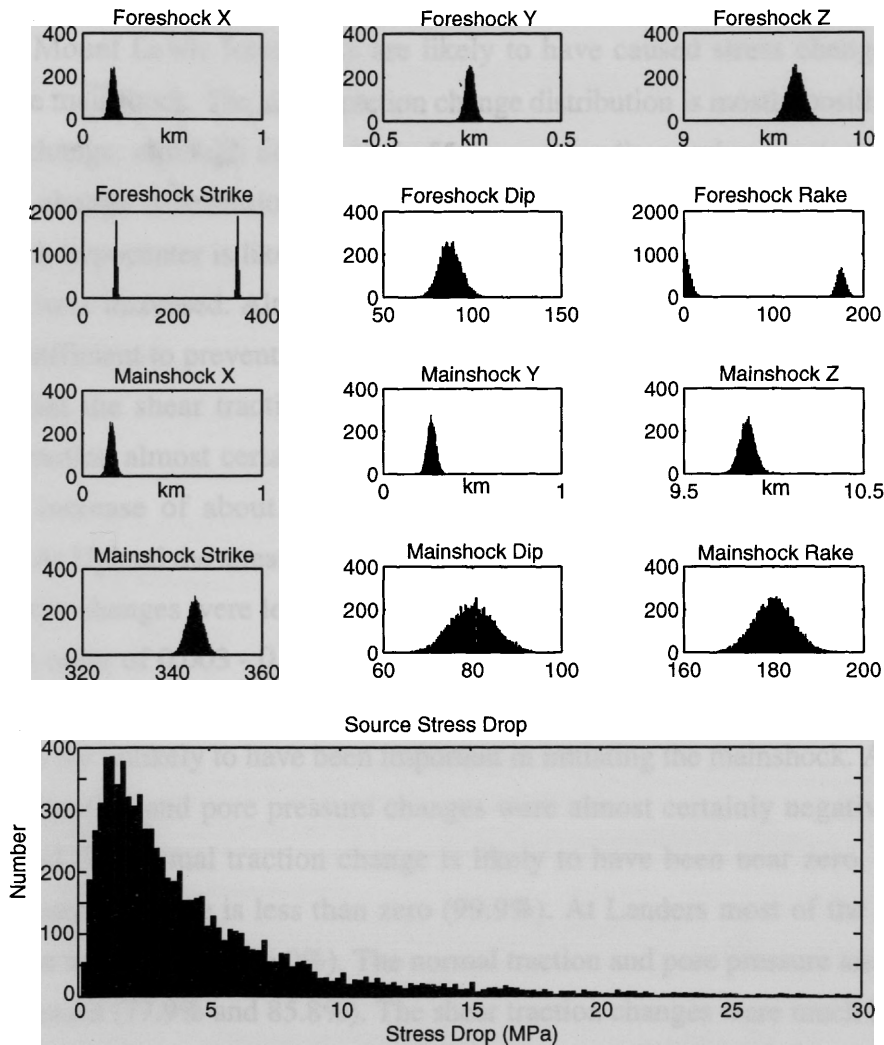
Figure 3.14. Sample of input parameter distributions for stress-change modeling. (top to bottom) Distributions for the source event coordinates, distributions for the source focal mechanism parameters (the bimodal character of the strike and rake distributions is intended to account for the focal-plane ambiguity in the focal mechanism determinations), corresponding distributions for the mainshock hypocenter (the focal mechanism ambiguity is considered to be resolved for the mainshock, so its strike and rake distributions are unimodal), and distribution for source stress drop.

random variable. Figure 3.14 shows an example set of data distributions generated using this approach.

Figure 3.15 shows the simulation results for the six foreshock sequences. For each sequence the shear traction change, normal traction change, Coulomb stress change ($\mu = 0.6$), and the pore pressure change distributions are shown. Of the six sequences, only the Mount Lewis foreshocks are likely to have caused stress changes that would trigger the mainshock. The shear traction change distribution is mostly positive, the normal traction change, although near zero, is 55% negative (increasing tension), and the pore pressure change distribution is positive. At Stone Canyon the shear traction at the mainshock hypocenter is likely (80%) to have decreased and the normal traction is likely (72%) to have increased. Although there may have been a slight pore pressure increase, it was not sufficient to prevent the Coulomb stress distribution from being mostly negative. At Chalfant the shear traction change was almost certainly negative (99.7%) and the normal traction almost certainly increased. Although there appears to have been a pore pressure increase of about 0.2 MPa, the Coulomb stress change was still negative (99.3%). At Upland the stress changes were consistent with triggering, but the magnitudes of the stress changes were less than 0.001 MPa. By comparison, maximum tidal stresses are of the order of 0.003 - 0.004 MPa [*Bodri and Iizuka*, 1989]. Since no clear evidence exists that tidal stresses trigger earthquakes, we conclude that the stress changes from the foreshocks are unlikely to have been important in initiating the mainshock. At Joshua Tree the shear traction and pore pressure changes were almost certainly negative (99.9% and 96.1%) and the normal traction change is likely to have been near zero. The resulting Coulomb stress change is less than zero (99.9%). At Landers most of the shear traction distribution was negative (86.0%). The normal traction and pore pressure are both likely to have decreased (77.9% and 85.8%). The shear traction changes were much larger than the normal traction changes, so the Coulomb stress distribution was mostly negative (84.9%) These Coulomb Stress-change results are consistent with the previous point estimates of *Dodge et al.* [1995] for this earthquake.

All stresses in MPa
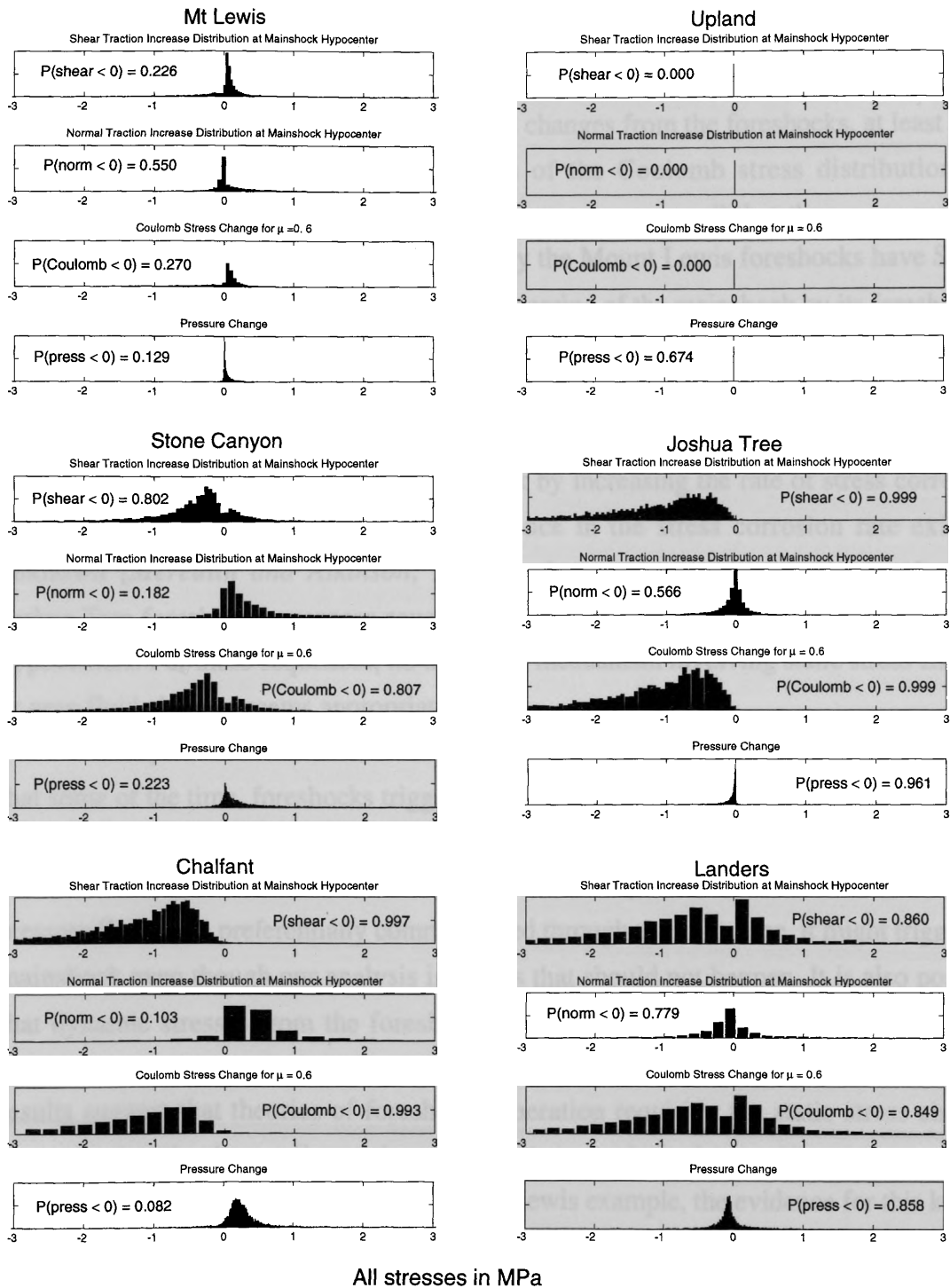
Figure 3.15. Stress-change distributions for the six sequences. (top to bottom) Shear traction distribution, normal traction distribution, the Coulomb Stress distribution, and the pore pressure distributions. Sign conventions are: positive shear, negative normal traction, positive Coulomb stress, and positive pore pressure change contribute to failure. The probability of each parameter being less than zero is also shown.

3.5 Discussion

For four of the six sequences the sign of the Coulomb stress distribution suggests that the mainshock was not triggered by stress changes from the foreshocks, at least at the 80% confidence level. At Upland the sign of the Coulomb stress distribution was consistent with triggering, but the stress changes were so small that they were probably unimportant in triggering the mainshock. Only the Mount Lewis foreshocks have Stress-change distributions clearly consistent with triggering of the mainshock by its foreshocks.

Pore fluids can accelerate the growth of cracks in silicates through stress corrosion [*Scholz*, 1990]. If increases in pore pressure increase the rate of stress corrosion, then even though there was a net stress decrease at Stone Canyon and Chalfant, the foreshocks might have indirectly triggered the mainshock by increasing the rate of stress corrosion. However, whether such a pressure dependence in the stress corrosion rate exists is unknown [*Meredith and Atkinson*, 1983], and even if it does exist, the Landers and Joshua Tree foreshock sequences caused the pore pressure to decrease at their mainshock hypocenters. For these sequences, no triggering mechanism involving static stress changes or pore fluid changes seems appropriate.

It may be that the relation of foreshocks to the mainshock is extremely variable and that some of the time, foreshocks trigger the mainshock and some of the time they do not. That possibility cannot be rejected based on the results of this study. It is also worth noting that our analysis is for the static effects in an isotropic earth. If, for instance, high-pressure fluid were preferentially communicated through the fault zone, it might trigger the mainshock even though our analysis indicates that should not happen. It is also possible that dynamic stresses from the foreshocks could weaken the fault near the mainshock hypocenter, thereby allowing slip at lower driving stress. Despite these limitations our results suggest that theories of foreshock generation requiring the static stress changes from the foreshocks to trigger the mainshock in a kind of cascading failure are not universally applicable. Apart from the Mount Lewis example, the evidence for this kind of triggering is weak, at best, and the evidence against is strong, particularly in the Joshua Tree example.

Several authors [*Das and Scholz*, 1981; *Dieterich*, 1992; *Ohnaka*, 1992] have proposed that foreshocks are simply a by-product of an aseismic nucleation process. This viewpoint is based on theoretical modeling and laboratory simulation of earthquake nucleation showing that the dynamic instability is preceded by a period of stable sliding

within a small patch around the eventual hypocenter. In these models, foreshocks are incidental to the nucleation process and occur on asperities within the nucleation zone that fail from the load imposed by the ongoing creep around them. If the nucleation zone is homogeneous in strength and stress, there are no foreshocks. Because the foreshocks are incidental to the nucleation process in this model, the stress changes from the foreshocks are not required to have any particular relation to the mainshock failure mechanism. If the fault is planar within the nucleation region, then the static stress changes from the foreshocks at the mainshock hypocenter will likely be consistent with the failure mechanism of the mainshock. For other geometries this need not be the case. Our stress-change observations are consistent with this view of foreshock generation.

If foreshocks are indeed a seismic manifestation of an aseismic nucleation process, then their distribution and kinematics provide constraints on the nucleation process. The distribution of foreshocks would provide information about the size of the nucleation zone and its relation to mainshock magnitude. There is debate about the size of the nucleation zone and whether it is large enough to be observable. *Dieterich* [*1986*] concludes that the radius of the nucleation zone will be too small to observe unless the critical slip displacement D_C is considerably larger for earthquake faults than for laboratory faults. *Ohnaka* [1992] models nucleation as taking place at a strength heterogeneity on the fault with the size of the heterogeneity controlling the size of the nucleation zone. In this model, strength increases with distance from the center of the nucleation zone, so that stable slip can occur within the nucleation zone. As slip progresses, the nucleation zone grows until a critical size is reached and dynamic rupture ensues. *Ohnaka* [1993] used foreshocks of the 1978 Izu-Oshima earthquake ($M_{JMA} = 7.0$) to estimate the size of the nucleation zone. He found that the foreshock zone attained a size of 10 km and that it expanded with time, as required by his model. However, the foreshock sequence occurred entirely offshore, so that seismograph coverage was less than optimal. Many of the events were located kilometers off the inferred fault trace, so there is question about the accuracy of the estimate. Recent observations of the seismic nucleation phase [*Ellsworth and Beroza,* 1995], if interpreted in terms of an aseismic nucleation process, yield a nucleation zone that scales with mainshock magnitude, and the size of that zone ranges from 600 to 6000 m for earthquakes with M_W 6.5.
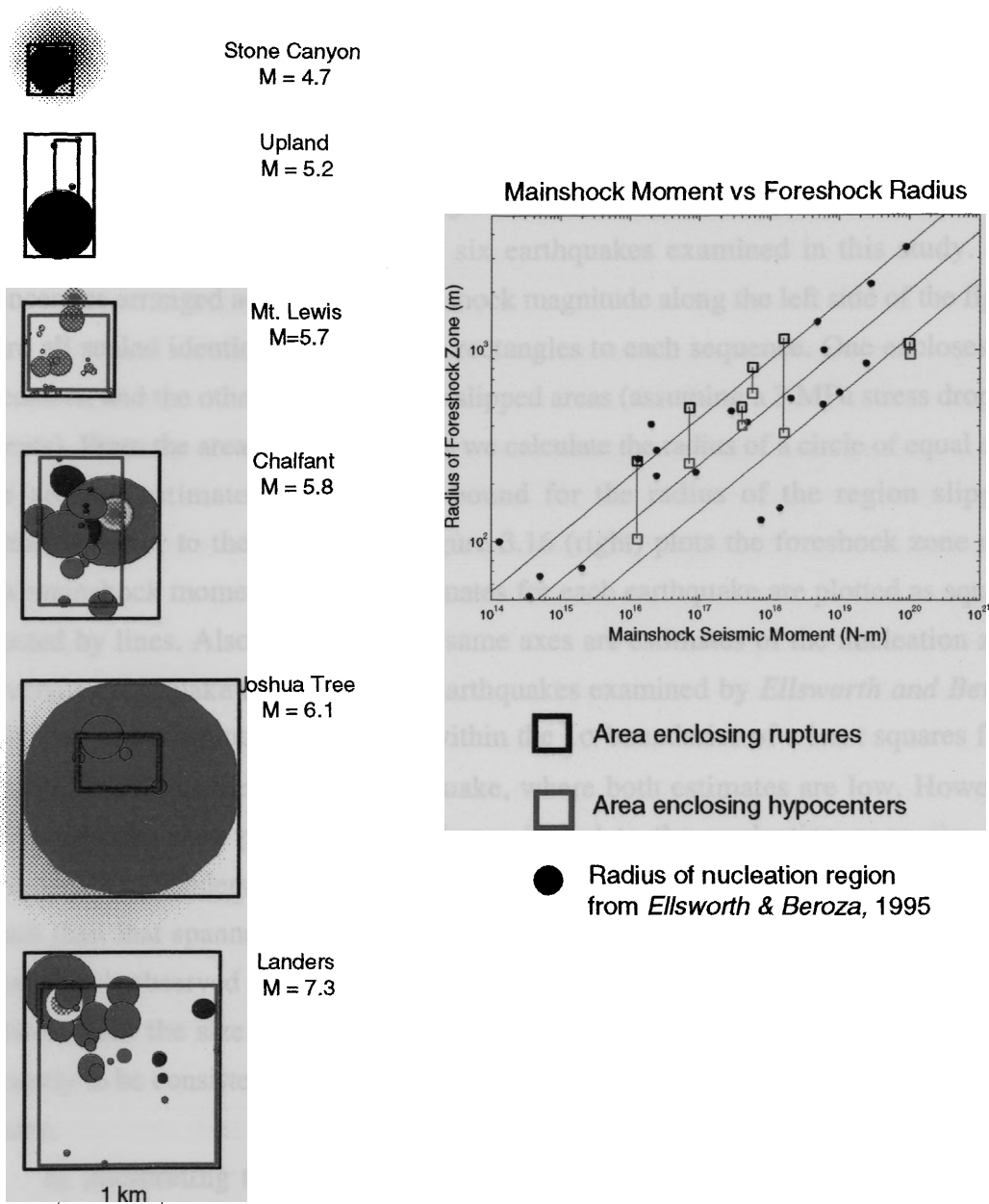
Figure 3.16. Comparison of foreshock zone dimension to mainshock moment. (left) Source disks of the six foreshock sequences projected onto their respective mainshock fault planes (from Figures 7-13). The rectangles superimposed on the plots indicate two ways of measuring the size of the foreshock zones. The outer rectangle encloses the source disks (based on 3-MPa stress drop), and the inner rectangle encloses the hypocenters. From the rectangle areas we calculate the radii of equivalent circles, and these are plotted (right) against mainshock moment. For each event the two estimates of source radius are connected by a line. On the same graph are plotted the estimates of source radius versus mainshock moment from the *Ellsworth and Beroza* [1995] study of the seismic nucleation phase. The straight lines are a least squares fit to the data and the 1σ boundaries from the fit.

Assuming that the extent of the foreshocks provides at least a rough estimate of the size of the nucleation zone, we can compare our observations of foreshocks to specific predictions of the models just mentioned. A straightforward estimate of the foreshock zone size is given by the smallest rectangle that encloses all the hypocenters when they are projected on the mainshock fault plane. Figure 3.16 shows graphically our estimates of the foreshock sequence dimensions for the six earthquakes examined in this study. The sequences are arranged according to mainshock magnitude along the left side of the figure and are all scaled identically. We fit two rectangles to each sequence. One encloses the hypocenters, and the other encloses all the slipped areas (assuming a 3 MPa stress drop for all events). From the area of each rectangle we calculate the radius of a circle of equal area. These are our estimates of the lower bound for the radius of the region slipping aseismically prior to the mainshock. Figure 3.16 (right) plots the foreshock zone radii versus mainshock moment. Our two estimates for each earthquake are plotted as squares connected by lines. Also, plotted on the same axes are estimates of the nucleation zone radii versus earthquake moment for 21 earthquakes examined by *Ellsworth and Beroza* [1995]. Our lower bound estimates are within the 1σ boundaries of a least squares fit to their data for all but the Landers earthquake, where both estimates are low. However, since foreshocks may provide only a lower bound to the nucleation zone size, the underestimate at Landers can be explained by invoking aseismic slip over a larger area of the fault than that spanned by the foreshocks. Alternatively, if the $M_W = 4.4$ subevent to the mainshock observed by *Abercrombie and Mori* [1994] is considered as an immediate foreshock, then the size of the foreshock zone for Landers would very likely increase sufficiently to be consistent with the *Ellsworth and Beroza* [1995] predictions of nucleation zone size.

In interpreting the apparent relation between foreshock zone dimensions and mainshock size shown in Figure 3.16, it is important to understand how the limitations of the data analyzed in this study may have affected this result. Obviously, the fewer the number of foreshocks, the harder it is to define the foreshock zone. In the limiting case of one foreshock the area of a rectangle enclosing the hypocenters would be zero, although the area enclosing the rupture might be large. More significantly, if swarms with no mainshock were plotted on the same figure, there would probably be no correlation between swarm dimensions and mainshock magnitude.

If the nucleation zone grows with time, as predicted by the *Ohnaka* [1992] model, then the size of the foreshock zone should also increase with time. However, since the location of individual foreshocks may be controlled partly by the mechanics of the nucleation process and partly by the location and characteristics of individual asperities, the sequence is not likely to grow outward uniformly, even if the nucleation zone is expanding uniformly. Instead, the foreshock locations may only trend outward. With the few events in the sequences we examine, such a trend could easily be masked by the "noise" from the asperity distribution. *Abercrombie et al.* [1995] examined the Landers foreshock sequence looking for indications of expansion with time and found that for the immediate foreshocks there was some indication that the zone of foreshocks expanded with time at a rate of about 5 to 10 cm/s, but this interpretation depended partially on treating one of the event locations as an outlier, an assumption that is not absolutely required by the observations.

To search for possible growth of the foreshock sequences with time, we examine two possible measures of growth, the RMS distance from the sequence centroid versus time and the RMS distance from the mainshock hypocenter versus time. Plots of these quantities are shown in Figure 3.17 for the Chalfant, Landers, and Mount Lewis sequences, the three sequences with enough events that a trend might be meaningful. Figure 3.17 (left) shows distance from the centroid versus time, and Figure 3.17 (right) shows distance from the mainshock hypocenter versus time. In each plot a least squares fit line is shown as well. Chalfant and Landers show a slight growth with time, as indicated by the upward slope of the lines in the left-hand plots, but the apparent growth is not statistically significant (R=-0.15, R=-0.17). Both of these sequences show a much stronger trend for the foreshock hypocenters to move toward the mainshock hypocenter with time (R=0.53, R=0.70). The Mt Lewis sequence appears to grow outward with time and shrink toward the hypocenter. The correlation is quite strong for both relations but should be interpreted with caution since the strength of the correlation depends entirely on two points. These results suggest that there may be more of a tendency for the foreshock zone to shrink toward the mainshock hypocenter than to grow outward. This behavior would be consistent with observations of *Ishida and Kanamori* [1978] and with modeling results by *Dieterich* [1992] showing that for faults with rate- and state-dependent strength, the earthquake nucleation process involves localization of slip to a subpatch, whose dimensions scale with the characteristic slip distance D_C.
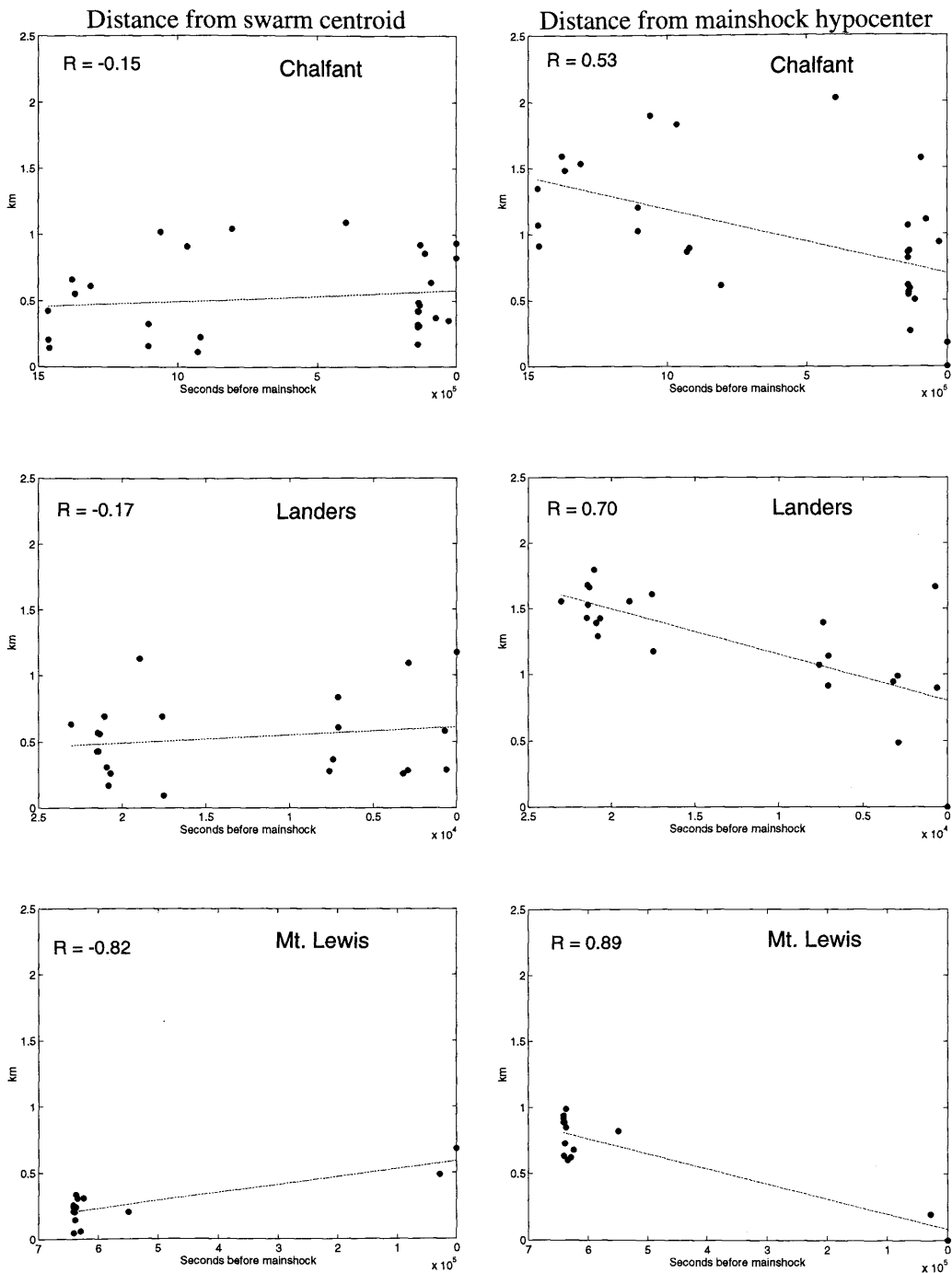
Figure 3.17. Foreshock sequence evolution with time. (left) distance of the foreshocks from the geometric mean of the foreshock cluster as a function of time before the mainshock. (right) Distance of the foreshocks from the mainshock hypocenter as a function of time before the mainshock. For each plot a least squares fit line to the data is also displayed. Correlation coefficients *R* are also shown. Only data from the Chalfant, Landers, and Mount Lewis sequences are shown since these are the only sequences with enough foreshocks to clearly define any trends that might exist.

The reason why some earthquakes are preceded by foreshocks and others are not is still unknown, but fault zone heterogeneity may be an important factor. The idea that foreshocks are associated with fault zone heterogeneity goes back to at least *Mogi* [1963], and there is considerable observational evidence for that association. For instance, *Jones et al.* [1982] concluded that the 1975 Haicheng earthquake ($M_L = 7.3$) probably nucleated at an en echelon fault step. *Jones* [1984] showed that of seven California earthquakes with foreshock sequences, four were associated with fault zone discontinuities and the other three were possibly associated with fault zone discontinuities. *Lindh et al.* [1978] observed a change in P/SV ratios between foreshocks and aftershocks for three California earthquakes that they attributed to a systematic change in stress or fault orientation in the source region. There is a strong inverse relation between depth of mainshock and foreshock sequence duration [*Jones*, 1984], which was attributed to the increase in minimum compressive stress with depth. In a more recent study, *Abercrombie and Mori*[1995] observed a similar decrease in number of foreshocks with depth and a dependence on focal mechanism of the mainshock. They suggested that the inverse relation with depth was due, at least partially, to the decrease in crustal heterogeneity with depth.

We can investigate the relation between crustal heterogeneity and foreshock generation using the results of this study. If we use the deviation of the fault from simple planar structure as a measure of heterogeneity, we can look for a relation between the amount of deviation and the number of foreshocks. There are a number of potential pitfalls with this approach. For instance, our measure of heterogeneity will not account for all sources of strength and stress variations, there may not be enough foreshocks to define the geometry of the fault, the number of foreshocks recorded might be biased because of differences in network sensitivity, and the choice of temporal and spatial windows used to identify immediate foreshocks could bias the results. Thus any relation that emerges from this analysis must be regarded as being suggestive rather than definitive.

We think that differing network sensitivities are unlikely to have biased our results. The seventh row of Table 3.1 shows the number of foreshocks recorded by the networks for each mainshock, and the bottom row shows the average distance from the mainshock of the five nearest stations for each sequence. If the variation in number of events is due to differing station distributions, then the number of foreshocks should be inversely related to average station distance. In fact, smaller numbers do not correspond to larger distances. For instance, the Landers sequence with 30 recorded immediate
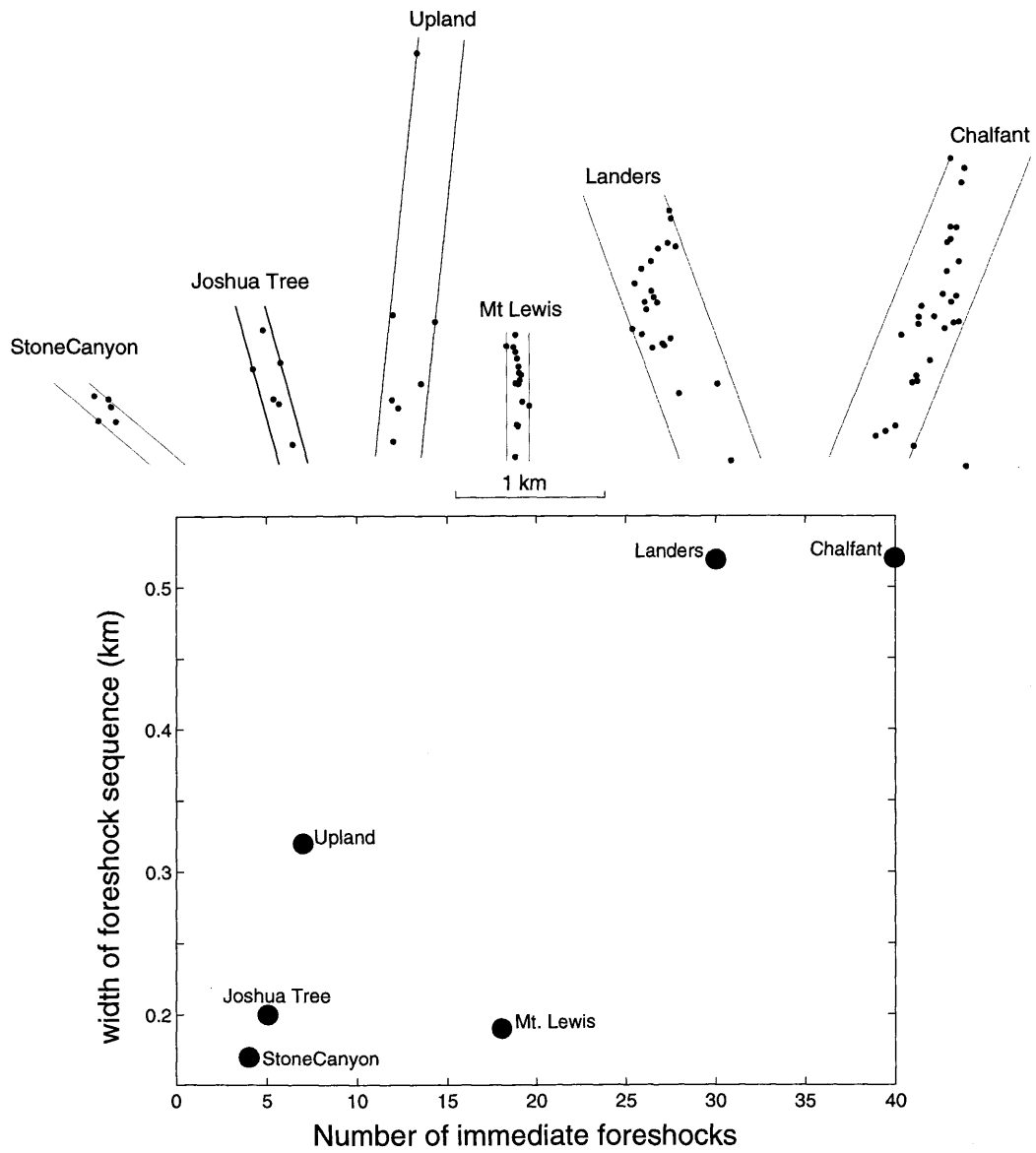
Figure 3.18. Fault zone width versus number of foreshocks. (top) Immediate foreshocks plotted in a plane perpendicular to the mainshock focal plane. The lines are drawn parallel to the average focal plane orientation of the foreshocks and just far enough apart to enclose all the foreshock and mainshock hypocenters. All sequences are plotted to the same scale. (bottom) Fault zone widths (measured perpendicular to the parallel lines for each sequence) plotted versus number of immediate foreshocks.

foreshocks has the greatest average distance, and Stone Canyon with only four immediate foreshocks has the smallest average distance.

All the sequences analyzed in this study were chosen using a spatial window of 2 km radius. This radius is large enough to avoid not selecting a potential foreshock because of network location error and small enough to avoid including seismicity from most nearby faults. Our results are not very sensitive to increases in this parameter because the distance to the nearest active fault is much greater than 2 km in all cases.

We used a time window of 30 days prior to the mainshock in our selection of immediate foreshocks. Our results are sensitive to this parameter choice. In the case of Mount Lewis most of the foreshocks we analyzed occurred 7 days before the mainshock, so a time window less than 7 days, for example, would exclude them. In the case of Chalfant the foreshocks occurred over a 3-week period, and a time window shorter than that would change our results.

The results of our comparison are shown in Figure 3.18. The top portion of the figure shows the immediate foreshocks plotted in a plane perpendicular to the mainshock fault plane. The parallel lines bounding the events in each sequence are drawn parallel to the average focal plane orientation of the foreshocks. Note that one of the Chalfant foreshocks is not enclosed by the lines for that sequence. This event is sufficiently distant from all the other events that there is some question as to whether it is actually part of the sequence. If this event was used, the correlation between fault zone width and number of foreshocks would be stronger. All sequences are plotted at the same scale. The foreshock zone widths are measured perpendicular to the parallel lines for each sequence. Figure 3.18 (bottom) shows those widths plotted against the number (from the catalog) of immediate foreshocks. With the exception of the Mount Lewis sequence there is a continuous increase of fault zone width with number of foreshocks. The correlation coefficient of the relation is 0.86. Although not definitive, these results certainly suggest that the strength of the heterogeneity is related to the number of foreshocks.

3.6 Summary

We have used high-precision relocations of the foreshock sequences of six California earthquakes to gain insight into the earthquake nucleation process. We find evidence that the foreshocks did not act to trigger the subsequent mainshocks by static stress changes. Of the six sequences, only one (Mount Lewis) had stress changes

consistent with static stress triggering. The stress changes from the Upland foreshock sequence were probably too small (< 0.001 MPa) to have been important. For the remaining four sequences the Stress-change distributions indicated that the foreshock sequences acted to destress the mainshock hypocenters. These results are consistent with a model in which the foreshocks are incidental to a predominantly aseismic earthquake nucleation process. We find that the size of the nucleation region, measured by the extent of the foreshocks, scales with mainshock moment in the same manner as determined independently by measurements of the seismic nucleation phase [*Ellsworth and Beroza*, 1995]. Thus we now have two completely independent suggestions that a slow nucleation process precedes some earthquakes. We also find evidence for slip localization, as predicted by some models of earthquake nucleation [*Dieterich*, 1992]. Fault zone heterogeneity appears to be an important factor in the location of the nucleation zone and in the number of foreshocks produced during nucleation. For three of the six sequences (Mount Lewis, Chalfant, and Landers) the mainshock hypocenter was located within 300 m, at most, of a significant change in strike or dip of the causative fault. The foreshocks to the Upland earthquake were located at a change of dip of the San Jose fault identified by *Hauksson and Jones* [1991]. Foreshock locations for the Stone Canyon and Joshua Tree earthquakes suggest that multiple fault planes may have been involved, but the scale of the possible heterogeneity is of the same order as the uncertainties in the locations.

Chapter 4 — Source array analysis of coda waves in central California: Implications for the mechanism of coseismic velocity changes

Abstract

Coda waves are often considered to be generated by backscattering of primary waves from randomly distributed heterogeneities in the crust; however, theoretical and experimental work indicates that much of the coda may be due to heterogeneity near the receiver. Knowing where the coda is generated is important for several reasons. Coda waves have been used to characterize: site amplification, scattering and attenuation throughout the crust, and velocity changes associated with large earthquakes. A lack of knowledge of where coda waves are generated, however, leads to ambiguous interpretations. In this study, we analyze 26 seconds of coda waves recorded at up to 78 stations using slowness stacking on 2 source arrays and find that at nearly every station, arrivals throughout the coda are strongly clustered in azimuth and takeoff angle at or near the direct arrival. This suggests that the coda consists primarily of waves scattered near the stations rather than of waves scattered from throughout the crust. This result holds even at stations very close to the sources where the amount of coda examined is about 6 times the direct S travel time. We use these results in combination with static stress modeling to examine the coseismic velocity decreases from the 1989 Loma Prieta earthquake observed by *Ellsworth et al.* [*1992*]. One possible mechanism for inducing such a change is a decrease in the mean stress from the mainshock slip; however, we find that this mechanism would produce a velocity increase in the region where velocity was observed to decrease. We conclude that the velocity decrease was more likely caused by crack opening or crack coalescence due to strong shaking from the mainshock.

4.1 Introduction

Seismograms of local earthquakes are observed to decay slowly to background levels after the arrival of the direct S wave. This "tail" of the seismogram is referred to as the coda, and is an incompletely understood part of the seismogram. Many features of the coda can be explained by assuming that the coda consists of waves that have been backscattered from random heterogeneities distributed throughout a volume that grows with lapse time. There are a diversity of models based on this assumption. *Aki and Chouet* [*1975*] modeled the coda as singly scattered surface waves in the shallow crust and as singly scattered S waves in the deep crust, and *Gao et al.* [*1983*] modeled the coda as multiply scattered body waves. *Frankel and Wennerberg* [*1987*] represented the coda decay using an "energy flux" model that accounts for both intrinsic and scattering attenuation. Although volume-scattering models like these can explain the shape of the coda, there is evidence that much of the coda may be due to more localized phenomena. *Levander and Hill* [*1985*] showed that coda waves could be produced by conversion of body waves to trapped surface waves. The coda may also be partially due to reverberations in layered structure between the source and receiver [*Bouchon, 1982*], or to near-receiver reverberations [*Phillips and Aki, 1986; Spudich and Bostwick, 1987; Blakeslee and Malin, 1990; Got and Coutant, 1996*]. This, more deterministic contribution to the coda, is probably always present to some degree, and it is useful to understand it for several reasons.

To the extent that coda waves are caused by near-site reverberations, their analysis can provide data useful for site-specific seismic hazard assessment. Relative amplification between hard rock and sediment sites has been found to be nearly constant from 10^{-5} to 0.2 g over a range of frequencies [*Phillips and Aki, 1986*]. By identifying the part of the coda due to site reverberations, and studying its decay characteristics and azimuthal variation, we may gain information that can be used to help predict the intensity of shaking in future large earthquakes.

Understanding the composition of the coda is also central to resolving the contradictory findings from coda Q studies. Coda Q is a parameter that describes the decay rate of coda waves. Under the single scattering assumption, coda Q measures the attenuation due to both scattering loss and to absorption. Coda Q is found to be strongly frequency dependent with values ranging from about 50 below 1 Hz to 2000 at 25 Hz [*Aki and Chouet, 1975*]. Although decreases in coda Q have often been found to correlate

positively with increases in seismicity [*Chouet, 1979; Gusev and Lemzikov, 1985; Jin and Aki, 1986*], coda Q may also increase with increased seismicity [*Jin and Aki, 1989*] or show no change [*Scherbaum and Kisslinger, 1985; Got et al., 1990; Got and Fréchet, 1993; Beroza et al., 1995*]. These inconsistencies may be attributed in part to differences in measurement technique or to regional differences in the predominant crack length. However, they may also be due in part to differences in the way the coda waves sample the crust.

Coda waves have also been used to search for coseismic changes in crustal velocity. *Ellsworth et al.* [*1992*] used multiplet earthquakes to search for coseismic velocity changes associated with the 1989 Loma Prieta earthquake. They studied multiplets located on the Calaveras and San Andreas faults in the vicinity of the mainshock that spanned the occurrence of the mainshock temporally and identified coseismic velocity decreases on source-receiver paths that traversed the aftershock zone. The change in slowness was quite large--large enough to be seen in the time domain. Nevertheless, it is difficult to interpret the change because the result has the same ambiguity as the result from an earlier study by *Poupinet et al.* [*1984*] of the 1979 Coyote Lake earthquake. There is little information on where the slowness change occurred. The change could be a near-surface phenomenon, confined to the fault zone, or distributed throughout a large volume of the crust.

In this study, we analyze coda waves from local earthquakes using two source arrays [*Spudich and Bostwick, 1987*]. The source arrays are clusters of earthquakes that, through Green's function reciprocity, can be treated as buried seismometer arrays responding to a seismic source at the true seismometer location. In this reciprocal viewpoint, conventional array analysis techniques applied to the seismograms yield the propagation direction and velocity of waves in the source region. Our data are 4055 seismograms recorded by up to 84 stations of the USGS Calnet array. These stations are 1 Hz vertical-component velocity transducers whose output is telemetered to a central recording facility at Menlo Park where the seismograms are digitized and archived. The two source arrays (Figure 4.1) are designated M1 and M2 after *Beroza et al.* [1995], and are centered around certain events used by *Ellsworth et al.* [*1992*] in their study of coseismic velocity changes.
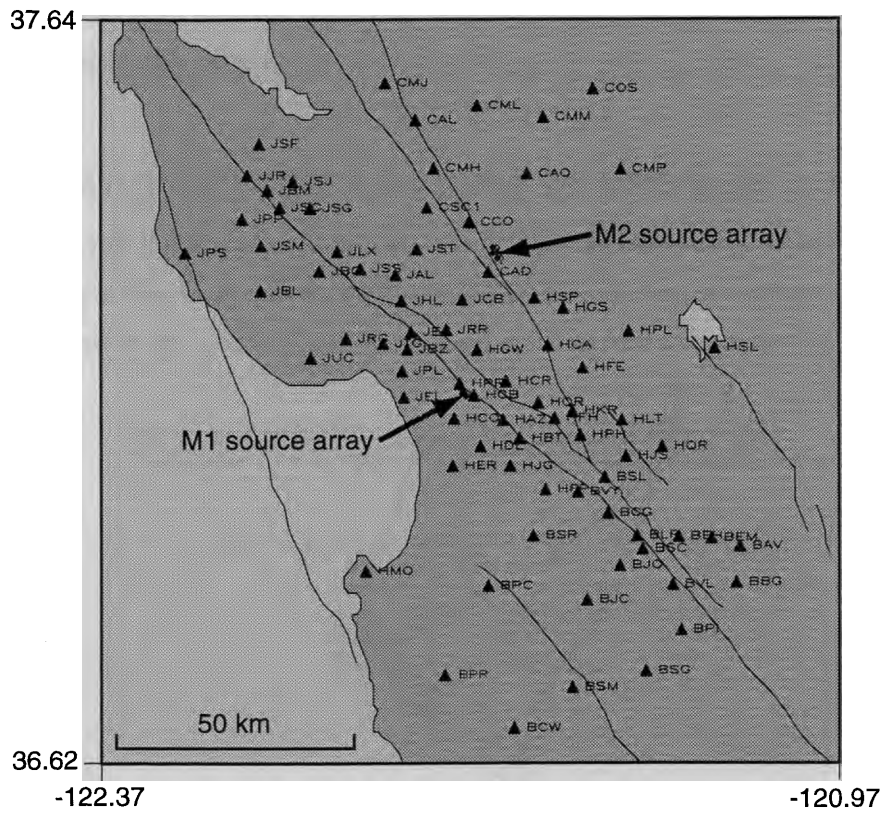
Figure 4.1. Study region showing the stations of the USGS Calnet used in this study and the location of the two earthquake source arrays.

We find that the coda is dominated by waves that left the source region in generally the same direction as the direct waves. This is true for all source-receiver azimuths and for lapse time to 6 *S*. We conclude that these waves must have been produced by near-station reverberations rather than by volume scattering. This implies that the coseismic velocity changes observed by *Ellsworth et al.* [*1992*] were probably confined to the shallow crust beneath the stations. We test whether the change in effective modulus was due to stress reorientation from the mainshock or was dynamically induced by modeling the velocity change expected from the mainshock slip distribution. We find that the observed velocity changes are inconsistent with the modeling results and conclude that the coseismic velocity change was dynamically induced.

4.2 Analysis of the coda using an earthquake array

We analyze coda waves from the two source regions using an earthquake array analysis technique due to *Spudich and Bostwick* [*1987*]. In this technique, standard array analysis is applied to the seismograms from a group of microearthquakes with very similar
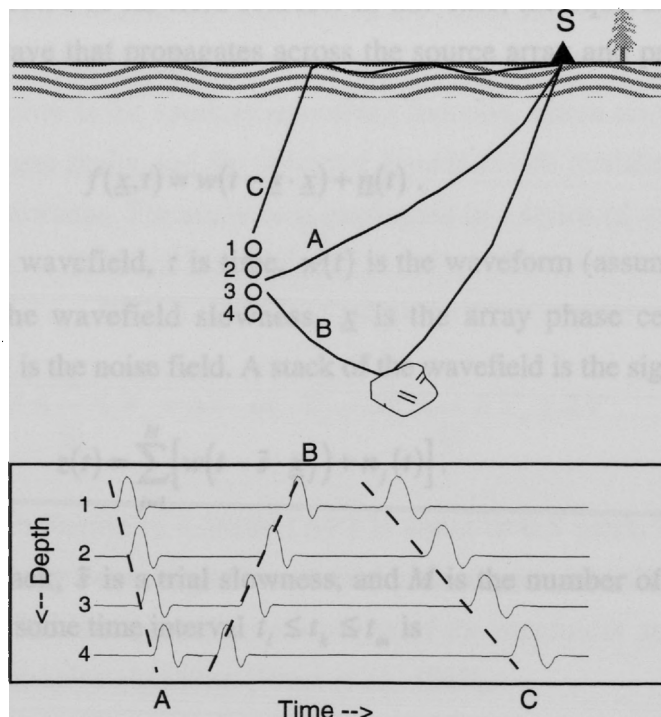
Figure 4.2. Schematic example of the source array technique after *Spudich and Bostwick* [*1987*]. (top) A vertical column of earthquake hypocenters numbered 1 through 4 and the ray paths for three arrivals in the seismograms recorded at station S. (bottom) The seismograms aligned on the origin times of the earthquakes and arranged by depth.

mechanisms to obtain information about the wavefield in the source region. For a 3-dimensional array it is possible to recover the full slowness field of the coda waves as they leave the source region. This is shown schematically in Figure 4.2 which is an adaptation of Figure 2 from *Spudich and Bostwick* [*1987*]. The upper half of Figure 4.2 shows a vertical column of earthquake hypocenters numbered 1 through 4 and the ray paths for three arrivals in the seismograms recorded at the station (S). The lower panel of the figure shows the seismograms aligned on the origin times of the earthquakes and arranged by depth. The direct arrivals (A) show the moveout expected from the increasing depth of the sources. Rays for arrival (B) leave the source region down-going and are later deflected up to the station, so the moveout has the opposite sense as that in case (A). Rays from arrival (C) leave the array vertically up and are later converted to surface waves, so the moveout is in the same sense as that of case (A), but greater.

A number of methods exist to extract information like this from seismograms recorded by arrays. In this study, we use delay-and-sum beam forming. We assume the source region is homogeneous and that the nearest scatterers are sufficiently distant that they all may be treated as far-field sources. In this case, the equivalent far-field source radiates a plane wave that propagates across the source array and produces a measured wavefield

$$f(\underline{x},t) = w(t - \underline{s} \cdot \underline{x}) + \underline{n}(t) \ . \tag{4.1}$$

Here $f(\underline{x},t)$ is the wavefield, t is time, $w(t)$ is the waveform (assumed coherent across the array), $\underline{s}$ is the wavefield slowness, $\underline{x}$ is the array phase center (mean sensor position), and $\underline{n}(t)$ is the noise field. A stack of the wavefield is the signal

$$z(t) = \sum_{j=1}^{M} \left[w(t - \tilde{s} \cdot \underline{x}_j) + n_j(t) \right] . \tag{4.2}$$

Here $z(t)$ is the stack, $\tilde{s}$ is a trial slowness, and M is the number of sensors. The stack power ($P(\tilde{s})$) over some time interval $t_i \le t_k \le t_m$ is

$$P(\tilde{s}) = \sum_{k=i}^{m} \left[z^2(t_k) \right]$$

$$(4.3)$$

$$= \sum_{k=i}^{m} \left[\left[\sum_{j=1}^{M} \left[w(t_k - \tilde{s} \cdot \underline{x}_j) + n_j(t) \right] \right]^2 \right]$$

If the noise $\vec{n}(t)$ is uncorrelated from channel to channel, its sum tends toward zero in the stack so that the stack power is primarily determined by the choice of $\tilde{s}$. When $\tilde{s} = \underline{s}$ the stack power is maximized.

Because the source arrays used in this study are deep (10 - 12 km) and stations are relatively close (< 30 km for most), we expect little surface wave excitation at the source. Instead, most of the energy should be in the form of body waves with either P or S velocity. Therefore, we restrict the slowness analysis to look only for waves with velocities near P or S. This assumption provides two advantages. First, the analysis can proceed more quickly because we don't search the entire slowness space. Second, many maxima in the slowness power spectra are artifacts caused by non-propagating signal (noise) or by sidelobes in the aperture smoothing function. These maxima are likely to lie outside the body wave shells, and the restricted domain avoids mistakenly choosing one of these as the true slowness. The analysis is performed in a series of overlapping windows beginning just prior to the P wave arrival and extending 26 seconds into the coda. For each time interval, $t_i \le t \le t_m$, $P(\tilde{s})$ is maximized subject to the constraint

$$V_p - \Delta V \le \frac{1}{|\tilde{s}|} \le V_p + \Delta V \quad \text{or} \quad V_s - \Delta V \le \frac{1}{|\tilde{s}|} \le V_s + \Delta V. \qquad (4.4)$$

The maximum perturbation in velocity (ΔV) is equal to 0.5 km/s. We accomplish the maximization by doing a coarse grid search in slowness space over the surfaces $|\tilde{s}| = 1 / V_p$ and $|\tilde{s}| = 1 / V_s$ to find the approximate location of the maximum and then refining the estimate using the simplex algorithm [*Press et al., 1987*].

4.3 Description of the source arrays

The earthquakes analyzed in this study were relocated using the cross correlation methods described in Chapter 1 of this thesis. Precise relative locations are important to the

array analysis because the magnitude of the location errors places a limit on the maximum frequency that can be used in computing the slowness power spectrum. The estimate of $P(\tilde{s})$ is not much affected by hypocentral errors at frequencies where the errors are less than 1/4 wavelength [*Spudich and Bostwick, 1987*]. A consequence is that the maximum usable frequency is about 1/4 the velocity divided by the hypocentral error. To use frequencies as high as 6 Hz for analysis of *S* waves requires that errors be limited to less than 150 m.

The M1 source array is located at the southern end of the Loma Prieta rupture zone at a depth of about 10.7 km and consists of 70 earthquakes with duration magnitudes ranging from 0.7 to 3.4 that occurred between November 20, 1989 and May 13, 1994. Because the M1 source array is located in a region of dense seismometer coverage, it is possible to get quite good relative relocations using only network picks. By using only stations within 40 km we were able to achieve location uncertainties (2.8σ) of 126 m horizontal and 270 m vertical. However, by using cross correlation picks we were able to achieve average location uncertainties of 40 m horizontal and 80 m vertical with average data residuals of 0.009 s. The mean number of observations per solution was 39. The array is about 850 m along strike and extends from about 10.2 to 11.2 km in depth. The event locations are shown in map and cross sectional views in Figure 4.3 and example seismograms are shown in Figure 4.4.

The M2 source array was also relocated using cross correlation techniques. It is at a depth of about 11.5 km on the Calaveras fault in the aftershock zone of the 1984 Morgan Hill earthquake and consists of 31 earthquakes with duration magnitudes ranging from 0 to 2 occurring between April 24, 1984 to May 2, 1990. The array is about 2.7 km along strike and extends from about 11.0 to 11.9 km in depth. The average data residual from the relative event locations (RMS) was 0.011 s and the average of the location uncertainties (2.8σ) was 65m horizontal and 154 m vertical. The mean number of observations per solution was 29. The event locations are shown in map and cross sectional views in Figure 4.5 and example seismograms are shown in Figure 4.6.
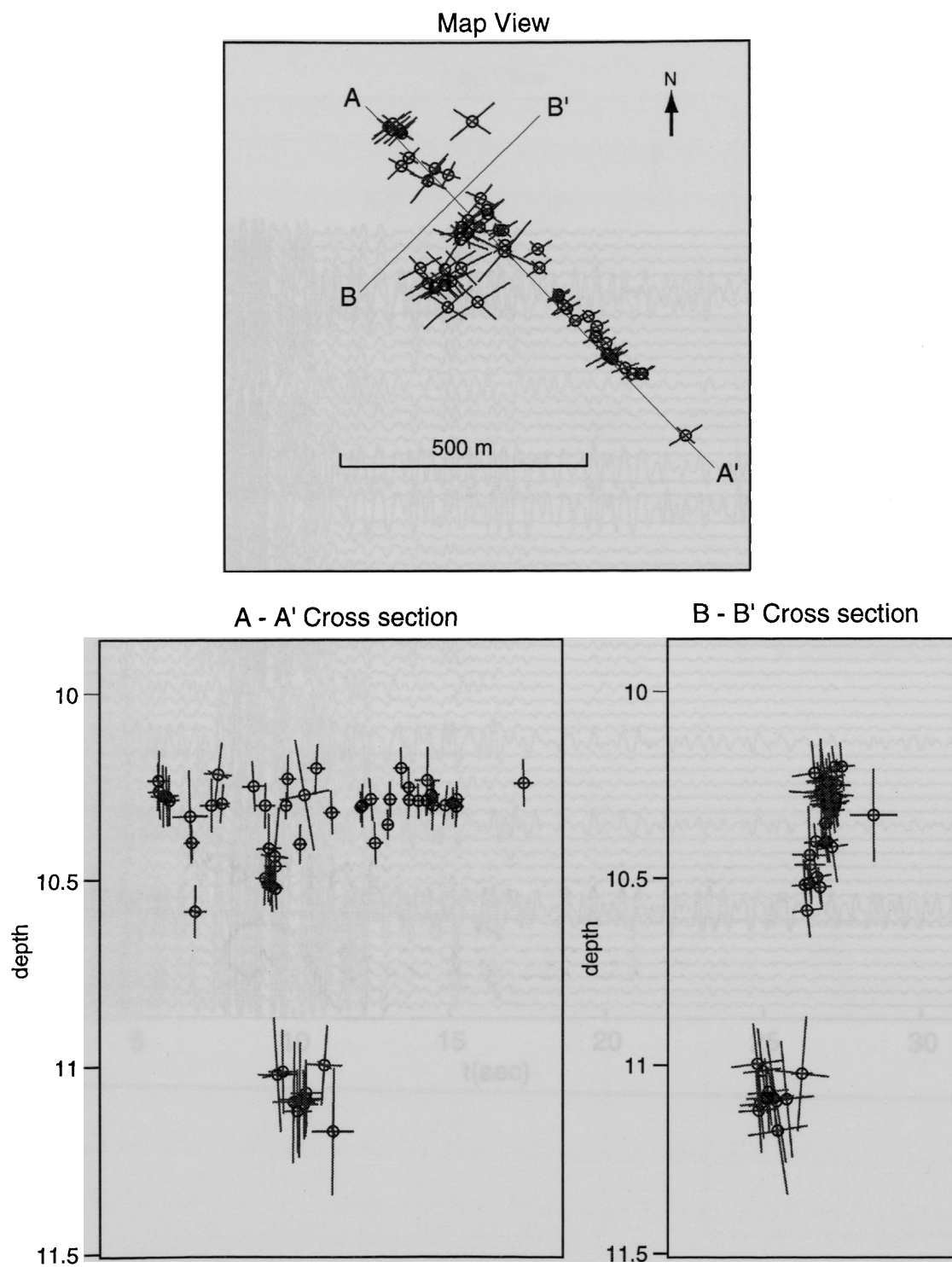
Figure 4.3. The M1 source array. (top) Map view of events. The bars are the axes of the 95% confidence ellipsoids for the relative locations projected on the map view. (bottom, left) The A-A' cross section looking to the NE. (bottom, right) The B-B' cross section looking along the fault to the NW.
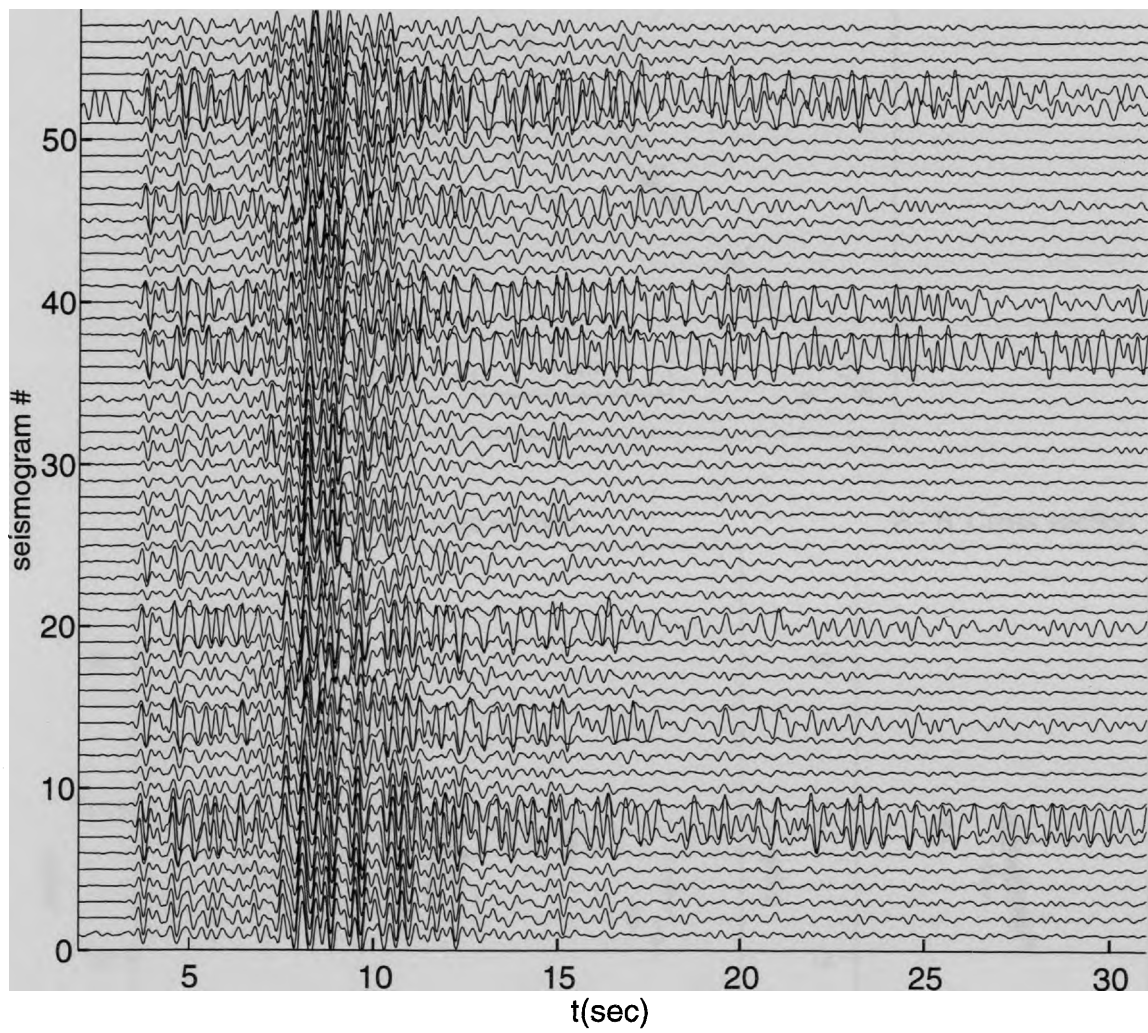
Figure 4.4. Seismograms from the M1 array recorded at station JEC. Traces are aligned on origin times from the relocations and are arranged by distance from JEC (closest at the bottom).
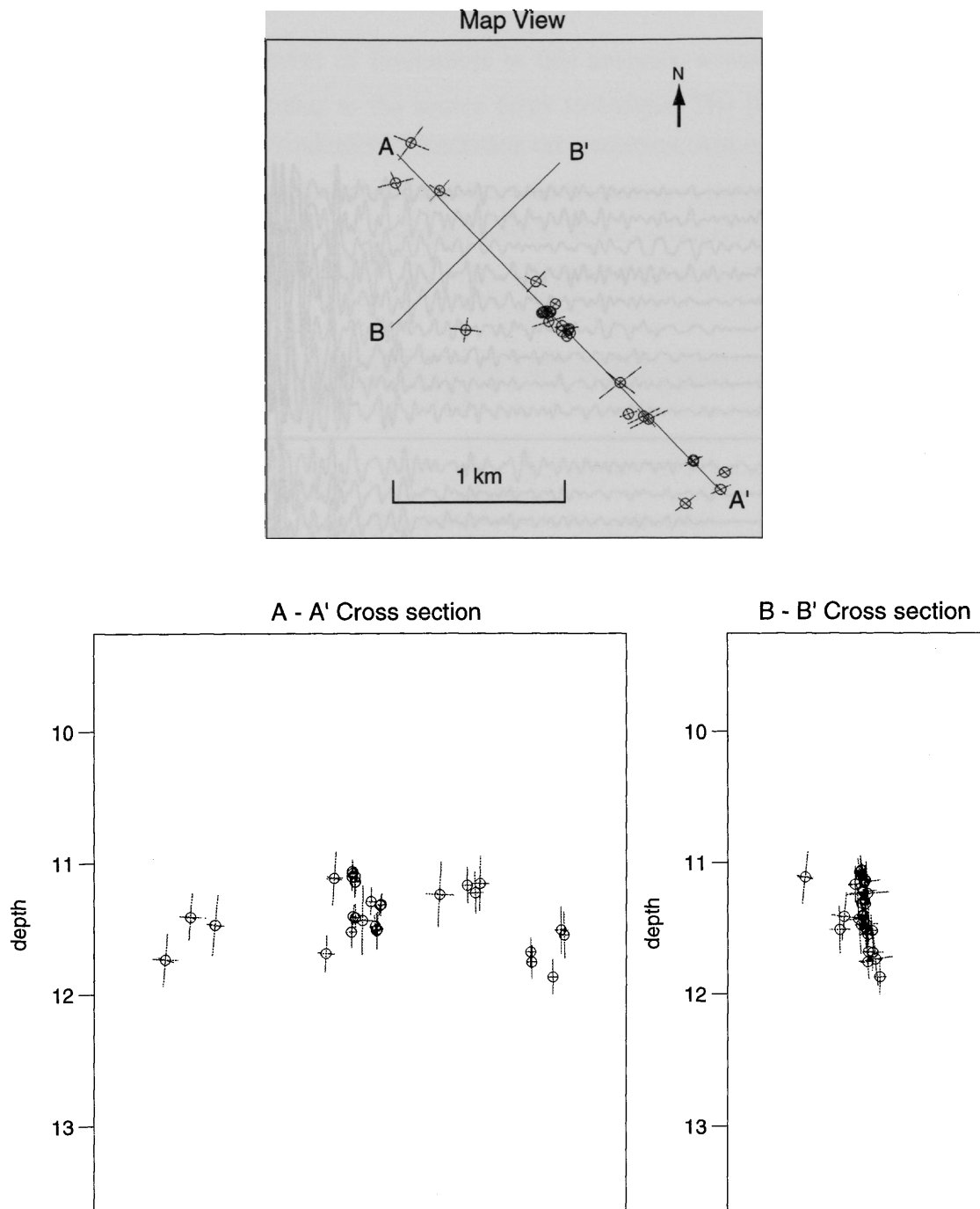
Figure 4.5. The M2 source array. (top) Map view of events. The bars are the axes of the 95% confidence ellipsoids for the relative locations projected on the map view. (bottom, left) The A-A' cross section looking to the NE. (bottom, right) The B-B' cross section looking along the fault to the NW.
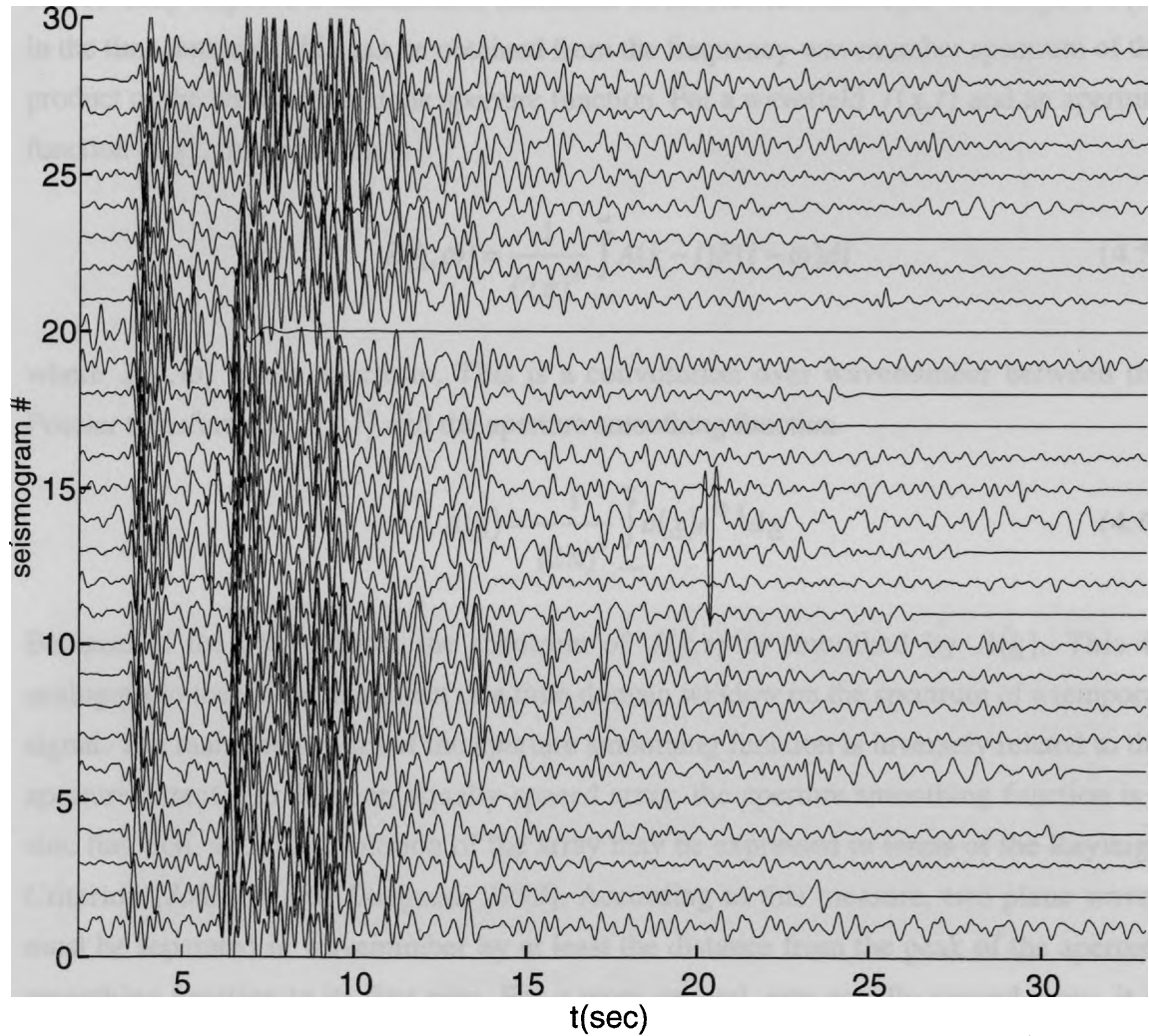
Figure 4.6. Seismograms from the M2 array recorded at station CAO. Traces are aligned on origin times from the relocations and are arranged by distance from CAO (closest at the bottom).

4.4 Limitations of the Analysis

4.4.1 Resolution

There are a number of limitations in this analysis, some present in any array analysis, and some peculiar to the source array technique. The limited aperture of the source array imposes a fundamental limitation on resolution. Although we compute $P(\tilde{s})$ in the time domain, $P(\tilde{s})$ can be obtained from the frequency-wavenumber spectrum of the product of the wavefield and the aperture function. For a wavefield $f(\underline{x},t)$ and an aperture function $a(\underline{x})$, the spectrum is

$$Z(\underline{k},\omega) = \frac{1}{(2\pi)^3} \int_{-\infty}^{\infty} A(\underline{k}-\underline{l})F(\underline{l}-\omega)d\underline{l} \qquad (4.5)$$

where $Z(\underline{k},\omega)$ is the spectrum. This is a convolution over wavenumber between the Fourier transform of $f(\underline{x},t)$ and the aperture smoothing function

$$A(\underline{k}) = \frac{1}{(2\pi)^3} \int_{-\infty}^{\infty} a(\underline{x})e^{i\underline{k}\cdot\underline{x}}d\underline{x} \ . \qquad (4.6)$$

Because of the convolution, the spectrum of $f(\underline{x},t)$ is smoothed by $A(\underline{k})$. This is analogous to the smoothing effect of a time-domain window on the spectrum of a temporal signal. The main lobe width of the aperture smoothing function is inversely related to the aperture extent. For a linear, equally-spaced array, the aperture smoothing function is a sinc function, and the resolution of the array may be expressed in terms of the Rayleigh Criterion [*Johnson and Dudgeon, 1993*]. According to this measure, two plane waves must be separated in wavenumber by at least the distance from the peak of the aperture smoothing function to its first zero. For a more general, non-equally-spaced array, it is convenient to define the resolution of the array as the distance between two points on the aperture smoothing function with amplitude equal to half of the maximum [*Johnson and Dudgeon, 1993*]. However defined, resolution in any direction is inversely proportional to the aperture extent in that direction. For source arrays this is controlled by fault geometry, earthquake occurrence, and the need to maintain waveform coherency. The repeating earthquakes around which the source arrays have been constructed are located on nearly planar fault segments, and have little extent perpendicular to their fault planes. Thus resolution in those directions is very low relative to resolution along the fault.
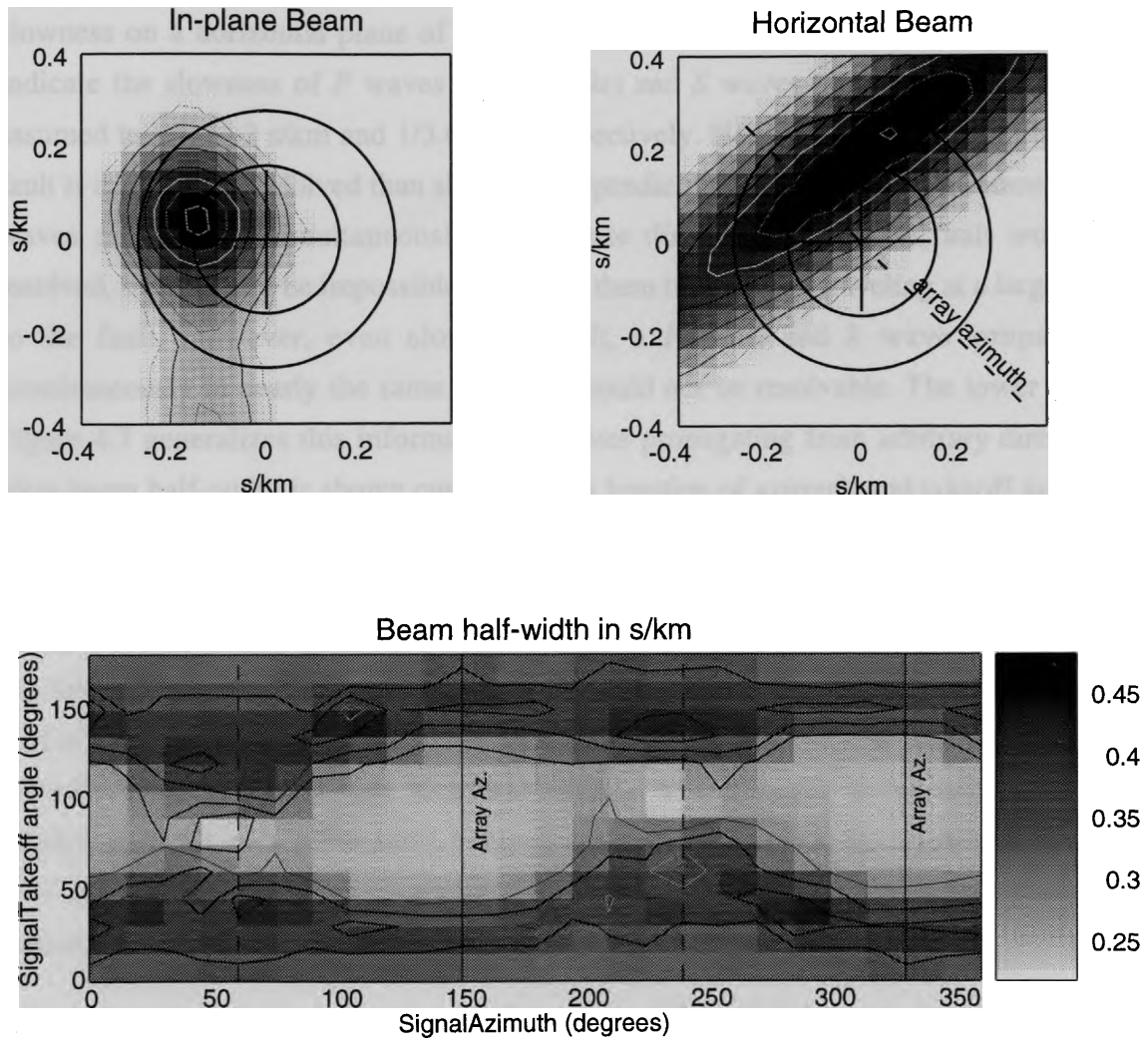
Figure 4.7. Resolution of M1 array as seen by station JEC. (top, left) Beam pattern on vertical plane parallel to fault. (top, right) Beam pattern on horizontal plane. (bottom) Beam pattern half-width as a function of wave azimuth and takeoff angle.

This is illustrated in Figure 4.7 which shows (top) beam patterns from the M1 source array as seen from station JEC and (bottom) beam half-width as a function of signal orientation. The left beam pattern is the apparent slowness on a vertical fault-parallel plane of a wave propagating from JEC to the array. The right beam pattern is the apparent slowness on a horizontal plane of the same wave. The concentric circles on each plot indicate the slowness of P waves (inner circle) and S waves (outer circle). These are assumed to be 1/6.2 s/km and 1/3.6 s/km respectively. Note that the slowness along the fault is much better resolved than slowness perpendicular to the fault. For instance, two P waves propagating simultaneously in opposite directions along the fault would be resolved, but it would be impossible to resolve them if they were traveling at a large angle to the fault. However, even along the fault, a P wave and S wave propagating simultaneously in nearly the same direction would not be resolvable. The lower half of Figure 4.7 generalizes this information to waves propagating from arbitrary directions. Here beam half-width is shown contoured as a function of azimuth and takeoff angle. In the calculations used to produce this plot, each plane wave had S wave velocity (3.6 km/s) and the beam width was measured on the surface of the S wave slowness sphere. Resolution is generally best for signals traveling in near-horizontal directions. The highest resolution is achieved in two small regions approximately normal to the array axes (the first at about 50° azimuth and 80° takeoff and the second at about 230° azimuth and 100° takeoff). However resolution decreases rapidly with changes in takeoff angle. The resolution off the ends of the array, although somewhat lower than the maximum, is stable over a much broader range of angles. The results shown in Figure 4.7, are specific to station JEC. However, the performance at most other stations is similar.

4.4.2 Aperture Ambiguities, Event mis-location, and Azimuth Bias

For arrays with 2-D or 1-D apertures, waves propagating from different directions at the same speed can produce the same spectrum [*Johnson and Dudgeon, 1993*]. For instance, a linear array has cylindrical symmetry, and cannot distinguish among waves propagating at the same angle to the symmetry axis. Because the source arrays are nearly planar they have near-mirror symmetry and may poorly distinguish different waves with the same apparent velocity in the array plane. This is illustrated in Figure 4.8 which shows two plane waves incident on a horizontal planar array. One wave is propagating downward with a velocity of 3.5 at an angle of 30° to the array. The array resolves this as a wave

propagating horizontally to the right with a velocity of 7. A second wave is shown propagating upward with a velocity of 6.06 at an angle of 60° to the array. It has the same apparent velocity as the first and so is indistinguishable.
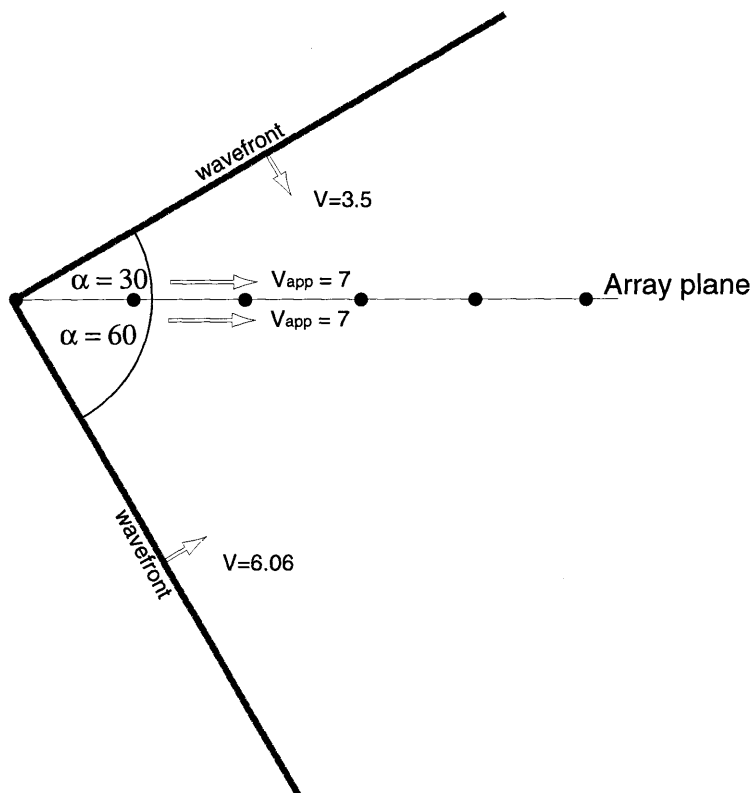
Figure 4.8. Schematic illustration of aperture ambiguity for a planar aperture. Wavefront approaching from beneath the array has a true velocity of 6.06 and an angle relative to the array of 60°. Wavefront approaching from above the array has a true velocity of 3.5 and an angle relative to the array of 30°. Both have an apparent velocity of 7 within the aperture.

Our arrays are not perfectly planar, so they have some resolution of the perpendicular component of slowness, and could distinguish the two waves of Figure 4.8. However, because of the finite sample rate and limited extent of the arrays perpendicular to their fault planes, two waves propagating nearly perpendicular to the fault planes would have phase differences too small to be resolvable.

Resolution measures the ability of the array to distinguish multiple waves simultaneously propagating through the array. However, a consequence of low resolution is the possibility of mis-identifying the true slowness of a wave. There can be many local maxima in the slowness power spectrum which are artifacts of the analysis. For instance, because the signals are temporally sampled, it is impossible to form exact delays for all possible slownesses, so it is sometimes impossible to estimate the power at the true slowness. Noise in the seismograms may also produce false maxima. Mis-identifying the maximum does little harm if the power spectrum has a compact main lobe since the chosen maximum is likely to be very near the true slowness. However, if the main lobe is very broad, this mistake could result in a significant error in slowness estimation. Restricting the range of possible slowness, as our algorithm does, helps mitigate, but does not eliminate, this problem.

Because the resolution of our source arrays has a directional dependence, errors in slowness estimation are also directionally dependent. To quantify this dependence we used Monte Carlo simulation [*Press et al., 1986*] to produce distributions of estimated azimuth, takeoff angle, and velocity for waves propagating along the array plane and normal to the array plane. The distributions were produced by varying the source locations within their probable uncertainties and are shown in Figure 4.9. For both arrays, azimuths are well constrained for waves propagating perpendicular to the array and more poorly constrained for waves propagating parallel to the array. This could be expected since the in-plane beam width is much narrower than the beam width perpendicular to the array plane (Figure 4.7). Takeoff angle resolution is not very dependent on wave azimuth since it is controlled by the in-plane beam width. Velocity is best resolved for waves propagating in the plane of the array. The M2 array has better resolution of azimuth and velocity because of its greater length (about 3 times the length of M1); however, its actual performance turns out to be poorer because the small size of its constituent events means that many of them are not available at most stations, or have much lower *snr* then the M1 events.

The B-B' cross section in Figure 4.3 shows the event hypocenters dipping to the SW at about 83°. Although this apparent dip to the west is consistent with the observation that the Loma Prieta earthquake occurred on a fault dipping to the west [*Dietz and Ellsworth, 1990*], it may also be at least partially an artifact from the known velocity contrast across the San Andreas fault, [*Aki and Lee, 1976; McNally and McEvilly, 1977;*
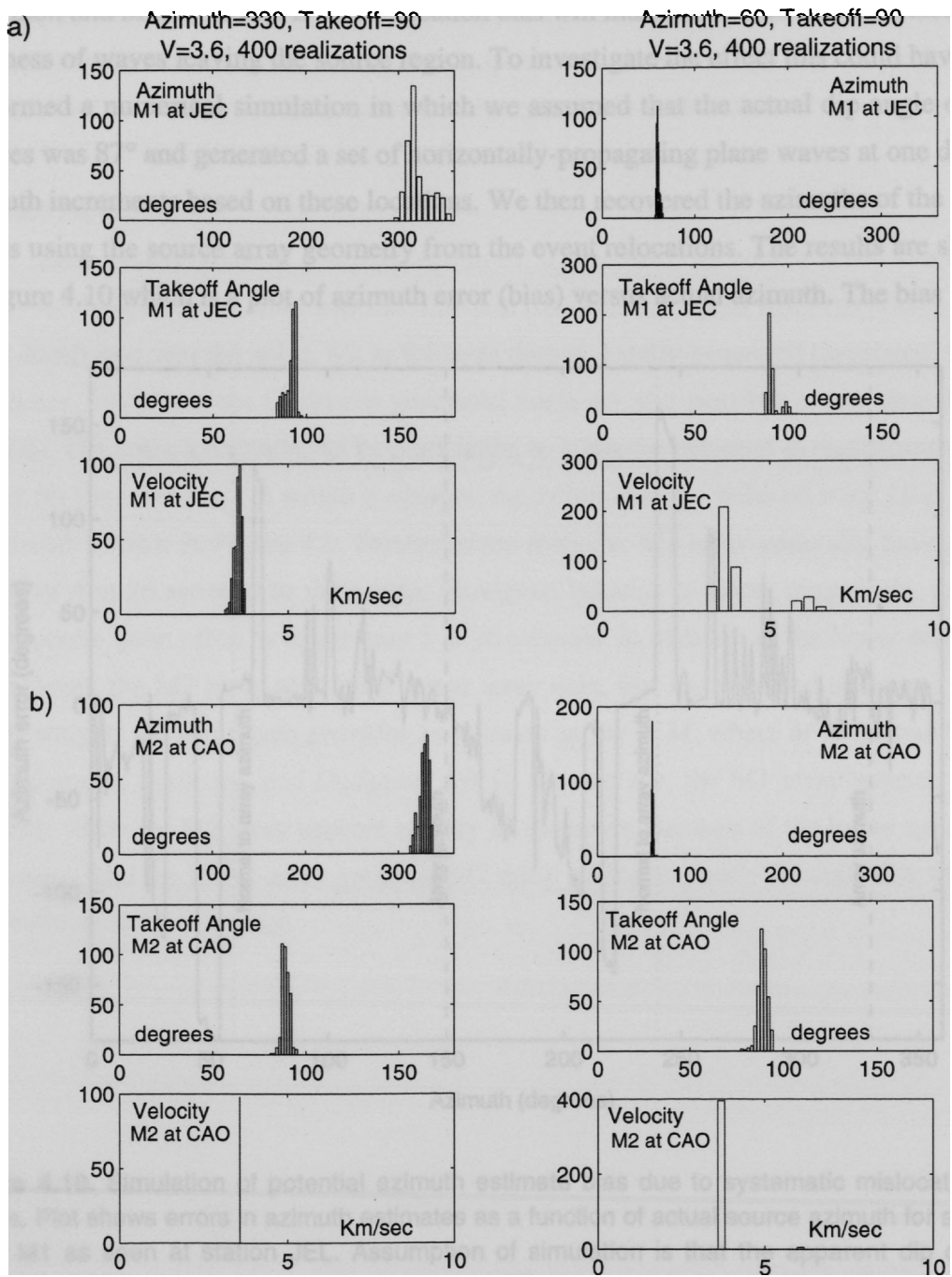
Figure 4.9. Distributions of parameter uncertainties as a function of source direction. (a) (left) Parameter estimate distributions for M1 source array as seen at station JEC for a source at azimuth 330° (in array plane) and (right) for a source at 60° (perpendicular to array plane). (b) (left) Parameter estimate distributions for M2 source array as seen at station CAO for a source at azimuth 330° (in array plane) and (right) for a source at 60° (perpendicular to array plane).

Ben-Zion and Malin, 1991]. If so the location bias will introduce a bias into the calculated slowness of waves leaving the source region. To investigate the effect this could have, we performed a numerical simulation in which we assumed that the actual dip angle of the sources was 87° and generated a set of horizontally-propagating plane waves at one degree azimuth increments based on these locations. We then recovered the azimuths of the plane waves using the source array geometry from the event relocations. The results are shown in Figure 4.10 which is a plot of azimuth error (bias) versus actual azimuth. The bias
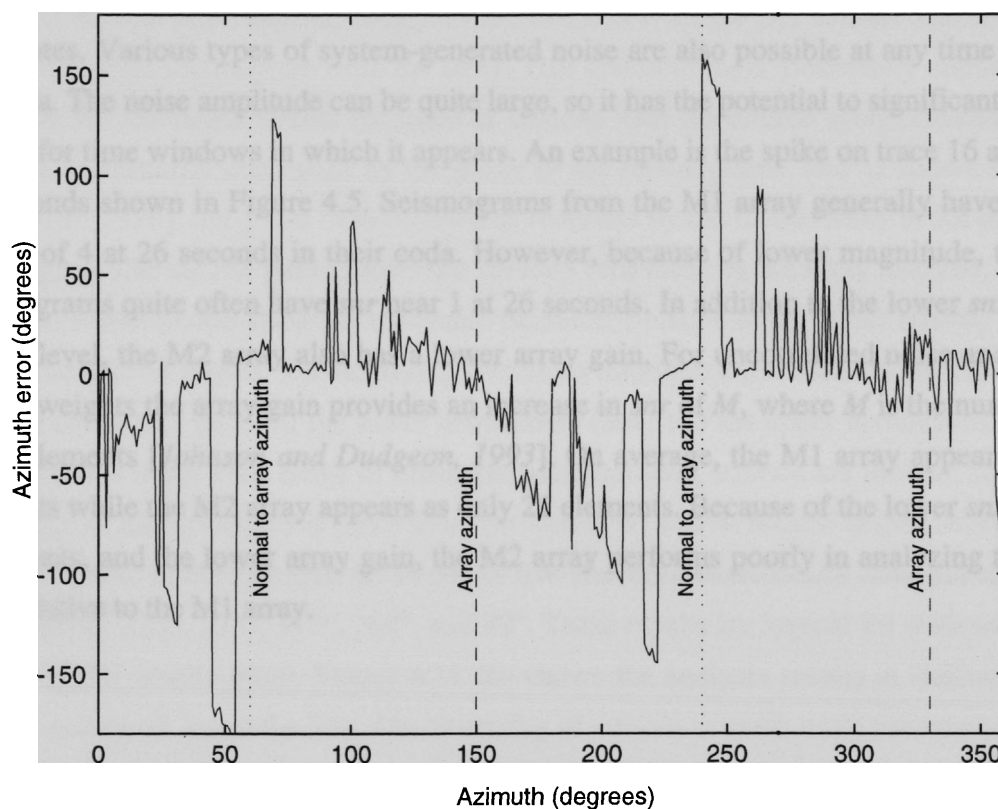
Figure 4.10. Simulation of potential azimuth estimate bias due to systematic mislocation of events. Plot shows errors in azimuth estimates as a function of actual source azimuth for source array M1 as seen at station JEL. Assumption of simulation is that the apparent dip of 83° exhibited by M1 seismicity is an artifact due to velocity contrast across the San Andreas fault and actual dip is 87°.

varies with azimuth, being smallest along the array azimuth and largest near the normal to the array azimuth. There the recovered azimuth can change suddenly from being nearly correct to being off by about 180°. These biases are, of course, dependent on the

assumptions of the simulation and only illustrate a possibility. Nevertheless, the behavior of some results discussed in section 4.5 is quite reminiscent of the bias behavior, and suggests that our results could be influenced by systematic mislocation of the array events.

4.4.3 Noise

Each seismogram is a superposition of signal from its source array event and background signal from other sources. Early in the coda the signal from the source array event dominates over the noise, but as the coda decays, locally-generated (unrelated) signal dominates. Various types of system-generated noise are also possible at any time during the coda. The noise amplitude can be quite large, so it has the potential to significantly alter results for time windows in which it appears. An example is the spike on trace 16 at about 20 seconds shown in Figure 4.5. Seismograms from the M1 array generally have *snr* in excess of 4 at 26 seconds in their coda. However, because of lower magnitude, the M2 seismograms quite often have *snr* near 1 at 26 seconds. In addition to the lower *snr* at the sensor level, the M2 array also has a lower array gain. For uncorrelated noise and equal sensor weights the array gain provides an increase in *snr* of M, where M is the number of array elements [*Johnson and Dudgeon, 1993*]. On average, the M1 array appears as 43 elements while the M2 array appears as only 21 elements. Because of the lower *snr* of the M2 events, and the lower array gain, the M2 array performs poorly in analyzing the late coda relative to the M1 array.

4.5 Results of the Array Analysis

The M1 source array was usable at 78 stations and the M2 array was usable at 12 stations. For each of these we calculated slowness power spectra in running widows 1.5 s long shifted by 0.2 s per estimate. The first window at each station began at the *P* arrival time, and there were 130 time steps (26 s) in all. For most stations this allowed the analysis to continue to the point where the coda had decayed to near the pre-*P* noise level.

Selected results for M1 are shown in Figure 4.11 (a-c). Figure 4.11 (a) shows the result for station JRR, approximately 14 km to the NW of the M1 events. The top panel shows a doublet seismogram from the array. This seismogram is moderately clipped, as is common for the larger events recorded at stations near the source array. However, our analysis is primarily controlled by the phase of the seismograms, and as shown by *Ellis and Lindh* [*1976*], the phase of seismograms recorded by the Calnet array is not distorted by clipping. The second panel shows the velocity recovered by the array analysis, and the third and fourth panels show the recovered azimuths (relative to the direct arrival) and the recovered takeoff angles. The scattering directions throughout the coda are summarized in the two equal area plots for the lower hemisphere (left) and the upper hemisphere (right). These show a fairly wide range of azimuths, although most arrivals are forward scattered. The range of takeoff angles is much more restricted, with most takeoff angles between 90° and 120°. Most of the azimuths are in one of five clusters symmetrically arranged about the array axis at 225°, 275°, 315°, 360°, and 40°. These results are typical for stations within 20 km of the source array. Figure 4.11 (b) shows the analysis results at station HMO, approximately 41 km to the SW. The clustering of arrivals is much more pronounced here. Virtually all arrivals are within a few degrees in azimuth of the direct arrival (220°) or are near an azimuth of about 80° (symmetric with respect to the array axis). Most takeoff angles are between 60° and 120°. There are many more arrivals with azimuths near 80° than with azimuths near 220° including much of the early *P* coda and the first 7 s of the *S* coda. This behavior is exhibited at stations where the direct arrivals leave the source array at large angles to the array axis, and is likely to be an artifact. That is, the cluster of arrivals near 80° probably have true azimuths near 220°, but have been mislocated because of low resolution normal to the array and bias in the array element locations. Figure 4.11 (c) shows the results at station BBG, about 69 km to the SE. Clustering is also pronounced here with one cluster at about the azimuth of the direct arrival (110°), a cluster at azimuth 150°, and a cluster at azimuth 190°. Most of the takeoff angles are between 50° and 90°.
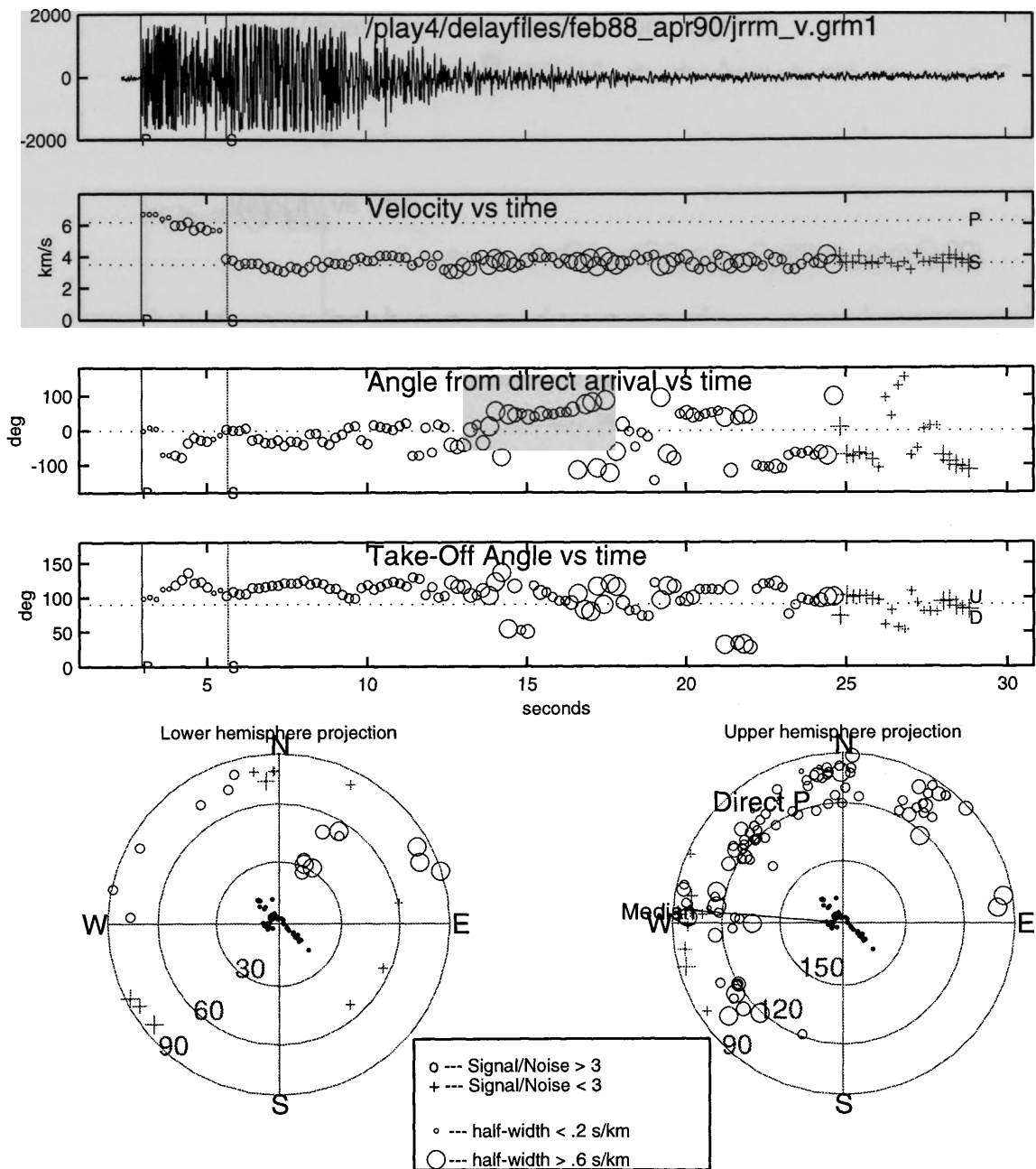
Figure 4.11. (a) Analysis summary at station JRR for M1 array. (top) Example seismogram from M1 array used in calculation of coseismic slowness change. (second) Velocity recovered from array analysis. (third) Scattering azimuth of coda waves relative to azimuth of direct arrival (from source location). (fourth) Takeoff angle of coda waves as a function of time. (bottom) equal area projections of coda wave scattering directions on lower hemisphere (left) and upper hemisphere (right). In all plots the symbol size is proportional to beam half-width. Arrivals represented with a "+" had an average *snr* less than 3.
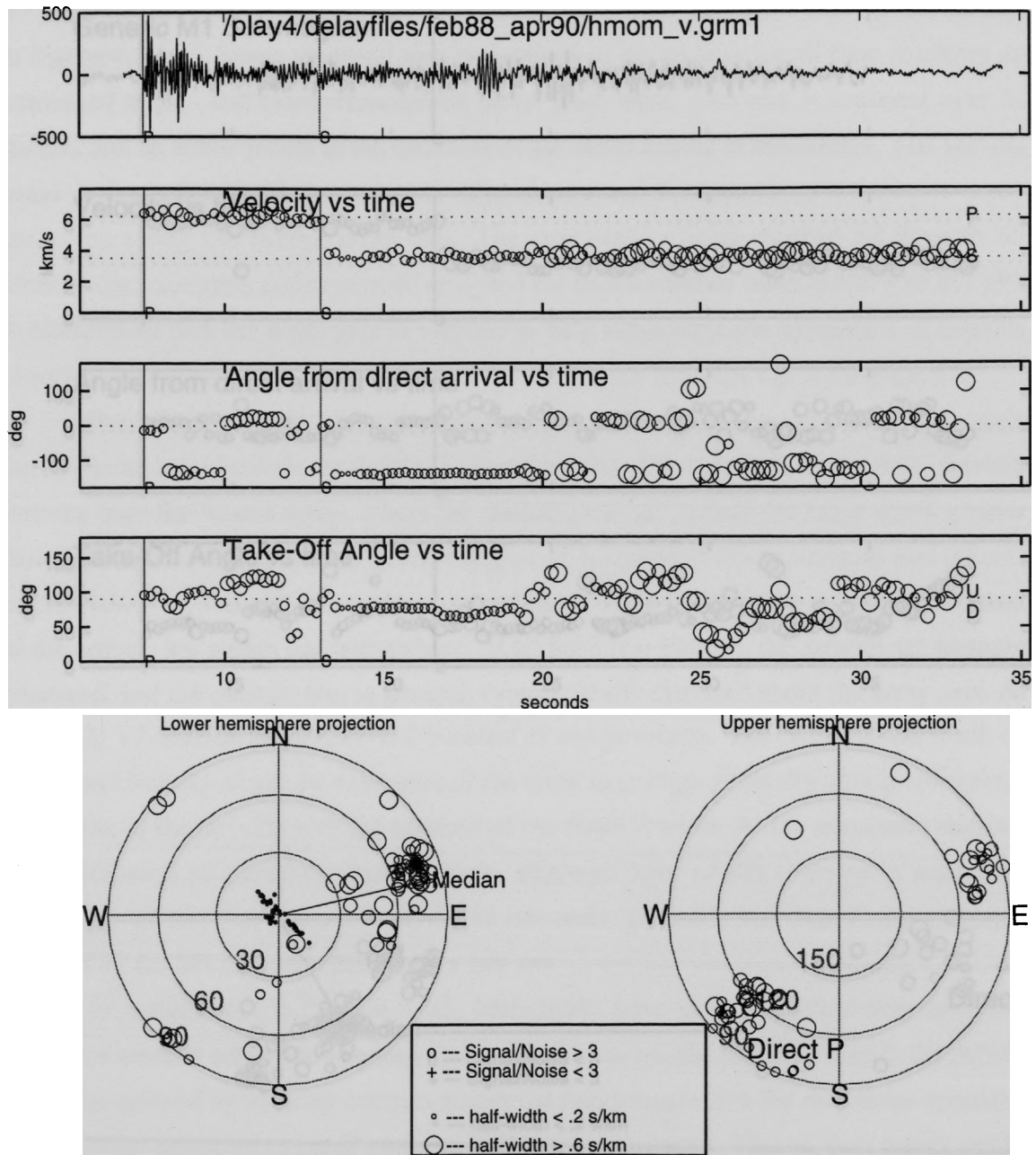
Figure 4.11. (b) Analysis summary at station HMO for M1 array. (top) Example seismogram from M1 array used in calculation of coseismic slowness change. (second) Velocity recovered from array analysis. (third) Scattering azimuth of coda waves relative to azimuth of direct arrival (from source location). (fourth) Takeoff angle of coda waves as a function of time. (bottom) equal area projections of coda wave scattering directions on lower hemisphere (left) and upper hemisphere (right). In all plots the symbol size is proportional to beam half-width.
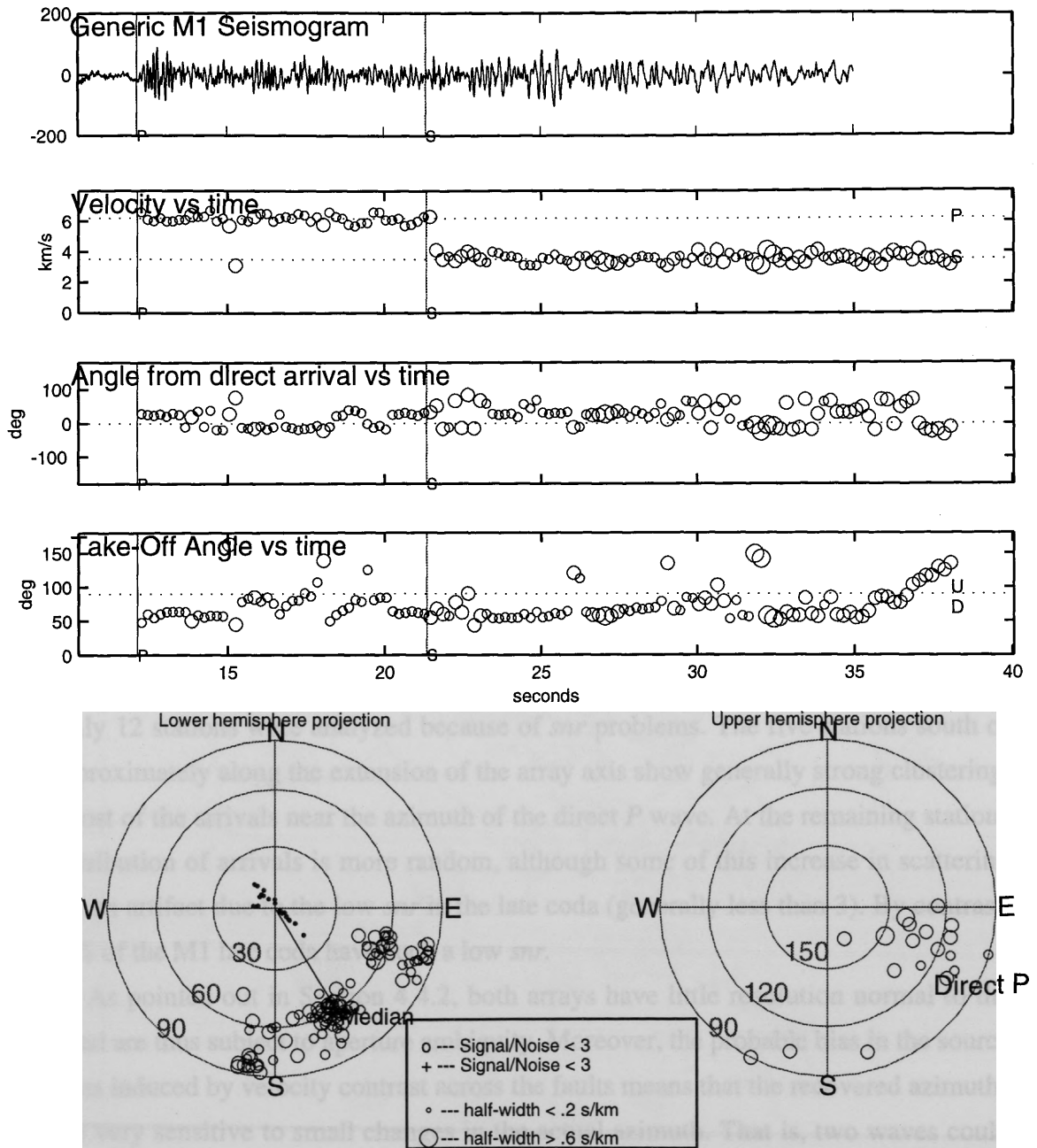
Figure 4.11 (c) Analysis summary at station BBG for M1 array. (top) Example seismogram from M1 array used in calculation of coseismic slowness change. (second) Velocity recovered from array analysis. (third) Scattering azimuth of coda waves relative to azimuth of direct arrival (from source location). (fourth) Takeoff angle of coda waves as a function of time. (bottom) equal area projections of coda wave scattering directions on lower hemisphere (left) and upper hemisphere (right). In all plots the symbol size is proportional to beam half-width.

Summaries of the analysis results are shown for M1 in Figure 4.12 (a) and for M2 in Figure 4.12 (b). These are equal area projections of the arrivals for all time windows on combined upper- and lower-hemisphere plots. Each equal area plot is centered over its station, and an arrow points in the direction of the direct arrival at that station. The vertical scale at the left side of the plot (for M1) shows the distance from the source array measured along the source array axis. The concentric circles marked $2S$ through $6S$ indicate the maximum extent of coda analyzed for stations within each circle. The M1 plot is oriented so that the array axis is vertical to help emphasize the symmetry of arrivals observed at many of the stations. (North is 30° clockwise from the top of the page.)

For M1, at stations where the analysis was restricted to the early S coda (outside the $2S$ circle) most arrivals are tightly clustered near the direct arrivals. In contrast, at many stations near the source array, where the analysis was performed for lapse times greater than $4S$, there is a significantly greater degree of scattering both in azimuth and takeoff angle. However, at nearly all stations, regardless of distance from the source, all or most of the arrivals are within one hemisphere. At all but a few stations, the arrivals are strongly clustered, and the clusters are, in general, symmetrically disposed about the array axis. At M2, only 12 stations were analyzed because of *snr* problems. The five stations south of M2 approximately along the extension of the array axis show generally strong clustering, with most of the arrivals near the azimuth of the direct P wave. At the remaining stations the distribution of arrivals is more random, although some of this increase in scattering may be an artifact due to the low *snr* in the late coda (generally less than 3). By contrast, only 8% of the M1 late coda have such a low *snr*.

As pointed out in Section 4.4.2, both arrays have little resolution normal to the array and are thus subject to aperture ambiguity. Moreover, the probable bias in the source locations induced by velocity contrast across the faults means that the recovered azimuths may be very sensitive to small changes in the actual azimuth. That is, two waves could have only slightly different azimuths, yet one azimuth would be correctly recovered by the analysis while the other would be recovered as its mirror image. Indeed, some of the data require the symmetry to be an artifact. At stations JUC, HGS, HOR, HKR, and HLT (Figure 4.12a) the computed azimuths of the P wave arrival and the first few seconds of the P coda are near-mirror images of the azimuth to the station. This condition was observed at stations on both sides of the source. If this is not an artifact, it implies that waves leaving the source traveling away from the station were able to arrive at the station
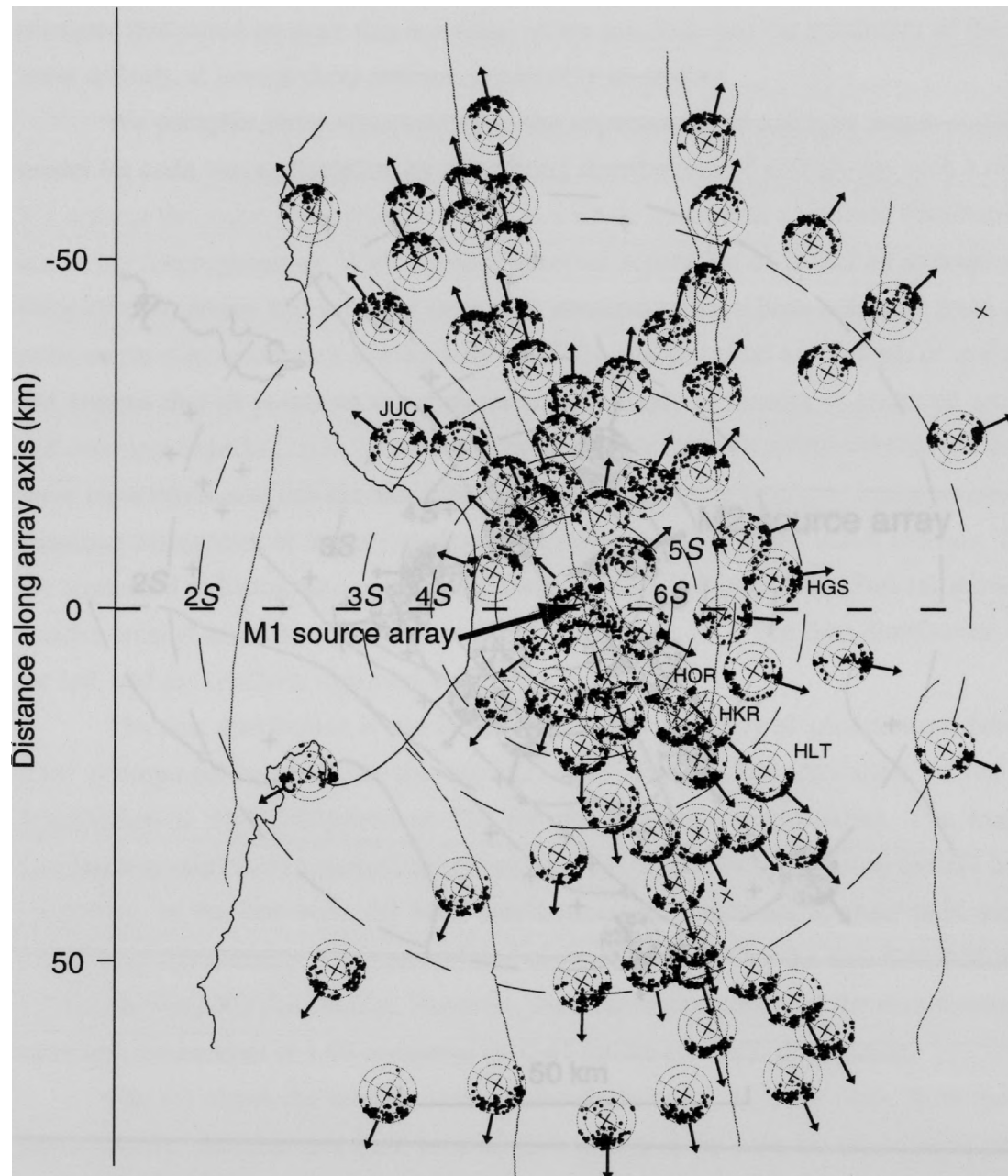
Figure 4.12 (a). Summary of M1 array analysis results at all stations. The map is oriented so that the source array axis is vertical (North is rotated 30° clockwise.) The concentric circles are equal area nets for both upper and lower hemispheres, and are located at the station positions. The dots inside each net are the projections of the scattering directions. The arrows show the direction of the direct arrival. The vertical scale at the left side of the plot shows the distance from the source array measured along the source array axis. The concentric circles marked 2S through 6S indicate the maximum extent of coda analyzed for stations within each circle.
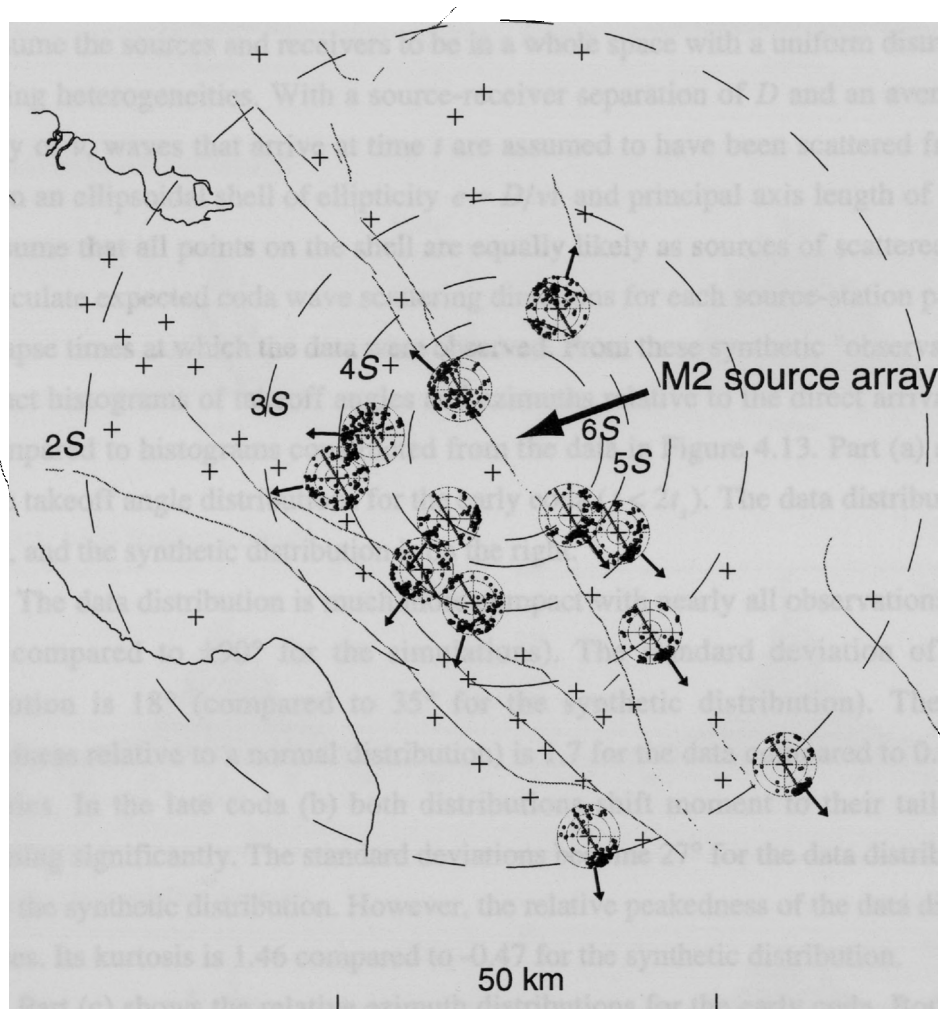
Figure 4.12 (b). Array analysis results from the M2 source array. (a) Map view of the scattering distributions. These are equal area projections of the arrivals for all time windows on combined upper- and lower-hemisphere plots. Each plot is centered on its station, and an arrow points in the direction of the direct arrival at that station. The concentric circles marked 2S through 6S indicate the maximum extent of coda analyzed for stations within each circle.

before waves leaving the source directly toward the station. There is no plausible velocity structure that could produce this behavior, so we conclude that the symmetry of the coda wave arrivals, at least at these stations, is probably an artifact.

We compare these observations to the expectations of a simple single-scattering model for coda wave generation by calculating distributions of arrivals for such a model. We assume the sources and receivers to be in a whole space with a uniform distribution of scattering heterogeneities. With a source-receiver separation of D and an average wave velocity of v, waves that arrive at time t are assumed to have been scattered from some point on an ellipsoidal shell of ellipticity $e = D/vt$ and principal axis length of $a = vt/2$. We assume that all points on the shell are equally likely as sources of scattered arrivals, and calculate expected coda wave scattering directions for each source-station pair for the same lapse times at which the data were observed. From these synthetic "observations" we construct histograms of takeoff angles and azimuths relative to the direct arrivals. These are compared to histograms constructed from the data in Figure 4.13. Part (a) shows the relative takeoff angle distributions for the early coda ($t < 2t_s$). The data distribution is on the left, and the synthetic distribution is on the right.

The data distribution is much more compact with nearly all observations between ±50° (compared to ±90° for the simulations). The standard deviation of the data distribution is 18° (compared to 35° for the synthetic distribution). The kurtosis (peakedness relative to a normal distribution) is 1.7 for the data compared to 0.03 for the synthetics. In the late coda (b) both distributions shift moment to their tails without broadening significantly. The standard deviations become 27° for the data distribution and 42° for the synthetic distribution. However, the relative peakedness of the data distribution increases. Its kurtosis is 1.46 compared to -0.47 for the synthetic distribution.

Part (c) shows the relative azimuth distributions for the early coda. Both the data and synthetic distributions have broader tails than was the case for the relative takeoff distributions. The standard deviation of the data distribution is 56° (compared to 64° for the synthetic distribution). The peakedness of the distributions is similar (kurtosis of the data is 1.1 compared to 0.97 for the synthetics). In the late coda, the azimuth distributions become even more similar with standard deviations of 81° for the data and 89° for the synthetics. The kurtosis of the late coda azimuth distribution is -0.6 (compared to -0.8 for the synthetics).

a) Early coda relative takeoff

b) Late coda relative takeoff

c) Early coda relative azimuth

d) Late coda relative azimuth
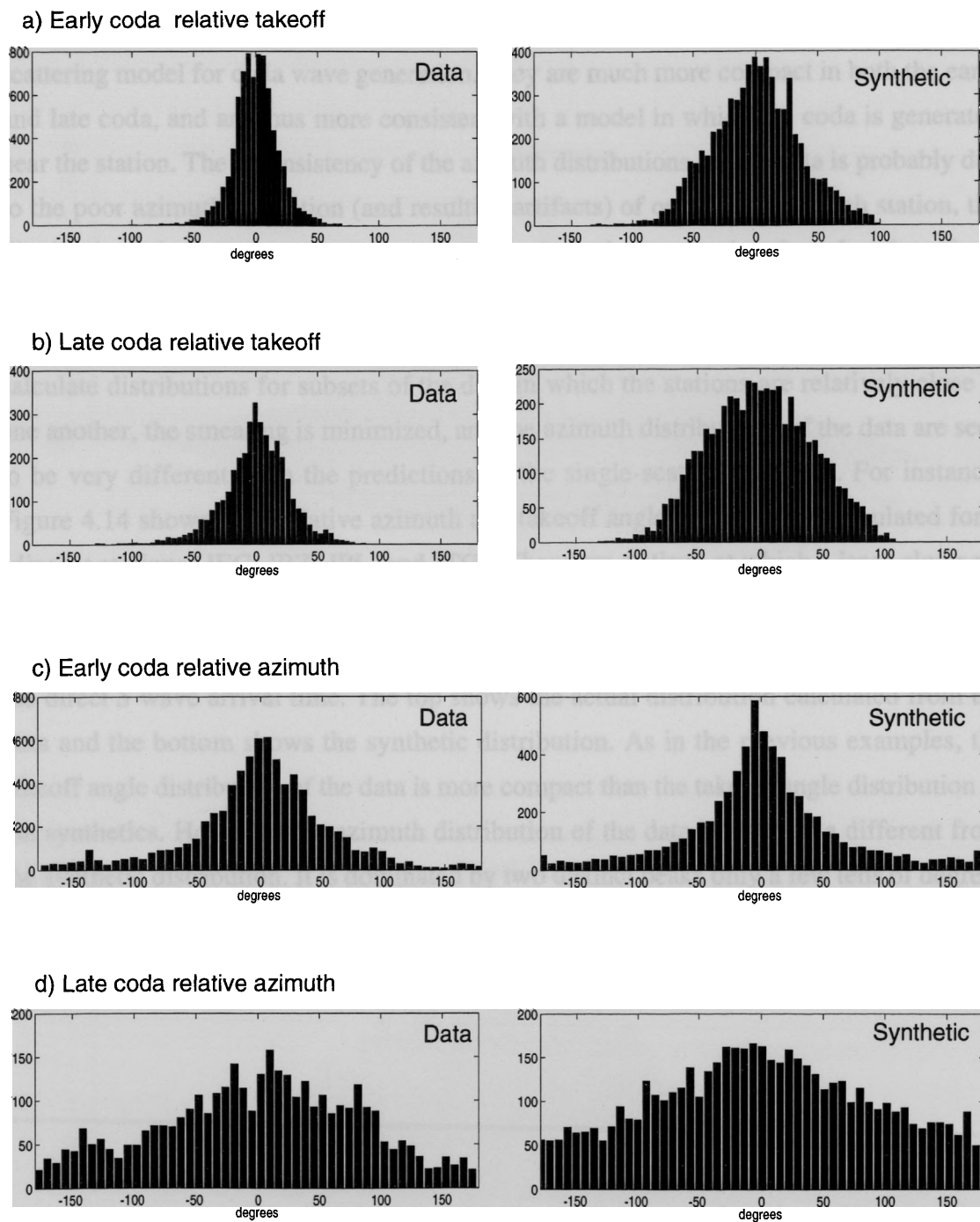
Figure 4.13. Comparison of simulated coda wave distributions to observed distributions for M1 and M2 source arrays. The histograms on the left are from the data and those on the right are from the simulations. (a) Early coda relative takeoff angle distributions. (b) Late coda relative takeoff angle distributions. (c) Early coda relative azimuth distributions. (d) Late coda relative azimuth distributions.

The takeoff angle distributions are inconsistent with the predictions of the single-scattering model for coda wave generation. They are much more compact in both the early and late coda, and are thus more consistent with a model in which the coda is generated near the station. The inconsistency of the azimuth distributions for the data is probably due to the poor azimuth resolution (and resulting artifacts) of our arrays. At each station, the distribution of azimuths tends to be symmetric about the array azimuth, rather than about the azimuth of the direct arrival. Therefore, when all the observations are combined into a distribution of azimuths relative to the direct arrivals, there is a smearing effect. When we calculate distributions for subsets of the data in which the stations are relatively close to one another, the smearing is minimized, and the azimuth distributions of the data are seen to be very different from the predictions of the single-scattering model. For instance, Figure 4.14 shows joint relative azimuth and takeoff angle distributions calculated for 4 adjacent stations (JEC, JBZ, JPL, and JTG). These are stations at which a large slowness anomaly was observed by *Ellsworth et al.* [*1992*]. The distributions are calculated for lapse times beginning with the direct *P* wave arrival time and continuing to about 4 times the direct *S* wave arrival time. The top shows the actual distribution calculated from the data and the bottom shows the synthetic distribution. As in the previous examples, the takeoff angle distribution of the data is more compact than the takeoff angle distribution of the synthetics. However, the azimuth distribution of the data is also quite different from the synthetic distribution. It is dominated by two distinct peaks only a few tens of degrees in width. By comparison, the azimuth distribution of the synthetics is nearly uniform. Clearly, at these 4 stations, the single-scattering model is not appropriate.
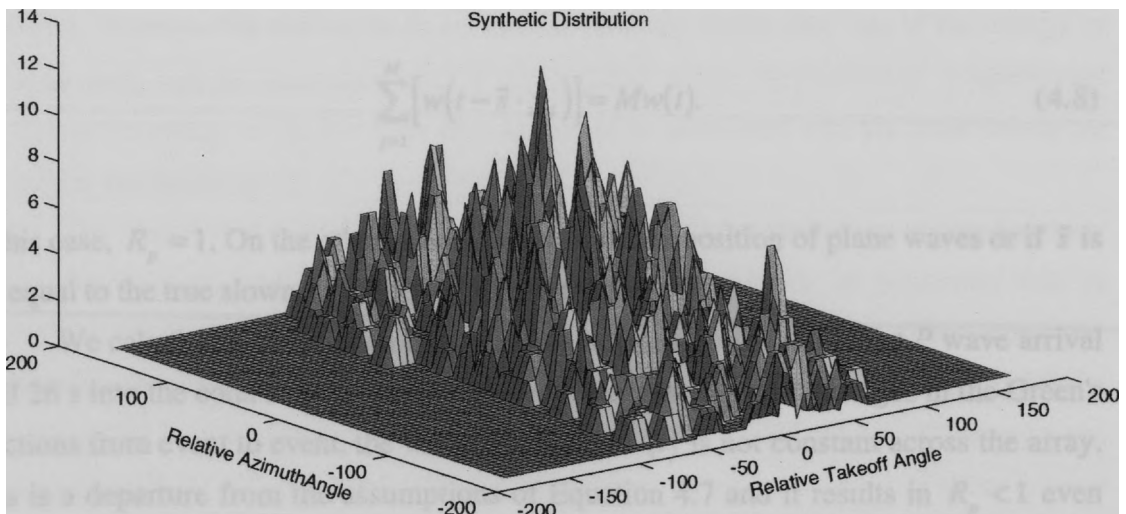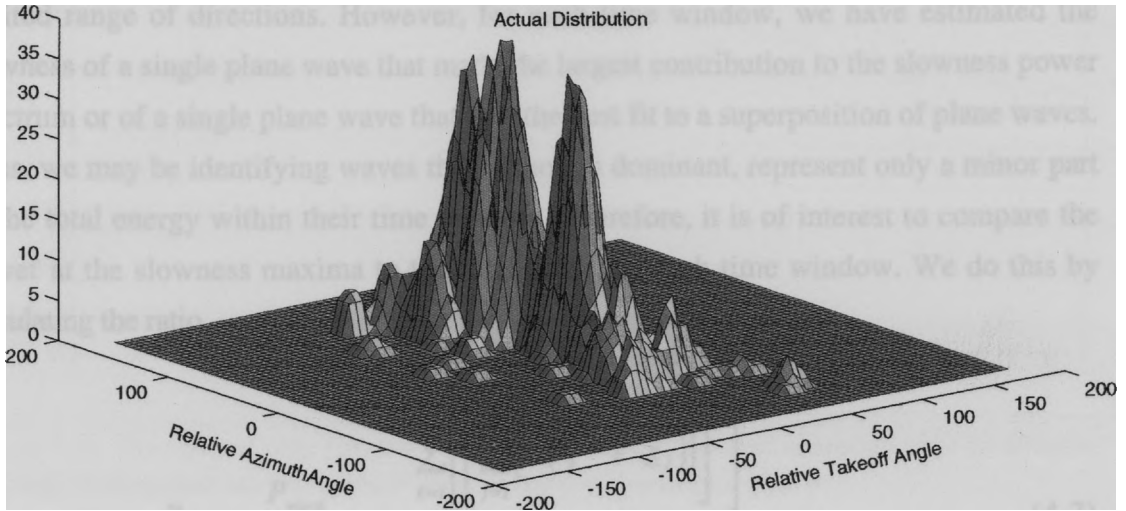
Figure 4.14. Comparison of actual to simulated distributions for entire coda at stations JEC, JBZ, JPL, and JTG. (top) joint distribution of relative azimuth and relative takeoff angles measured at the stations. (bottom) the joint distributions produced by modeling the coda waves.

Discussion of array analysis results

The results just presented indicate that a large fraction of both the early and late coda observed at most stations consists of waves that left the source region in a very limited range of directions. However, for each time window, we have estimated the slowness of a single plane wave that made the largest contribution to the slowness power spectrum or of a single plane wave that was the best fit to a superposition of plane waves. Thus, we may be identifying waves that, although dominant, represent only a minor part of the total energy within their time window. Therefore, it is of interest to compare the power at the slowness maxima to the total power in each time window. We do this by calculating the ratio

$$R_p = \frac{P_{stack}}{M^2 P_{element}} = \frac{\sum_{k=i}^{m}\left[\left[\sum_{j=1}^{M}\left[w\left(t_k - \tilde{s}\cdot\underline{x}_j\right)\right]\right]^2\right]}{M^2\sum_{k=i}^{m}\left[w^2\left(t_k\right)\right]} \ . \tag{4.7}$$

Here, $w(t)$ is the waveform, $\tilde{s}$ is the slowness used to compute the stack, $\underline{x}_j$ is the position of the jth element of the array, and M is the number of elements in the array. If $w(t)$ consists of only a single plane wave with slowness $\tilde{s}$, then

$$\sum_{j=1}^{M}\left[w\left(t - \tilde{s}\cdot\underline{x}_j\right)\right] = Mw(t). \tag{4.8}$$

In this case, $R_p = 1$. On the other hand, if $w(t)$ is a superposition of plane waves or if $\tilde{s}$ is not equal to the true slowness of the wavefield, then $R_p < 1$.

We calculated R_p for each time window beginning with the direct P wave arrival until 26 s into the coda at each station analyzed. Because of small changes in the Green's functions from event to event, the waveform shape $w(t)$ is not constant across the array. This is a departure from the assumptions of Equation 4.7 and it results in $R_p < 1$ even where the wavefield is most coherent (around the direct P arrival). In fact, the average value of R_p at the direct P arrival was 0.8. We averaged R_p across the stations and normalized the resulting time series, $\overline{R}_P(t)$, so that $\overline{R}_P(0) = 1$. This is shown plotted in Figure 4.15.
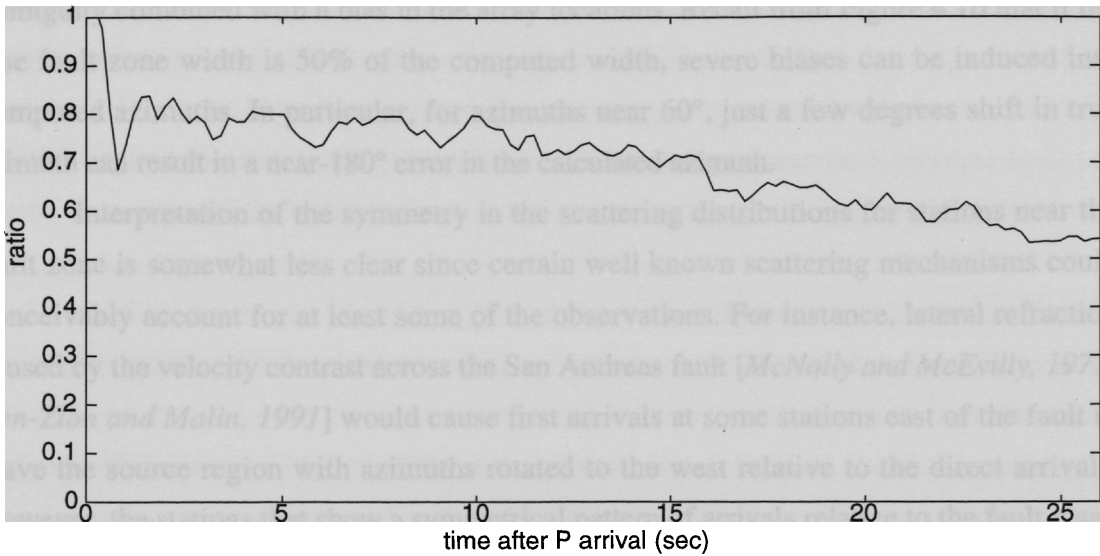
Figure 4.15. Normalized ratio between stack power and total power averaged over all stations. The ratio is computed starting at the P wave arrival (t = 0) until 26 s after P.

$\overline{R}_P(t)$ is relatively constant in the early coda. Although it drops to about 0.8 almost immediately after the direct P wave arrival, by 15 s it has only decayed to about 0.7, a decay of about 13%. By 26 s $\overline{R}_P(t)$ has decayed to about 0.55 (about 68% of its value in the early coda). Some of the decrease in $\overline{R}_P(t)$ with time may be due to the decrease in *snr* with time; however, the decline in $\overline{R}_P(t)$ almost certainly shows that less of the energy in the later coda can be associated with a single plane wave. Nevertheless, a significant fraction of the energy in the late coda does appear to be associated with the plane waves we identify in our analysis.

The remarkable degree of symmetry with respect to the fault plane shown by many of the distributions suggests that either the fault zones played an important role in controlling the scattering process or that much of the symmetry is an artifact. For some stations this second conclusion is almost certainly correct. For instance, at station HGS the first second of P and its coda have computed azimuths near 238°, about 187° away from the true azimuth of 47°. It is hard to imagine a velocity structure that would allow a wave leaving the source in the opposite direction to the receiver to be the first arrival. Moreover, if such a structure does exist, then stations near HGS should see similar arrivals. Yet, station HSP (about 3 km from HGS) has only arrivals near its true azimuth for the first 10 seconds of the events. A much more likely explanation for this behavior is aperture

ambiguity combined with a bias in the array locations. Recall from Figure 4.10 that if the true fault zone width is 50% of the computed width, severe biases can be induced into computed azimuths. In particular, for azimuths near 60°, just a few degrees shift in true azimuth can result in a near-180° error in the calculated azimuth.

Interpretation of the symmetry in the scattering distributions for stations near the fault zone is somewhat less clear since certain well known scattering mechanisms could conceivably account for at least some of the observations. For instance, lateral refraction caused by the velocity contrast across the San Andreas fault [*McNally and McEvilly, 1977; Ben-Zion and Malin, 1991*] would cause first arrivals at some stations east of the fault to leave the source region with azimuths rotated to the west relative to the direct arrivals. However, the stations that show a symmetrical pattern of arrivals relative to the fault plane are as numerous on the west side of the fault as on the east side. Also, although the arrival directions are clustered, there is no corresponding clustering in time. That is the rotated arrivals appear at random intervals throughout the coda of the affected seismograms. Fault zone guided waves [*Li et al., 1990; 1994*] could conceivably produce some of the observations. However, such waves have only been observed at distances of less than three fault zone widths from the source and at distances less than 500 m from the fault trace [*Li et al., 1994*], whereas the stations showing symmetric arrival patterns are located at distances up to about 70 km from the source and over 10 km from the fault trace.

It is much easier to explain the shape of the near-fault scattering distributions as a product of the relatively poor azimuth resolution of the source arrays for azimuths near the array azimuths and of bias in the array locations. The simulation results presented in Figure 4.9 show that timing errors corresponding to the uncertainty in the source locations of the array events can induce errors in azimuth of up to ±34° for the M1 array and up to ±15° at M2. This alone can account for most of the range of arrivals calculated for the near-fault stations. Also, the bias calculations presented in Figure 4.10 and the simulations presented in Figure 4.13 (c) show that even near the array azimuth, relatively small shifts in true azimuth could cause shifts of up to 50° in the recovered azimuth.

Where there are multiple clusters, their azimuths are usually within 45° of the direct arrivals. So, even if they are not artifacts of the array analysis, the travel paths for those arrivals are likely to be substantially similar to the paths of the direct arrivals. Thus, to achieve the necessary delays they must have been scattered near the stations at which they were recorded. This result is in general, consistent with the findings of other studies of the

seismic coda. For instance, *Phillips and Aki* [*1986*] studied site amplification using coda waves, and concluded that at many of the central California Calnet stations, much of the coda was likely to have been caused by near-site resonances. *Spudich and Bostwick* [*1987*] applied the source array technique to three stations near the Calaveras fault and found that most of the early coda at those stations was dominated by waves scattered within 2 km of each station. They were not able to analyze the late coda because of *snr* problems. *Scherbaum et al.* [*1991*] applied the source array technique to two earthquake clusters in northern Switzerland recorded at 7 stations from 10 to 63 km from the sources. They found that the early coda was dominated by waves with slowness near the direct arrivals. *Blakeslee and Malin* [*1990*] analyzed coda waves from 21 Parkfield earthquakes using a surface seismometer and matched borehole seismometer. They concluded that the coda could be best modeled as a sum of waves scattered in the deep lithosphere and scattered near the receiver.

What is surprising about the results of this study is the apparent uniformity of the scattering behavior at so many stations and over so much of the coda. *Phillips and Aki* [*1986*] found very significant differences in site amplification among many of the same stations analyzed here. They found, for instance that in the 1.5 Hz band the Hollister stations, HOR, HFH, HKR, and HPH had amplifications 20 times greater than the Gabilan stations BSR, BJC, BSG, BPC. If amplification is a direct function of site resonance, and if the apparent near-station scattering seen in these results is produced by site resonance, then we would expect to see a much greater degree of scattering at the Gabilan stations than at the Hollister stations. Yet, at both sets of stations we find the coda waves to be tightly clustered around or near the direct arrivals. At least part of the difference in results may be due to the length of coda analyzed (up to 100 s versus 26 s) and to differences in the frequency bands. The spatial distribution of site amplification in the 12 Hz band determined by *Phillips and Aki* [*1986*] was quite different from that of the 1.5 Hz band. Since our analysis includes frequencies from 1 to 6 Hz, we may average out such frequency-dependent behavior.

Scherbaum et al. [*1991*] found that at large lapse times, the diversity of scattering increased substantially relative to scattering in the early coda. One explanation for the difference between our results and theirs (for the late coda) may be that mechanisms of coda wave generation are strongly dependent on local tectonics. Another possibility is that at large lapse times their results were affected by noise in the seismograms. Their arrays

had 12 and 16 events respectively compared to 70 and 31 events in our two source arrays. This means that our array gains were several times higher, resulting in improved noise suppression. Also, the seismograms they analyzed appear to have had poor *snr* relative to the seismograms from our M1 cluster. (Compare our Figure 4.4 to their Figures 10, 12, and 14.) In this context, it is interesting to note that *Got and Coutant* [1996] obtained results similar to ours using a source array of 71 multiplet earthquakes beneath Kilauea volcano. They analyzed coda wave slowness for lapse time to $4S$ at 9 stations within 20 km of the source array and found that although the late coda slowness was not necessarily the same as the direct wave slowness, the arrivals were tightly focused.

Blakeslee and Malin [*1990*] found significant differences between coda waves recorded by a surface seismometer and a matched seismometer in a 200 m borehole. They concluded that the early coda was dominated by near-surface scattering and the late coda was dominated by volume-scattered waves. By contrast, our results indicate that the late coda is still dominated by near surface scattering. Probably the major contributor to the difference between our conclusions is that we analyze waves with frequencies from 1 to 6 Hz. At these frequencies, the wavelengths are from 3 to 18 times the depth of the borehole, so that both seismometers are effectively at the free surface.

4.6 Stress induced velocity changes

Ellsworth et al. [*1992*] analyzed 21 multiplet earthquakes that occurred on the Calaveras and San Andreas faults near the Loma Prieta mainshock and that spanned the occurrence of the mainshock temporally. The authors identified path-averaged coseismic velocity changes of up to 0.8% on source-receiver paths traversing the aftershock zone, and in every case, the velocity was lower after the mainshock. However, their analysis provides no information on where the slowness change occurred. The change could be a near-surface phenomenon, confined to the fault zone, or distributed throughout a large volume of the crust. The phase shifts between seismograms on which the velocity change is based occurred in the early S coda within a few seconds of the S wave arrival. The analysis of the previous section shows that at nearly all stations the early S coda consists of waves that left the source at azimuths close to the azimuth of the direct arrival. This is true for stations both inside and outside the fault zone and implies that most of the early coda for stations in this region is generated by scattering near the station. This would imply a change in effective moduli of the near-surface rock under the affected stations. The

change in moduli could be caused by crack opening or extension either from the change in stress due to the earthquake or from strong shaking associated with the earthquake.

In the case of the Loma Prieta earthquake we have some constraints on the stress change from extended-source models of the earthquake. If the observed slowness changes are due to stress changes from the mainshock then the spatial distribution of modeled velocity changes should correspond to the spatial distribution of observed coseismic slowness changes. If, on the other hand, the observed slowness changes are due to strong shaking there is little reason to expect agreement between the observed and modeled distributions. We only model velocity changes due to change in mean stress, or equivalently, change in pressure since the shear wave velocity change is likely to be dominated by the effects of pressure change [*Mavko, et al., 1995*]. The pressure change is mapped into a velocity change using the empirical relation between effective pressure and shear wave velocity of *Jones* [*1983*].

4.6.1 Calculation of Velocity Changes

The *Beroza* [*1991*] slip model is based on a planar fault surface that strikes N 50° W and dips 70° to the SW. The model has a total horizontal extent of 40 kilometers, and extends in depth from about 6 kilometers to 20 kilometers. There are two areas of high slip in the model. The first area is centered 7 kilometers northwest of the epicenter at a depth of 14 kilometers, and the second is centered 6 kilometers to the southeast of the epicenter at a depth of 12 kilometers. Slip in both regions exceeded 4.5 meters; however, slip in the southern region is predominantly right-lateral strike-slip, and slip in the northern region is predominantly reverse dip-slip. The slip model is divided into 272 rectangles two kilometers in height and one kilometer in width. We used the DIS3D program [*Erickson, 1987*] to compute the stress changes from the slip model at 5 km intervals on a grid extending 100 kilometers east and west of the mainshock hypocenter , and 2 kilometers in depth.

It is well known that seismic velocities in crustal rocks depend on the applied stress [*Walsh, 1965; Nur, 1971; Mavko and Nur, 1978*]. This dependence is attributed to closing of compliant parts of the pore volume with increasing stress. Because the effective modulus of a rock is a function of the relative proportions of pore volume and solid matrix, reducing the pore volume increases the effective modulus and thus, the velocity. The relation between stress change and velocity change is a function of rock type (because

of inherent differences in pore volume) and of confining stress (because cracks become less compliant as they close). Laboratory experiments have established empirical relations between confining pressure and seismic velocity for numerous rock types. In this study, we use a relation established for Sierra White granite by *Jones* [*1983*]. This relation is shown in Figure 4.17. It is based on laboratory measurements of shear wave velocity in Sierra white granite at 15 pressures ranging from about 1 MPa to 80 MPa. The

Velocity - Pressure Relation (Jones, 1983)

Effective Pressure (MPa)
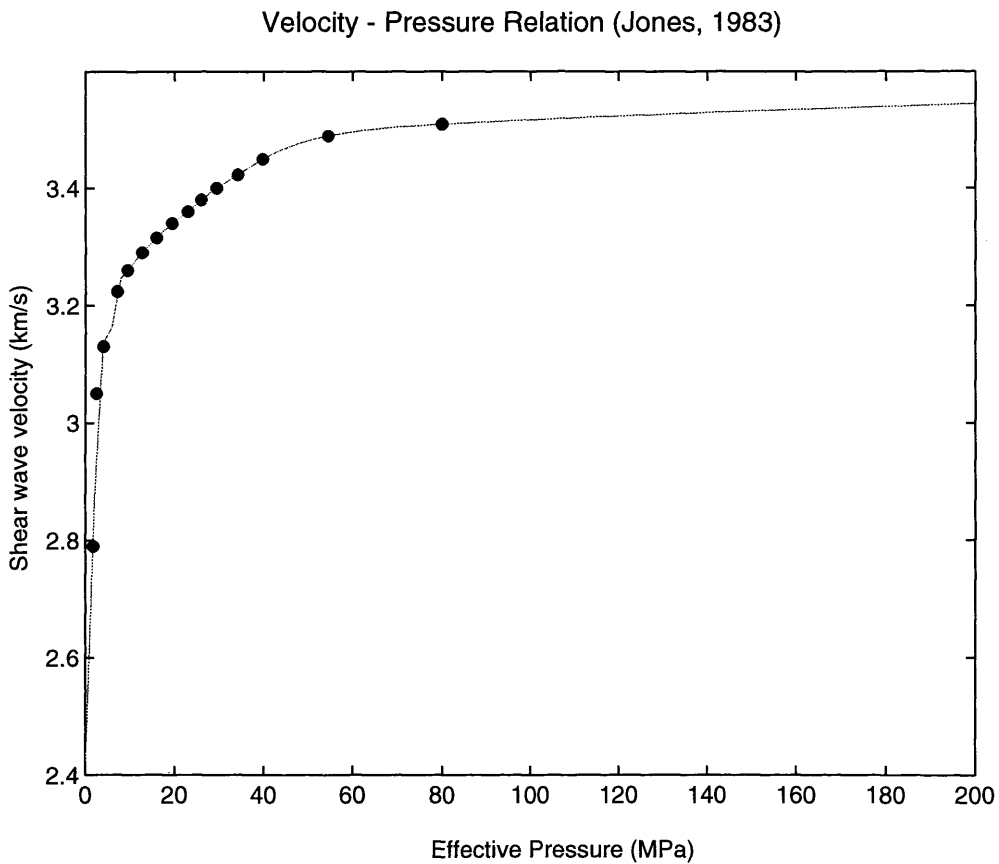
Figure 4.16 Shear wave velocity as a function of effective pressure. This is an adaptation of the relation determined by *Jones* [*1983*]. A datum has been added at P = 0 in order to constrain the cubic spline for use at very low pressures.

velocity change resulting from a step in pressure is dependent on the depth at which the measurement is made since the confining stress increases with depth. That is, if ΔP is the change in pressure due to a change in the local stress, and if $P(z)$ is the lithostatic pressure at the depth z where the stress change occurs, then the change in velocity (ΔV) is given by

$$\Delta V = f(P + \Delta P) - f(P) \ . \tag{4.9}$$

Here $f(P)$ is the relation between pressure and shear wave velocity given shown in Figure 4.17.

In the study region, the San Andreas fault is bounded on the east by Franciscan sedimentary rocks, and on the west by either Salinian (granitic) or sedimentary rocks. Thus, the relation of Figure 4.17 is only approximate for the entire region. For this reason, we do not attempt to relate the amplitudes of the observed velocity changes to the amplitudes of the theoretical changes. We only attempt to determine if the spatial variations are consistent. We assume that the rock properties are sufficiently homogeneous on a regional scale that the locations of the maximum velocity change will roughly correspond with the observed variations if the slowness changes are actually due to stress changes.

4.6.2 Results of the Velocity Modeling

The results of the velocity change modeling are shown in Figure 4.17. (b), which is a close-up of the epicentral region and is scaled the same as the *Ellsworth et al.* [*1992*] slowness change map reproduced in (a). The large velocity changes from the mainshock are concentrated within a radius of about 20 km from the mainshock epicenter and range in magnitude up to 0.1 km/s. Velocities increase to the NE of the Zayante fault and decrease to the SW. The pattern of the velocity change persists to at least 2 km depth. However, the magnitude of the velocity changes decreases rapidly with depth.

The observed slowness changes reported by *Ellsworth et al.* [*1992*] were based on analysis of 21 multiplets which spanned the Loma Prieta earthquake temporally. For each event-pair a moving-window cross spectral analysis [*Poupinet et al.* , *1983*] was applied to the seismogram codas to determine signal delay as a function of time. Under the assumption of uniform velocity change throughout the volume traversed by the coda waves, the fractional delay ($\Delta T / T$) is equal to the minus fractional velocity change ($\Delta V / V$). Their result is reproduced in Figure 4.17 (a). The map contours 421 slowness change estimates for the 21 multiplets at the CALNET stations shown on the map. Most stations have more than one observation. Consequently, the datum used at each station is the average of the individual slowness change estimates. The maximum slowness change for these observations occurs near stations JRG, JEC, JTG, JBZ, and JPL and is near 5 parts per 1000. This corresponds to a decrease in velocity. The peak of the slowness

(a) Coseismic slowness change in parts per 1000

(b) Predicted velocity decrease

Figure 4.17 Predicted velocity changes at a depth of 0.1 km with comparison to the *Ellsworth et al.* [*1992*] results. (a) Coseismic velocity change in parts per 1000 from the *Ellsworth et al.* [*1992*] study.(b) Map of velocity changes at a depth of 0.1 km. Scale is from -0.1 to +0.1 km/s.

increase is at station JEC, which is located on the San Andreas fault about 15 km south of its intersection with the Sargent fault. By contrast the region of maximum velocity decrease from the stress change modeling is to the SW of the Zayante fault and the region of velocity increase from the modeling overlaps most of the region where velocity decreased in the *Ellsworth et al.* [*1992*] study. The *Ellsworth et al.* [*1992*] results also show a region of moderate slowness increase around stations HAZ, HOR, HBT, HFH, HSF, and HPH. This is nearly the region that produced the maximum slowness increase in the [*Poupinet et al., 1983*] study of the of the Coyote Lake earthquake and is far from any place where the static stress modeling predicts a decrease in velocity.

It appears that the measured coseismic velocity change is due to something other than the mean stress change from the mainshock The observed slowness increase (velocity decrease) is located in a region predicted by the modeling to have a velocity increase, and there is only a minor slowness increase southwest of the Zayante fault where the static stress modeling predicts a major decrease in velocity. An alternative explanation for the velocity change is cracking of near surface rock by strong shaking during the earthquake. This is consistent with the fact that the region of greatest velocity change is approximately coincident with the mainshock rupture. The coincidence of the southern slowness increase zone with the *Poupinet et al.* [*1983*] slowness increase zone is difficult to explain if the slowness change is due to static stress redistribution, since that zone is in a compressional quadrant for Loma Prieta and in a dilatational quadrant for Coyote Lake. However, if both regions are prone to high accelerations because of site effects, then they might be expected to behave similarly.

4.7 Summary

We have used the source array technique of *Spudich and Bostwick* [*1987*] to analyze coda waves recorded at up to 78 central California Calnet stations using a source array of 70 events located on the San Andreas fault south of the 1989 Loma Prieta rupture (M1) and a source array of 31 events located on the Calaveras fault in the aftershock zone of the 1984 Morgan Hill earthquake (M2). The interpretation is complicated by the fact that both arrays are nearly planar since each is located at depth on a well developed fault. This introduces strong azimuth dependencies in the array sensitivity. At nearly every station, arrivals throughout the coda were found to be strongly clustered in azimuth and takeoff angle. At most stations there were several clusters symmetrically disposed about the array

planes. The multiplicity of the clusters is likely to be an artifact resulting from the limited resolution of the arrays, so that at most stations nearly all the arrivals are, in fact, clustered near the direct arrival. Even if this is not the case, most clusters to the NW and SE of the arrays are centered within about ±45°of the direct arrival, consistent with strong forward scattering. These results suggest that at nearly all of the stations analyzed, the first 26 s of coda consists primarily of waves that were scattered near the stations rather than throughout a volume of the lithosphere that grows with lapse time. This result holds even at stations very close to the source (at least for the M1 cluster) where the amount of coda examined amounts to about 6 times the direct S travel time. In other words, for at least some of the stations, even in the late coda a large fraction of the energy is from waves scattered near the station.

We use these results in combination with static stress modeling to examine the source of coseismic velocity decreases from the 1989 Loma Prieta earthquake [*Ellsworth et al., 1992*]. These velocity changes were observed in the early *S* coda of multiplet earthquakes that spanned the Loma Prieta mainshock temporally, and the largest such change was observed at station JEC using earthquakes from the M1 cluster. Results from the slowness analysis show that the coda at JEC has slowness almost identical to the direct arrival to at least $2t_s$ JEC is in the fault zone, so it is possible that the early coda at JEC is generated by trapped waves. However, coda at nearby stations JTG, JBZ, JPL, and JEL (which are well outside the fault zone) also consist of waves with slowness near the direct arrival. The simplest explanation for these observations is that most of the early coda for stations in this region is generated by scattering near the station. If so, then the velocity change observed by *Ellsworth et al.* [*1992*] must be due to changes in the shear wave modulus of the near-station crust. The velocity change field from the modeling has its maximum increase between the Zayante and San Andreas faults, and its maximum decrease to the SW of the Zayante fault. In contrast, the *Ellsworth et al.* [*1992*] results place the maximum velocity decrease to the NE of the Zayante fault--almost on top of the region of velocity increase from the modeling. This region is almost directly above a high-slip part of the *Beroza* [*1991*] model, and would have been likely to experience high accelerations during the mainshock. Therefore, we conclude that the observed coseismic velocity decrease was probably caused by crack opening due to strong shaking from the mainshock.

References

Abercrombie, R., and J. Mori, Foreshock occurrence as a function of mainshock depth and mechanism, *Seismo. Res. Lett.*, *66*, 23, 1995.

Abercrombie, R., and J. Mori, Local observations of the onset of a large earthquake: 28 June 1992 Landers, California, *Bull. Seismol. Soc. Am.*, *84*, 725-734, 1994.

Abercrombie, R., D.C. Agnew, and F.K. Wyatt, Testing a model of earthquake nucleation, *Bull. Seismol. Soc. Am.*, *85*, 1873-1878, 1995.

Aki, K., and W. H. K. Lee, Determination of three-dimensional velocity anomalies under a seismic array using P arrival times from local earthquakes, 1. A homogeneous initial model, *J. Geophys. Res.*, *81*, 4381-4399, 1976.

Aki,. K., and B. Chouet, Origin of coda waves: source, attenuation and scattering effect, *J. Geophys. Res.*, *80*, 3322-3342, 1975.

Bakun, W.H., R.M. Stewart, C.G. Bufe, and S.M. Marks, Implication of seismicity for failure of a section of the San Andreas fault, *Bull. Seismol. Soc. Am.*, *70*, 1185-201, 1980.

Behr, J., R. Bilham, P. Bodin, and S. Gross, Eureka Peak fault afterslip following the 28 June 1992 Landers earthquake, *Bull. Seismol. Soc. Am.*, *84*, 826-834, 1994.

Ben-Zion, Y. and P. Malin, San Andreas fault zone head waves near Parkfield, California, *Science*, *251*, 1592-1594, 1991.

Beroza, G. C. Near-source modeling of the Loma Prieta earthquake: evidence for heterogeneous slip and implications for earthquake hazard. *Bulletin of the Seismological Society of America*, *81*, 1603. 1991

Beroza, G.C., and M.D. Zoback, Mechanism diversity of the Loma Prieta aftershocks and the mechanics of mainshock-aftershock interaction, *Science, 259*, 210-213, 1993.

Beroza, G. C., Cole, A. T., and W. L. Ellsworth, Stability of coda wave attenuation during the Loma Prieta, California, earthquake sequence, *J. Geophys. Res.*, *100*, 3977-3987, 1995.

Blakeslee, S. N., and P. E. Malin, A comparison of earthquake coda waves at surface versus subsurface seismometers, *J. Geophys. Res.*, *95*, 309-325, 1990.

Boatwright, J., A spectral theory for circular seismic sources: Simple estimates of source dimension, dynamic stress drops, and radiated energy, *Bull. Seismol. Soc. Am.*, *70*, 1-28,1980.

Bodri, B., and S. Iizuka, On the correlation between earth tides and microseismic activity, *Phys. Earth Planet. Inter.*, *55*, 126-134, 1989.

Bortugno, E.J., Map showing recency of faulting, San Bernardino quadrangle, California, scale 1:250,000, regional geologic map series, Div. of Mines and Geol., Sacramento, Calif., 1986.

Bouchon, M. A complete synthesis of seismic crustal phases at regional distances, *J. Geophys. Res.*, *87*, 1735-1742, 1982.

Brune, J. N., Tectonic stress and the spectra of seismic shear waves from earthquakes, *J. Geophys. Res.*, *75*, 4997-5009, 1970.

Buland, R., The mechanics of locating earthquakes, *Bull. Seismol. Soc. Am.*, *66*, 173-187,1976.

Chouet, B., Temporal variation in the attenuation of earthquake coda near stone canyon, California, *Geophys. Res. Lett., 6*, 143-146, 1979.

Cohee, B. P. and G. C. Beroza, Slip distribution of the 1992 Landers earthquake and its implications for earthquake source mechanics, *Bull. Seismol. Soc. Am., 84*, 692-712, 1994.

Das, S. and C. Scholz, Off-fault aftershock clusters caused by shear stress increase? *Bull. Seismol. Soc. Am. 71*, 1669-1675, 1982.

Das, S., and C. Scholz, Theory of time-dependent rupture in the Earth, *J. Geophys. Res., 86*, 6039-6051, 1981.

Deichmann, N. and M. Garcia-Fernandez, Rupture geometry from high-precision relative hypocentre locations of microearthquake ruptures, *Geophys. J. Int., 110*, 501-517, 1992.

Deichmann, N. Empirical Green's functions: a comparison between pulse width measurements and deconvolution by spectral division. Submitted to *Bulletin of the Seismological Society of America*, 1995.

Dieterich, J.H., A model for the nucleation of earthquake slip, in *Earthquake Source Mechanics, Geophys. Monogr. Ser.*, vol. 37, edited by S. Das, J. Boatwright, and C.H. Scholz, pp. 37-47, AGU, Washington, D.C., 1986.

Dieterich, J.H., Earthquake nucleation on faults with rate- and state-dependent strength, *Tectonophysics, 211*, 115-134, 1992.

Dieterich, J.H., Time-dependent friction and the mechanics of stick-slip. *Pure Appl. Geophys., 116*, 790-806, 1978.

Dietz, L. D. and W. L. Ellsworth, The October 17, 1989 Loma Prieta, California, earthquake and its aftershocks: Geometry of the sequence from high-resolution locations, *Geophys. Res. Lett., 17*, 1215-1218, 1990.

Dodge, D. A., G.C. Beroza, and W.L. Ellsworth, Evolution of the 1992 Landers, California, foreshock sequence and its implications for earthquake nucleation, *J. Geophys. Res., 100*, 9865-9880, 1995.

Dodge, D. A., G.C. Beroza, W.L. Ellsworth, and A.T. Cole, Array analysis of micro-earthquakes to determine the cause of velocity changes associated with the 1989 Loma Prieta earthquake, *Seismol. Res. Lett., 64*, 33, 1993.

Dodge, D. A., and K.F. Sprenke, Improvements in mining induced microseismic source locations at the Lucky Friday mine using an automated whole-waveform analysis system, *Pageoph, 139*, 609-626, 1992.

Douglas, A., Joint epicentre determination, *Nature, 215*, 47-48, 1967.

Ellis, J. R., and A. Lindh, Linearity of VCO-discriminator playback system with respect to zero crossing times, *U.S. Geol. Surv. Open File Rep., 76-873*, 8 pp., 1976.

Ellsworth, W.L., Three-dimensional structure of the crust and mantle beneath the island of Hawaii, 327 p., Ph.D. thesis, Mass. Inst. of Technol., Cambridge, 1977.

Ellsworth, W. L., A. T. Cole, G. C. Beroza, and M. C. Verwoerd, Changes in crustal wave propagation associated with the 1989 Loma Prieta, California earthquake (abstract) *EOS Trans. AGU, 73*, 360. 1992.

Ellsworth, W. L., and G.C. Beroza, Seismic evidence for a seismic nucleation phase, *Science*, *268*, 851-855, 1995.

Ellsworth, W. L., and L. D. Dietz, Repeating earthquakes: Characteristics and implications, *USGS Open File Report, OF 90-098*, 1990.

Ellsworth, W. L., Kissling, E., and H. Maurer, Errors in traveltime tomography and robust estimation of tomographic models, *International Association of Seismology and Physics of the Earth's Interior*, 27th General Assembly Abstracts, Wellington, New Zealand, 1994.

Erickson, L., *User's Manual For DIS3D: A Three-Dimensional Dislocation Program With Applications to Faulting in the Earth*, Geomechanics, Applied Earth Science Department, Stanford University, Stanford, Calif., 1987.

Evernden, J. F., Precision of epicenters obtained by small numbers of worldwide stations, *Bull. Seismol. Soc. Am.*, *59*, 1365-1398, 1969.

Fitch, T. J., Compressional velocity in source regions of deep earthquakes: An application of the master earthquake technique, *Earth Planet. Sci. Lett.*, *26*, 156-166, 1975.

Flinn, E. A., Confidence regions and error determinations for seismic event location, *Rev. Geophys.*, *3*, 157-185, 1965.

Frankel, A. and L. Wennerberg, Energy flux model of seismic coda: separation of scattering and intrinsic attenuation, *Bull. Seismol. Soc. Am.* *77*, 1223-1251, 1987.

Frankel, A., and H. Kanamori, Determination of rupture duration and stress drop from earthquakes in southern California, Bull. *Seismol. Soc. Am. 73*, 1527-1551, 1983.

Frémont , M., and S.D. Malone, High precision relative locations of earthquakes at Mount St. Helens, Washington, *J. Geophys. Res. 92*, 10,223-10,236, 1987.

Geller, R. J., and C. S. Mueller, Four similar earthquakes in central California, *Geophysical Research Letters*, *7*, 821-824, 1980.

Gao, L. S., L. C. Lee, N. N. Biswas, and K. Aki, Comparisons of the effects between single and multiple scattering on coda waves for local earthquakes. *Bull. Seismol. Soc. Am. 73*, 337-389, 1983.

Gillard, D., A.M. Rubin and P. Okubo. Kilauea's upper east rift: a strike-slip fault atop a magma body?, *EOS Trans.* AGU, Fall Meeting Supplement, *76*, F350, 1995.

Got, J. L., and J. Fréchet Origin of amplitude variations in seismic doublets: Source or attenuation process?, *Geophys. J. Int.*, 114, 325-340, 1993.

Got, J. L., J. Fréchet, F.W. Klein, Deep fault plane geometry inferred from multiplet relative relocation beneath the south flank of Kilauea. *Journal of Geophysical Research*, *99*, 15375-15386, 1994.

Got, J. l., and O. Coutant, Composition of microearthquake coda waves: Implications for the monitoring of crustal deformation and stresses, *European Seismological Commission*, 25th General Assembly Abstracts, Reykjavík, Iceland, 1996.

Gubbins, D., *Seismology and plate tectonics*, Cambridge University Press, New York, 1990.

Gusev, A. A., and U. K. Lemzikov, Properties of scattered elastic waves in the lithosphere of Kamchatka: parameters and temporal variations, *Tectonophysics*, *112*, 137-153, 1985.

Harris, R. A., and R. W. Simpson, Changes in static stress on southern California faults after the 1992 Landers earthquake, *Nature, 360*, 251-254, 1992.

Hauksson, E., and L. M. Jones, The 1988 and 1990 Upland earthquakes: Left-lateral faulting adjacent to the central transverse ranges, *J. Geophys. Res., 96*, 8143-8165, 1991.

Hauksson, E., L. M. Jones, K. Hutton, and D. Eberhart-Phillips, The 1992 Landers earthquake sequence: Seismological observations, *J. Geophys. Res., 98*, 19,835-19,858, 1993.

Hough, S.E., Southern surface rupture associated with the M 7.3 1992 Landers, California, earthquake, *Bull. Seismol. Soc. Am. 84*, 817-825, 1994.

Iio, Y. Slow initial phase of the P-wave velocity pulse generated by microearthquakes. *Geophys. Res. Let., 19*, 477-480, 1992.

Ishida, M. and H. Kanamori, The foreshock activity of the 1971 San Fernando earthquake, California, *Bull. Seismol. Soc. Am. 68*, 1265-1279, 1978.

Jain, A. K., and R. C. Dubes, *Algorithms for clustering data*, Prentice Hall, Englewood Cliffs, NJ, 1988.

Jin, A., and K. Aki, Spatial and temporal correlation of coda Q^{-1} and seismicity and its physical mechanism., *J. Geophys. Res., 94*, 14,041-14,059, 1989.

Jin, A., and K. Aki, Temporal change in coda Q before the Tangshen earthquake of 1976 and the Haicheng earthquake of 1975, *J. Geophys. Res., 91*, 665-673, 1986.

Johnson, D. H., and D. E. Dudgeon, *Array Signal Processing*, Prentice Hall, Englewood Cliffs, NJ, 1993.

Johnston, M.J.S., A.T. Linde, and D.C. Agnew, Continuous borehole strain in the San Andreas fault zone before, during and after the 28 June 1992, Mw 7.3 Landers, California, earthquake, *Bull. Seismol. Soc. Am., 84* , 799-805, 1994.

Johnston, M.J.S., A.T. Linde, and M.T. Gladwin, Near-field high resolution strain measurements prior to the October 18, 1989, Loma Prieta Ms 7.1 earthquake, *Geophys. Res. Lett., 17*, 1777-1780, 1990.

Jones, L. M., and P. Molnar, Some characteristics of foreshocks and their possible relationship to earthquake prediction and premonitory slip on faults, *J. Geophys. Res., 84*, 3596-3608, 1979.

Jones, L. M., B. Wang, S. Xu, and T. J. Fitch, The foreshock sequence of the February 4, 1975, Haicheng earthquake ($M = 7.3$), *J. Geophys. Res., 87*, 4575-4584, 1982.

Jones, L. M., Foreshocks (1966-1980) in the San Andreas System, California. *Bull. Seismol. Soc. Am., 74*, 1361-1380, 1984.

Jones, T. D., Wave propagation in porous rock and models for crustal structure, Ph.D. thesis, Stanford University, 223 p., 1983.

Kanamori, H., and D.L. Anderson, Theoretical basis of some empirical relations in seismology, *Bull. Seismol. Soc. Am., 65*, 1073-1095, 1975.

Kanamori, H., The nature of seismicity patterns before large earthquakes, in *Earthquake Prediction: An International Review, Maurice Ewing Ser.*, vol. 4, edited by D. W. Simpson and P. G. Richards, pp. 1-19, AGU, Washington, D. C., 1981.

Keilis-Borok, V. I., On the estimation of the displacement in an earthquake source and of source dimensions, *Ann. Geofis., 12*, 205-214, 1959.

King, G. C. P., R. S. Stein, and J. Lin, Static stress changes and the triggering of earthquakes, *Bull. Seismol. Soc. Am.*, *84* , 935-954, 1994.

Lahr, J. C., Local earthquake location programs in *A course on PC-based seismic systems*, *U. S. Geol. Surv. Open File Rep.*, *OF 92-441*, edited by W. H. K. Lee, and D. A. Dodge, pp. 226-250, 1992.

Lee, W. H. K., and J. C. Lahr, HYPO71 (revised): A computer program for determining hypocenter, magnitude, and first motion pattern of local earthquakes, *U. S. Geol. Surv. Open File Rep.*, *OF 75-311*, 1-116, 1975.

Lee, W. H. K., and S. W. Stewart, *Principles and applications of microearthquake networks*, Academic Press, San Francisco, 1981.

Levander, A. R., and N. R. Hill, P-SV resonances in irregular velocity surface layers, *Bull. Seismol. Soc. Am. 75*, 847-865, 1985.

Li, Y., Aki, K., Adams, D., Hasemi, A., and W. H. K. Lee, Seismic guided waves trapped in the fault zone of the Landers, California, earthquake of 1992, *J. Geophys. Res.*, *99*, 11,705-11,722, 1994.

Li, Y., Leary, P., Aki, K., and P. Malin, Seismic trapped modes in the Oroville and San Andreas fault zones, Science, 249, 763-766, 1990.

Lindh, A., G. Fuis, and C. Mantis, Seismic amplitude measurements suggest foreshocks have different focal mechanisms than aftershocks, *Science, 201*, 56-59, 1978.

Maurer, H., and U. Kradolfer, Hypocentral parameters and velocity estimation in the western Swiss Alps by simultaneous inversion of *P*- and *S*-wave data, *Bulletin of the Seismological Society of America*, *86*, 32-42, 1996.

Mavko, G., and A. Nur, The effect of non-elliptical cracks on the compressibility of rocks, *J. Geophys. Res., 83*, 4459-4468, 1978.

Mavko, G., Mukerji, T., and N. Godfrey, Predicting stress-induced velocity anisotropy in rocks, *Geophysics, 60*, 1081-1097, 1995.

McNally, K. C., and T.V. McEvilly, Velocity contrast across the San Andreas fault in central California: Small-scale variations from *P*-wave nodal plane distortion, *Bull. Seismol. Soc. Am. 67*, 1565-1576, 1977.

Meredith, P.G., and B.K. Atkinson, Stress corrosion and acoustic emission during tensile crack propagation in Whin Sill dolerite and other basic rocks, *Geophys. J. R. Astron. Soc., 75*, 1-21, 1983.

Meremonte, M., Gomberg, J., and E. Cranswick, Constraints on the 29 June 1992 Little Skull Mountain, Nevada, earthquake sequence provided by robust hypocenter estimates, *Bulletin of the Seismological Society of America, 85*, 1039-1049, 1995.

Mogi, K., *Earthquake Prediction*, Academic, San Diego, Calif., 1985.

Mogi, K., Some discussions on aftershocks, foreshocks and earthquake swarms - The fracture of a semi-infinite body caused by inner stress origin and its relation to earthquake phenomena, 3, *Bull. Earthquake Res. Inst. Univ. Tokyo, 41*, 615-658, 1963.

Mori J., and A. Frankel, Source parameters for small events associated with the North Palm Springs, California, earthquake determined using empirical Green functions. *Bull. Seismol. Soc. Am. 80*, 278-295, 1990.

Mueller, C. S., Source pulse enhancement by deconvolution of an empirical Green's function, *Geophys. Res. Lett., 22,* 33-36, 1985.

Nakamura, Y., Relative location of moonquakes within a source region, *EOS, 59,* p 315, 1978.

Nur, A., Effects of stress on velocity anisotropy in rocks with cracks, *J. Geophys. Res., 76,* 2022-2034, 1971.

Ohnaka, M., Critical size of the nucleation zone of earthquake rupture inferred from immediate foreshock activity, *J. Phys. Earth, 41,* 45-46, 1993.

Ohnaka, M., Earthquake source nucleation: A physical model for short term precursors. *Tectonophysics, 211,* 149-178, 1992.

Okada, Y., Internal deformation due to shear and tensile faults in a half-space, *Bull. Seismol. Soc. Am., 82,* 1018-1040, 1992.

Oppenheimer, D. H., Klein, F. W., and J. P. Eaton, The first 20 years of CALNET, the Northern California seismic network, *USGS Open File Report, OF 92-0209,* 1992.

Pechmann, J.C. and H. Kanamori. Waveforms and spectra of preshocks and aftershocks of the 1979 Imperial Valley, California, earthquake: evidence for fault heterogeneity?, *Journal of Geophysical Research, 87,* 10579-10597, 1982.

Phillips, W. S., and K. Aki, Site amplification of coda waves from local earthquakes in central California, *Bull. Seismol. Soc. Am. 76,* 627-648, 1986.

Poupinet, G., W. L. Ellsworth, J. Fréchet, Monitoring velocity variations in the crust using earthquake doublets: An application to the Calaveras fault, California, *J. Geophys. Res., 89,* 5719-5731, 1984.

Press, W.H., B.P. Flannery, S.A. Teukolsky, and W.T. Vettering, *Numerical Recipes: The Art of Scientific Computing,* Cambridge Univ. Press, New York, 1986.

Reasenberg, P., and D. Oppenheimer, FPFIT, FPPLOT and FPPAGE: Fortran computer programs for calculating and displaying earthquake fault-plane solutions, *U.S. Geol. Surv. Open File Rep.,* 85-739, 109 pp., 1985.

Rice, J.R., and M.P. Cleary, Some basic stress diffusion solutions for fluid-saturated elastic porous media with compressible constituents, *Rev. Geophys., 14,* 227-241, 1976.

Roecker, S.W., Seismicity and tectonics of the Pamir-Hindu Kush region of central Asia, Ph.D. thesis, 294 p., Mass. Inst. Technol., Cambridge, 1981.

Scherbaum, F. and C. Kisslinger, Coda Q in the Adak seismic zone, *Bull. Seismol. Soc. Am. 75,* 615-619, 1985.

Scherbaum, F., Gillard, D., and N. Deichmann, Slowness power spectrum analysis of the coda composition of two microearthquake clusters in northern Switzerland, *Physics of the Earth and Planetary Interiors, 67,* 137-161, 1991.

Scholz, C.H., *The Mechanics of Earthquakes and Faulting,* Cambridge Univ. Press, New York., 1990.

Segall, P., and D. D. Pollard, Mechanics of discontinuous faults. *J. Geophys. Res., 85,* 4337-4350, 1980.

Shearer, P. M., Improving local earthquake locations using the L1-norm and waveform cross-correlation: Application to the Whittier Narrows, California, aftershock sequence, Submitted to *J. Geophys. Res.*, 1995.

Sibson, R. H., Implications of fault-valve behaviour for rupture nucleation and recurrence, *Tectonophysics*, *211*, 283-293, 1992.

Simpson, R. W., and P. A. Reasenberg, Earthquake-induced static stress changes on central California faults, in *The Loma Prieta, California, earthquake of October 17, 1989--Tectonic processes and models*, edited by R. W. Simpson, *U.S. Geol. Surv. Prof. Pap.*, *1550-F*, 1-131, 1994.

Smith, K.D., and K.F. Priestley, The foreshock sequence of the 1986 Chalfant, California, earthquake, *Bull. Seismol. Soc. Am.*, *78*, 172-187, 1988.

Spudich, P. and T. Bostwick. Studies of the seismic coda using an earthquake cluster as a deeply buried seismograph array, *Journal of Geophysical Research*, *92*, 10526-10546, 1987.

Stein, R. S., G. C. P. King, and J. Lin, Change in failure stress on the southern San Andreas fault system caused by the 1992 magnitude = 7.4 Landers earthquake, *Science*, *258*, 1328-1332, 1992.

Swanson, P. L., Estey, L. H., Boler, F. M., and S. Billington, Mining-induced microseismic event location errors: Acurracy and precision of two location systems, *Pageoph*, *139*, 375-404, 1992.

Tucker, W., Herrin, E., and H. W. Freedman, Some statistical aspects of the estimation of seismic travel times, *Bull. Seismol. Soc. Am.* *58*, 1243-1260, 1968.

VanDecar, J. C., and R. S. Crosson, Determination of teleseismic relative phase arrival times using multi-channel cross-correlation and least squares, *Bull. Seismol. Soc. Am.* *80*, 150-169, 1990.

Vidale, J. E., Ellsworth, W. L., Cole, A., and C. Marone, Variations in rupture process with recurrence interval in a repeated small earthquake, *Nature*, *368*, 624-626, 1994

Walsh, J., B., The effect of cracks on the compressibility of rock, *J. Geophys. Res.*, *70*, 381-389, 1965.

Wyss, M., and R. E. Habermann, Precursory quiescence before the August 1982 Stone Canyon, San Andreas fault, earthquakes, *Pure Appl. Geophys.*, *126*, 333-356, 1988.

Yamashita, T., and M. Ohnaka, Nucleation process of unstable rupture in the brittle regime: A theoretical approach based on experimentally inferred relations, *J. Geophys. Res.*, *96*, 8351-8367, 1991.

Zhou, Y., K.C. McNally, and T. Lay, Analysis of the 1986 Mount Lewis, California, earthquake: Preshock sequence-mainshock-aftershock sequence, *Phys. Earth Planet. Inter.*, *75*, 267-288, 1993.

Zongjin, M., F. Zhengxiang, Z. Yingzhen, W. Chengmin, Z. Guomin, and L. Defu, *Earthquake Prediction*, Springer-Verlag, New York, 1990.